

Issue 1

2018 | Volume 14

The Journal on Advanced Studies in Theoretical and Experimental Physics,
including Related Themes from Mathematics

PROGRESS IN PHYSICS



“All scientists shall have the right to present their scientific research results, in whole or in part, at relevant scientific conferences, and to publish the same in printed scientific journals, electronic archives, and any other media.” — Declaration of Academic Freedom, Article 8

ISSN 1555-5534

PROGRESS IN PHYSICS

A quarterly issue scientific journal, registered with the Library of Congress (DC, USA). This journal is peer reviewed and included in the abstracting and indexing coverage of: Mathematical Reviews and MathSciNet (AMS, USA), DOAJ of Lund University (Sweden), Scientific Commons of the University of St. Gallen (Switzerland), Open-J-Gate (India), Referativnyi Zhurnal VINITI (Russia), etc.

Electronic version of this journal:
<http://www.ptep-online.com>

Advisory Board

Dmitri Rabounski,
Editor-in-Chief, Founder
Florentin Smarandache,
Associate Editor, Founder
Larissa Borissova,
Associate Editor, Founder

Editorial Board

Pierre Millette
millette@ptep-online.com
Andreas Ries
ries@ptep-online.com
Gunn Quznetsov
quznetsov@ptep-online.com
Felix Scholkmann
scholkmann@ptep-online.com
Ebenezer Chifu
chifu@ptep-online.com

Postal Address

Department of Mathematics and Science,
University of New Mexico,
705 Gurley Ave., Gallup, NM 87301, USA

Copyright © *Progress in Physics*, 2018

All rights reserved. The authors of the articles do hereby grant *Progress in Physics* non-exclusive, worldwide, royalty-free license to publish and distribute the articles in accordance with the Budapest Open Initiative: this means that electronic copying, distribution and printing of both full-size version of the journal and the individual papers published therein for non-commercial, academic or individual use can be made by any user without permission or charge. The authors of the articles published in *Progress in Physics* retain their rights to use this journal as a whole or any part of it in any other publications and in any way they see fit. Any part of *Progress in Physics* howsoever used in other publications must include an appropriate citation of this journal.

This journal is powered by L^AT_EX

A variety of books can be downloaded free from the Digital Library of Science:
<http://fs.gallup.unm.edu/ScienceLibrary.htm>

ISSN: 1555-5534 (print)
ISSN: 1555-5615 (online)

Standard Address Number: 297-5092
Printed in the United States of America

January 2018

Vol. 14, Issue 1

CONTENTS

Müller H. Astrobiological Aspects of Global Scaling	3
Abdelmohssin F. A. Y. Modified Standard Einstein's Field Equations and the Cosmological Constant	7
Millette P. A. Bosons and Fermions as Dislocations and Disclinations in the Spacetime Continuum	10
Müller H. Gravity as Attractor Effect of Stability Nodes in Chain Systems of Harmonic Quantum Oscillators	19
Belyakov A. V. On the Ultimate Energy of Cosmic Rays	24
Borissova L., Rabounski D. Cosmological Redshift in the De Sitter Stationary Universe	27
Eid S. A., Diab S. M. Nuclear Structure of ^{154,156} Dy Isotopes	30
Grigoryan A., Kutuzyan A., Yesayan G. Soliton-effect Spectral Self-compression for Different Initial Pulses	35
Petit J.-P. A Symplectic Cosmological Model	38
Müller H. Quantum Gravity Aspects of Global Scaling and the Seismic Profile of the Earth	41
Medina V., Falcon N. Relativistic Model for Radiating Spherical Collapse	46

Information for Authors

Progress in Physics has been created for rapid publications on advanced studies in theoretical and experimental physics, including related themes from mathematics and astronomy. All submitted papers should be professional, in good English, containing a brief review of a problem and obtained results.

All submissions should be designed in L^AT_EX format using *Progress in Physics* template. This template can be downloaded from *Progress in Physics* home page <http://www.ptep-online.com>

Preliminary, authors may submit papers in PDF format. If the paper is accepted, authors can manage L^AT_EX typing. Do not send MS Word documents, please: we do not use this software, so unable to read this file format. Incorrectly formatted papers (i.e. not L^AT_EX with the template) will not be accepted for publication. Those authors who are unable to prepare their submissions in L^AT_EX format can apply to a third-party payable service for LaTeX typing. Our personnel work voluntarily. Authors must assist by conforming to this policy, to make the publication process as easy and fast as possible.

Abstract and the necessary information about author(s) should be included into the papers. To submit a paper, mail the file(s) to the Editor-in-Chief.

All submitted papers should be as brief as possible. Short articles are preferable. Large papers can also be considered. Letters related to the publications in the journal or to the events among the science community can be applied to the section *Letters to Progress in Physics*.

All that has been accepted for the online issue of *Progress in Physics* is printed in the paper version of the journal. To order printed issues, contact the Editors.

Authors retain their rights to use their papers published in *Progress in Physics* as a whole or any part of it in any other publications and in any way they see fit. This copyright agreement shall remain valid even if the authors transfer copyright of their published papers to another party.

Electronic copies of all papers published in *Progress in Physics* are available for free download, copying, and re-distribution, according to the copyright agreement printed on the titlepage of each issue of the journal. This copyright agreement follows the *Budapest Open Initiative* and the *Creative Commons Attribution-Noncommercial-No Derivative Works 2.5 License* declaring that electronic copies of such books and journals should always be accessed for reading, download, and copying for any person, and free of charge.

Consideration and review process does not require any payment from the side of the submitters. Nevertheless the authors of accepted papers are requested to pay the page charges. *Progress in Physics* is a non-profit/academic journal: money collected from the authors cover the cost of printing and distribution of the annual volumes of the journal along the major academic/university libraries of the world. (Look for the current author fee in the online version of *Progress in Physics*.)

Astrobiological Aspects of Global Scaling

Hartmut Müller

E-mail: hm@interscalar.com

In this paper we apply chain systems of harmonic quantum oscillators as a fractal model of matter to the analysis of astrophysical and biological metric data. Astrobiological aspects of global scaling are discussed.

Introduction

Already in [1] we have shown that scale invariance is a fundamental characteristic of chain systems of harmonic oscillators. In [2] we applied this model on chain systems of harmonic quantum oscillators and could show that particle rest masses coincide with the eigenstates of the system. This is valid not only for hadrons, but for mesons and leptons as well. On this background we proposed scaling as model of mass emergency [3] and introduced our fractal model of matter as a chain system of oscillating protons and electrons. Andreas Ries [4] demonstrated that this model allows for the prediction of the most abundant isotope of a given chemical element.

Our fractal model of matter as a chain system of oscillating protons and electrons provides also a good description of the mass distribution of large celestial bodies in the Solar System [5]. Physical properties of celestial bodies such as mass, size, rotation and orbital period can be understood as macroscopic quantized eigenstates in chain systems of oscillating protons and electrons [6]. This allows to see a connection between the stability of the Solar system and the stability of electron and proton and consider scale invariance as a forming factor of the Solar system.

In [7] we have calculated the model masses of unknown planets in the Solar system which correspond well with the hypothesis of Batygin and Brown [8] about a new gas giant called “planet 9” and with the hypothesis of Volk and Malhotra [9] about an unknown Mars-to-Earth mass “planet 10” beyond Pluto.

In [6] we have proposed a new interpretation of the cosmic microwave background as a stable eigenstate in a chain system of oscillating protons. Therefore, our model may be of cosmological significance as well.

In [10] we applied our model to the domain of biophysics and have demonstrated that the frequency ranges of electrical brain activity and of other cyclical biological processes correspond with eigenstates in chain systems of oscillating protons and electrons. This would indicate that biological cycles may have a subatomic origin.

Scale invariance as a property of the metric characteristics of biological organisms is well studied [11, 12] and it is not an exclusive characteristic of adult physiology. Furthermore, many metric characteristics of human physiology, for example, the frequency ranges of electrical brain activity [13, 14],

are common to most mammalian species.

In this paper we demonstrate how the scale invariance of our fractal model of matter as a chain system of oscillating protons and electrons allows us to see a connection between the metric characteristics of biological organisms and those of the celestial bodies. This connection could be of astrobiological significance.

Methods

In [1] we have shown that the set of natural frequencies of a chain system of similar harmonic oscillators coincides with a set of finite continued fractions \mathcal{F} , which are natural logarithms:

$$\ln(\omega_{jk}/\omega_{00}) = n_{j0} + \frac{z}{n_{j1} + \frac{z}{n_{j2} + \dots + \frac{z}{n_{jk}}}} =$$

$$= [z, n_{j0}; n_{j1}, n_{j2}, \dots, n_{jk}] = \mathcal{F}, \quad (1)$$

where ω_{jk} is the set of angular frequencies and ω_{00} is the fundamental frequency of the set. The denominators are integer: $n_{j0}, n_{j1}, n_{j2}, \dots, n_{jk} \in \mathbb{Z}$, the cardinality $j \in \mathbb{N}$ of the set and the number $k \in \mathbb{N}$ of layers are finite. In the canonical form, the numerator z equals 1.

For finite continued fractions \mathcal{F} (1), ranges of high distribution density (nodes) arise near reciprocal integers $1, 1/2, 1/3, 1/4, \dots$ which are the attractor points of the distribution.

Any finite continued fraction represents a rational number [15]. Therefore, all natural frequencies ω_{jk} in (1) are irrational, because for rational exponents the natural exponential function is transcendental [16]. It is probable that this circumstance provides for high stability of an oscillating chain system because it prevents resonance interaction between the elements of the system [17]. Already in 1987 we have applied continued fractions of the type \mathcal{F} (1) as criterion of stability in engineering [18, 19].

In the case of harmonic quantum oscillators, the continued fractions \mathcal{F} (1) not only define fractal sets of natural angular frequencies ω_{jk} , oscillation periods $\tau_{jk} = 1/\omega_{jk}$ and wavelengths $\lambda_{jk} = c/\omega_{jk}$ of the chain system, but also fractal sets of energies $E_{jk} = \hbar \cdot \omega_{jk}$ and masses $m_{jk} = E_{jk}/c^2$ which correspond with the eigenstates of the system. For this reason, we call the continued fraction \mathcal{F} (1) the “fundamental



Fig. 1: The canonical projection of \mathcal{F} (natural logarithmic representation).

fractal” of eigenstates in chain systems of harmonic quantum oscillators.

Normal matter is formed by nucleons and electrons because they are exceptionally stable. Furthermore, protons and neutrons have similar rest masses (the difference being only 0.14 percent). This allows us to interpret the proton and the neutron as similar quantum oscillators with regard to their rest masses. Therefore, in [3,6] we have introduced a fractal model of matter as a chain system of oscillating protons and electrons.

Table 1 shows the basic set of electron and proton units that can be considered as a fundamental metrology (c is the speed of light in vacuum, \hbar is the reduced Planck constant).

We hypothesize that scale invariance based on the fundamental fractal \mathcal{F} (1), calibrated on the metric properties of the proton and electron, is a universal characteristic of organized matter. This hypothesis we have called ‘global scaling’ [6].

Results

Let’s start with the metric characteristics large celestial bodies. The current amount of the Solar mass supports our hypothesis of global scaling, because it corresponds to a main attractor node of the \mathcal{F} (1) calibrated on the electron. In fact, the natural logarithm of the Sun-to-electron mass ratio is close to an integer number:

$$\ln\left(\frac{M_{\text{Sun}}}{m_{\text{electron}}}\right) = \ln\left(\frac{1.9884 \cdot 10^{30} \text{ kg}}{9.10938356 \cdot 10^{-31} \text{ kg}}\right) = 138.936$$

The electron rest mass is $m_e = 9.10938356 \cdot 10^{-31} \text{ kg}$ [20].

In the canonical form of the fundamental fractal \mathcal{F} (1), shorter continued fractions correspond with more stable eigenstates of a chain system of harmonic oscillators. There-

Table 1: The basic set of physical properties of the electron and proton. Data taken from Particle Data Group [20]. Frequencies, oscillation periods and the proton wavelength are calculated.

property	electron	proton
rest mass m	$9.10938356(11) \cdot 10^{-31} \text{ kg}$	$1.672621898(21) \cdot 10^{-27} \text{ kg}$
energy $E = mc^2$	$0.5109989461(31) \text{ MeV}$	$938.2720813(58) \text{ MeV}$
angular frequency $\omega = E/\hbar$	$7.76344071 \cdot 10^{20} \text{ Hz}$	$1.42548624 \cdot 10^{24} \text{ Hz}$
oscillation period $\tau = 1/\omega$	$1.28808867 \cdot 10^{-21} \text{ s}$	$7.01515 \cdot 10^{-25} \text{ s}$
wavelength $\lambda = c/\omega$	$3.8615926764(18) \cdot 10^{-13} \text{ m}$	$2.1030891 \cdot 10^{-16} \text{ m}$

fore, integer logarithms represent the most stable eigenstates (main attractor nodes).

In the framework of our model of matter, the correspondence of the Sun-to-electron mass ratio with a main attractor node of the fundamental fractal \mathcal{F} (1) is a criterion of high stability of the chain system of quantum oscillators that appears as the star we call ‘Sun’. Therefore, the current body mass of the Sun is not casual, but an essential aspect of its stability.

Also the correspondence of the current radius of the Sun with a main attractor node (integer logarithm) now we can understand as criterion of its stability:

$$\ln\left(\frac{R_{\text{Sun}}}{\lambda_{\text{electron}}}\right) = \ln\left(\frac{6.96407 \cdot 10^8 \text{ m}}{3.8615926764 \cdot 10^{-13} \text{ m}}\right) = 48.945$$

The angular Compton wavelength of the electron is $\lambda_e = 3.8615926764 \cdot 10^{-13} \text{ m}$ [20].

The natural logarithm of the proton-to-electron mass ratio is approximately 7.5 and consequently, the fundamental fractal \mathcal{F} calibrated on the proton will be shifted by 7.5 logarithmic units relative to the \mathcal{F} calibrated on the electron:

$$\ln\left(\frac{1.672621898 \cdot 10^{-27} \text{ kg}}{9.10938356 \cdot 10^{-31} \text{ kg}}\right) \approx 7.5$$

Consequently, integer logarithms of the proton \mathcal{F} correspond to half logarithms of the electron \mathcal{F} and vice versa. Therefore, all the most stable eigenstates are connected through division of the integer logarithms by 2.

As we have seen above, the Solar mass coincides with the main attractor and stability node [139; ∞] of the \mathcal{F} calibrated on the electron. Dividing the logarithm $139/2 = 69.5$ we receive the logarithm of the node [69; 2] that is the main node [62; ∞] of the \mathcal{F} calibrated on the proton, because $69.5 - 7.5 = 62$.

This main node corresponds to the mass: $m_p \cdot \exp(62) = 1.4 \text{ Kg}$, where $m_p = 1.672621 \cdot 10^{-27} \text{ kg}$ is the proton rest mass [20]. Probably, the mass range around 1.4 kg isn’t noticeable in astrophysics, but in biophysics it is. This mass range is typical for the adult human brain [21] represented by 7 billion samples (current terrestrial population of homo sapiens).

At the same time, the Solar mass is near the node [131; 2] of the \mathcal{F} calibrated on the proton, because $139 - 7.5 = 131.5$. Dividing the logarithm $131.5/2 = 65.75$ we receive a logarithm that corresponds to the significant subnode [66; -4] in the range of the world statistical average adult human body mass: $m_p \cdot \exp(65.75) = 60 \text{ kg}$ [20].

Jupiter's body mass coincides with the main attractor node [132; ∞] of the electron-calibrated \mathcal{F} (1):

$$\ln\left(\frac{M_{\text{Jupiter}}}{m_{\text{electron}}}\right) = \ln\left(\frac{1.8986 \cdot 10^{27} \text{ kg}}{9.10938356 \cdot 10^{-31} \text{ kg}}\right) = 131.98$$

Dividing the logarithm $132/2 = 66$ we receive the logarithm of the main node [66; ∞] that corresponds to the mass: $m_e \cdot \exp(66) = 42 \text{ g}$. This mass range coincides with the average mass of the human spinal cord [23].

At the same time, Jupiter's body mass is near the node [124; 5] of the proton-calibrated \mathcal{F} (1):

$$\ln\left(\frac{M_{\text{Jupiter}}}{m_{\text{proton}}}\right) = \ln\left(\frac{1.8986 \cdot 10^{27} \text{ kg}}{1.672621 \cdot 10^{-27} \text{ kg}}\right) = 124.47$$

The half value of this logarithm $124.47/2 = 62.24$ corresponds to the mass: $m_p \cdot \exp(62.24) = 1.78 \text{ kg}$ that is the range of the adult human liver [21]. It is remarkable that the most massive planet of the Solar System corresponds with the most massive organ of the human organism – the liver.

Saturn's body mass is near the subnode [123; 4] of the proton-calibrated \mathcal{F} (1):

$$\ln\left(\frac{M_{\text{Saturn}}}{m_{\text{proton}}}\right) = \ln\left(\frac{5.6836 \cdot 10^{23} \text{ kg}}{1.672621 \cdot 10^{-27} \text{ kg}}\right) = 123.26$$

The half value of this logarithm $123.26/2 = 61.63$ corresponds to the mass: $m_p \cdot \exp(61.63) = 0.975 \text{ kg}$ that is the range of the adult human lungs [21]. It is remarkable that the second massive planet of the Solar System corresponds with the second massive organ of the human organism – the lungs.

The radius of Saturn is near the main node [54; ∞] of the \mathcal{F} calibrated on the proton:

$$\ln\left(\frac{R_{\text{Saturn}}}{\lambda_{\text{proton}}}\right) = \ln\left(\frac{6.0268 \cdot 10^7 \text{ m}}{2.1030891 \cdot 10^{-16} \text{ m}}\right) = 54.01$$

Dividing the logarithm $54/2 = 27$ we receive the logarithm of the main node [27; ∞] that corresponds to the wavelength $\lambda_p \cdot \exp(27) = 0.11 \text{ mm}$ that coincides with the size of the human fertile oocyte (zygote) [24].

As shown above, the Solar radius coincides with the main node [49; ∞] of the \mathcal{F} calibrated on the electron. Dividing the logarithm $49/2 = 24.5$ we receive the logarithm of the node [24; 2] that is the main node [32; ∞] of the \mathcal{F} calibrated on the proton, because $24.5 + 7.5 = 32$. This logarithm corresponds to the wavelength $\lambda_e \cdot \exp(24.5) = 16.6 \text{ mm}$ that coincides with the object focal length of the human eye [25] that is also the length of the newborn eyeball.

At the same time, the Solar radius is near the node [56; 2] of the \mathcal{F} calibrated on the proton:

$$\ln\left(\frac{R_{\text{Sun}}}{\lambda_{\text{proton}}}\right) = \ln\left(\frac{6.96407 \cdot 10^8 \text{ m}}{2.103089 \cdot 10^{-16} \text{ m}}\right) = 56.46$$

The angular Compton wavelength of the proton is $\lambda_p = 2.103089 \cdot 10^{-16} \text{ m}$ [20].

Dividing the logarithm $56.5/2 = 28.25$ we receive the logarithm of the significant subnode [28; 4] that corresponds to the wavelength $\lambda_p \cdot \exp(28.25) = 0.39 \text{ mm}$ that coincides with the second focal length [26] behind the retina of the human eye.

Already in 1981 Leonid Chislenko [27] did demonstrate that ranges of body masses and sizes preferred by the most quantity of biological species show an equidistant distribution on a logarithmic scale with a scaling factor close to 3. Probably, this is a consequence of global scaling, if we consider that the scaling factor $e = 2.718 \dots$ connects the main attractor nodes of stability in the fundamental fractal \mathcal{F} .

Conclusion

Applying our fractal model of matter as chain system of oscillating protons and electrons to the analysis of astrophysical and biophysical metric data we can assume that the metric characteristics of biological organisms and those of the Solar system have a common subatomic origin. However, there is a huge field of research where various discoveries are still to be expected.

Acknowledgements

The author is grateful to Viktor Panchelyuga and Leili Khosravi for valuable discussions.

Submitted on November 5, 2017

References

1. Müller H. Fractal Scaling Models of Resonant Oscillations in Chain Systems of Harmonic Oscillators. *Progress in Physics*, 2009, v. 5, no. 2, 72–76.
2. Müller H. Fractal Scaling Models of Natural Oscillations in Chain Systems and the Mass Distribution of Particles. *Progress in Physics*, 2010, v. 6, no. 3, 61–66.
3. Müller H. Emergence of Particle Masses in Fractal Scaling Models of Matter. *Progress in Physics*, 2012, v. 8, no. 4, 44–47.
4. Ries A. Qualitative Prediction of Isotope Abundances with the Bipolar Model of Oscillations in a Chain System. *Progress in Physics*, 2015, v. 11, 183–186.
5. Müller H. Fractal scaling models of natural oscillations in chain systems and the mass distribution of the celestial bodies in the Solar System. *Progress in Physics*, 2010, v. 6, no. 3, 61–66.
6. Müller H. Scale-Invariant Models of Natural Oscillations in Chain Systems and their Cosmological Significance. *Progress in Physics*, 2017, v. 13, 187–197.
7. Müller H. Global Scaling as Heuristic Model for Search of Additional Planets in the Solar System. *Progress in Physics*, 2017, v. 13, 204–206.
8. Batygin K., Brown M.E. Evidence for a distant giant planet in the Solar System. *The Astronomical Journal*, 2016, v. 151.
9. Volk K., Malhotra R. The curiously warped mean plane of the Kuiper belt. arXiv:1704.02444v2 [astro-ph.EP], 19 June 2017.
10. Müller H. Chain Systems of Harmonic Quantum Oscillators as a Fractal Model of Matter and Global Scaling in Biophysics. *Progress in Physics*, 2017, v. 13, no. 4, 231–233.

11. Barenblatt G.I. *Scaling*. Cambridge University Press, 2003.
 12. Schmidt-Nielsen K., *Scaling. Why is the animal size so important?* Cambridge University Press, 1984.
 13. Sainsbury R.S., Heynen A., Montoya C.P. Behavioral correlates of hippocampal type 2 theta in the rat. *Physiol. Behavior*, 1987, v. 39 (4), 513–519.
 14. Stewart M., Fox S.E., Hippocampal theta activity in monkeys. *Brain Research*, 1991, v. 538 (1), 59–63.
 15. Khintchine A.Ya. *Continued fractions*. University of Chicago Press, Chicago 1964.
 16. Hilbert D. Über die Transcendenz der Zahlen e und π . *Mathematische Annalen*, 1893, 43, 216–219.
 17. Panchelyuga V.A., Panchelyuga M.S. Resonance and Fractals on the Real Numbers Set. *Progress in Physics*, 2012, v. 8, no. 4, 48–53.
 18. Müller H. The general theory of stability and objective evolutionary trends of technology. Applications of developmental and construction laws of technology in CAD. Volgograd, VPI, 1987 (in Russian).
 19. Müller H. Superstability as a developmental law of technology. Technology laws and their Applications. Volgograd-Sofia, 1989 (in Russian).
 20. Olive K.A. et al. (Particle Data Group), *Chin. Phys. C*, 2016, v. 38, 090001. Patrignani C. et al. (Particle Data Group), *Chin. Phys. C*, 2016, v. 40, 100001.
 21. Singh D. et al. Weights of human organs at autopsy in Chandigarh zone of north-west India. *JIAFM*, 2004, v. 26 (3), 97-99.
 22. Walpole S.C. et al. The weight of nations: an estimation of adult human biomass. *BMC Public Health*, 2012, v. 12 (1), 439.
 23. Watson C., Paxinos G., Kayalioglu G. *The Spinal Cord*. Amsterdam: Elsevier, 2009.
 24. Zamboni L., Mishell D.R., Bell J.H., Baca M. Fine structure of the human ovum in the pronuclear stage. *Journal of Cell Biology* 1966, 30(3), 579–600.
 25. Hunt et al. *Light, Color and Vision*. Chapman and Hall, Ltd, London, 1968.
 26. Ebenholtz S.M. *Oculomotor Systems and Perception*. Cambridge Univ. Press, 2001.
 27. Chislenko L.L. *The structure of fauna and flora in connection with the sizes of the organisms*. Moscow, 1981 (in Russian).
-

Modified Standard Einstein's Field Equations and the Cosmological Constant

Faisal A. Y. Abdelmohssin

IMAM, University of Gezira, P.O. BOX: 526, Wad-Medani, Gezira State, Sudan
Sudan Institute for Natural Sciences, P.O. BOX: 3045, Khartoum, Sudan
E-mail: f.a.y.abdelmohssin@gmail.com

The standard Einstein's field equations have been modified by introducing a general function that depends on Ricci's scalar without a prior assumption of the mathematical form of the function. By demanding that the covariant derivative of the energy-momentum tensor should vanish and with application of Bianchi's identity a first order ordinary differential equation in the Ricci scalar has emerged. A constant resulting from integrating the differential equation is interpreted as the cosmological constant introduced by Einstein. The form of the function on Ricci's scalar and the cosmological constant corresponds to the form of Einstein-Hilbert's Lagrangian appearing in the gravitational action. On the other hand, when energy-momentum is not conserved, a new modified field equations emerged, one type of these field equations are Rastall's gravity equations.

1 Introduction

In the early development of the general theory of relativity, Einstein proposed a tensor equation to mathematically describe the mutual interaction between matter-energy and spacetime as [13]

$$R_{ab} = \kappa T_{ab} \quad (1.1)$$

where κ is the Einstein constant, T_{ab} is the energy-momentum, and R_{ab} is the Ricci curvature tensor which represents geometry of the spacetime in presence of energy-momentum.

Einstein demanded that conservation of energy-momentum should be valid in the general theory of relativity since energy-momentum is a tensor quantity. This was represented as

$$T_{ab;b} = 0 \quad (1.2)$$

where semicolon (;) represents covariant derivatives. But equation (1.2) requires

$$R_{ab;b} = 0 \quad (1.3)$$

too which is not always true.

Finally, Einstein presented his standard field equations (EFEs) describing gravity in the tensor equations form, namely, [2–5, 8–12]

$$G_{ab} = \kappa T_{ab} \quad (1.4)$$

where G_{ab} is the Einstein tensor given by

$$G_{ab} = R_{ab} - \frac{1}{2} g_{ab} R \quad (1.5)$$

where, R , is the Ricci scalar curvature, and g_{ab} is the fundamental metric tensor.

In his search for analytical solution to his field equations he turned to cosmology and proposed a model of static and homogenous universe filled with matter. Because he believed of the static model for the Universe, he introduced a constant

term in his standard field equations to represent a kind of “anti gravity” to balance the effect of gravitational attractions of matter in it.

Einstein modified his standard equations by introducing a term to his standard field equations including a constant which is called the cosmological constant Λ , [7] to become

$$R_{ab} - \frac{1}{2} g_{ab} R + g_{ab} \Lambda = \kappa T_{ab} \quad (1.6)$$

where Λ is the cosmological constant (assumed to have a very small value). Equation (1.6) may be written as

$$R_{ab} - \frac{1}{2} (R - 2\Lambda) g_{ab} = \kappa T_{ab} \quad (1.7)$$

Einstein rejected the cosmological constant for two reasons:

- The universe described by this theory was unstable.
- Observations by Edwin Hubble confirmed that the universe is expanding.

Recently, it has been believed that this cosmological constant might be one of the causes of the accelerated expansion of the Universe [15].

Einstein has never justified mathematically introduction of his cosmological constant in his field equations.

Based on that fact I have mathematically done that using simple mathematics.

2 Modified standard Einstein's field equations

I modified the (EFEs) by introducing a general function $L(R)$ of Ricci's scalar into the standard (EFEs). I do not assume a concrete form of the function. The modified (EFEs), then becomes

$$R_{ab} - g_{ab} L(R) = \kappa T_{ab} \quad (2.1)$$

Taking covariant derivative denoted by semicolon (;) of both sides of equation (2.1) yields

$$R_{ab;b} - [g_{ab}L(R)]_{;b} = \kappa T_{ab;b} \quad (2.2)$$

Since covariant divergence of the metric tensor vanishes, equation (2.2) may be written as

$$R_{ab;b} - g_{ab} \left(\frac{dL}{dR} \right) R_{;b} = \kappa T_{ab;b} \quad (2.3)$$

Substituting the Bianchi identity

$$R_{;c} = 2g^{ab}R_{ac;b} \quad (2.4)$$

in equation (2.3) and requiring the covariant divergence of the energy-momentum tensor to vanish (i.e. energy-momentum is conserved), namely, equation (1.2), we arrive at

$$R_{ab;b} - g_{ab} \left(\frac{dL}{dR} \right) (2g^{ac}R_{ab;c}) = 0 \quad (2.5)$$

Rearranging equation (2.5) we get

$$R_{ab;b} - 2 \left(\frac{dL}{dR} \right) (g_{ab}g^{ac}) R_{ab;c} = 0 \quad (2.6)$$

Substituting the following identity equation

$$g_{ab}g^{ac} = \delta_b^c \quad (2.7)$$

in equation (2.6), we get

$$R_{ab;b} - 2 \left(\frac{dL}{dR} \right) (\delta_b^c) R_{ab;c} = 0 \quad (2.8)$$

By changing the dummy indices, we arrive at

$$R_{ab;b} \left(1 - 2 \frac{dL}{dR} \right) = 0 \quad (2.9)$$

We have either,

$$R_{ab;b} = 0, \quad (2.10)$$

or

$$1 - 2 \left(\frac{dL}{dR} \right) = 0 \quad (2.11)$$

Equation (2.10) is not always satisfied as mentioned before. Whilst, equation (2.11) yields

$$\frac{dL}{dR} = \frac{1}{2} \quad (2.12)$$

This has a solution

$$L(R) = \frac{1}{2} R - C \quad (2.13)$$

where C is a constant.

Interpreting the constant of integration C , as the cosmological constant Λ , the functional dependence of $L(R)$ on Ricci scalar may be written as

$$L(R) = \frac{1}{2} (R - 2\Lambda) \quad (2.14)$$

Equation (2.14) is the well known Lagrangian functional of the Einstein-Hilbert action with the cosmological constant.

3 The Modified Equations and the Einstein Spaces

In absence of energy-momentum i.e. in a region of spacetime where there is no energy, a state which is different from vacuum state everywhere in spacetime, equation (2.1) becomes

$$R_{ab} - g_{ab}L(R) = 0 \quad (3.1)$$

Contacting equation (3.1) with g^{ab} , we get

$$R - NL(R) = 0 \quad (3.2)$$

where N is the dimension of the spacetime. Equation (3.2) yields

$$L(R) = \frac{1}{N} R \quad (3.3)$$

Substituting equation (3.3) in equation (3.1), we get

$$R_{ab} = \frac{1}{N} g_{ab}R \quad (3.4)$$

Equation (3.4) is the Einstein equation for Einstein spaces in differential geometry [1,2];

$$R_{ab} = I g_{ab} \quad (3.5)$$

where I is an invariant. This implies that the function I proposed, $L(R)$, is exactly the same as the invariant I in Einstein spaces equation when contacted with g^{ab} .

A 2D sections of the 4D spacetime of Einstein spaces are geometrically one of the geometries of spacetime which satisfies the standard Einstein's field equations in absence of energy-momentum.

A naive substitution of $N = 4$ into equation (3.4) would lead to an identity from which Ricci scalar could not be calculated, because it becomes a non-useful equation, it gives $R = R$.

4 The modified equations and gravity equations with non-conserved energy-momentum

Because in general relativity spacetime itself is changing, the energy is not conserved, because it can give energy to the particles and absorb it from them [2].

In cosmology the notion of dark energy – represented by term introduced by Einstein – and dark matter is a sort of sources of energy of unknown origin.

It is possible to incorporate the possibility of non-conserved energy-momentum tensor in the modified equations. In this case equation (2.9) should become

$$R_{ab;b} \left(1 - 2 \frac{dL}{dR} \right) = \kappa T_{ab;b} \quad (4.1)$$

where $T_{ab;b} \neq 0$. Since $R_{ab;b}$ is not always equals to zero, this implies that the bracket in the LHS of equation (4.1) is not zero in any case.

Let us assume it is equal to D , where D is a dimensionless constant, i.e.

$$1 - 2\frac{dL}{dR} = D \quad (4.2)$$

Then, equation (4.2) becomes

$$\frac{dL}{dR} = \frac{1}{2}(1 - D) \quad (4.3)$$

Now, integrating equation (4.3) yields

$$L(R, D) = \frac{1}{2}(1 - D)R - E \quad (4.4)$$

where E is a constant. When $D = 0$, equation (4.4) should reduce to equation (2.13), the equation in case of conserved energy-momentum, for which $E = \Lambda$. So, equation (4.4) becomes

$$L(R, D) = \frac{1}{2}(1 - D)R - \Lambda \quad (4.5)$$

Finally, the modified equations (equation (2.1)) in case of non-conserved energy-momentum become

$$R_{ab} - \frac{1}{2}(1 - D)g_{ab}R + \Lambda g_{ab} = \kappa T_{ab} \quad (4.6)$$

5 The modified equations and the Rastall gravity equations

Rastall [14] introduced a modification to the Einstein field equations, in which the covariant conservation condition $R_{ab;b} = 0$ is no longer valid.

In his theory he introduced a modification to the Einstein field equations without the cosmological constant which read

$$R_{ab} - \frac{1}{2}(1 - 2\lambda\kappa)g_{ab}R = \kappa T_{ab} \quad (5.1)$$

where λ is a free parameter. When $\lambda = 0$, we recover the standard Einstein's field equations. Comparing Rastall's equations in equation (5.1) with equation (4.6) without the cosmological constant, we deduce

$$D = 2\lambda\kappa \quad (5.2)$$

Acknowledgements

I gratefully acknowledge IMAM, University of Gezira, P.O. BOX: 526, Wad-Medani, Gezira State, Sudan, for full financial support of this work.

Submitted on November 5, 2017

References

1. Besse A.L. Einstein Manifolds. Classics in Mathematics. Berlin, Springer, 1987.
2. Misner C.W., Thorne K.S., Wheeler J.A. Gravitation, San Francisco: W. H. Freeman, 1973.
3. Landau L.D., Lifshitz E.M. The Classical Theory of Fields. 4th edition, Butterworth-Heinemann, 1975.
4. Hartle J.B. Gravity: An Introduction to Einstein's General Relativity, Addison-Wesley, 2003.
5. Carroll S. Spacetime and Geometry: An Introduction to General Relativity, Addison-Wesley, 2003.
6. Sharan P. Spacetime, Geometry and Gravitation, Springer, 2009.
7. D'Inverno R. Introducing Einstein's Relativity, Clarendon Press, 1992.
8. Hobson M.P., Efstathiou G.P., Lasenby A.N. General Relativity: An Introduction for Physicists, Cambridge University Press, 2006.
9. Schutz B.A. First Course in General Relativity. Cambridge University Press, 1985.
10. Foster J., Nightingale J.D. A Short Course in General Relativity. 3rd edition, Springer, 1995.
11. Wald R.M. General Relativity, Chicago University Press, 1984.
12. Hawking S.W., Israel W. Three Hundred Years of Gravitation, Cambridge University Press, 1987.
13. Mehra J. Einstein, Hilbert, and The Theory of Gravitation, Historical Origins of General Relativity Theory, Springer, 1974.
14. Rastall P. Phys. Rev. D6, 3357 1972.
15. Riess A., et al. Observational Evidence from Supernovae for an Accelerating Universe and a Cosmological Constant. *The Astronomical Journal*, 1998, v. 116(3), 1009–1038.

Bosons and Fermions as Dislocations and Disclinations in the Spacetime Continuum

Pierre A. Millette

PierreAMillette@alumni.uottawa.ca, Ottawa, Canada

We investigate the case for dislocations (translational displacements) and disclinations (rotational displacements) in the Spacetime Continuum corresponding to bosons and fermions respectively. The massless, spin-1 screw dislocation is identified with the photon, while edge dislocations correspond to bosons of spin-0, spin-1 and spin-2. Wedge disclinations are identified with quarks. We find that the twist disclination depends both on the space volume ℓ^3 of the disclination and on the length ℓ of the disclination. We identify the ℓ^3 twist disclination terms with the leptons, while the ℓ twist disclination which does not have a longitudinal (massive) component, is identified with the massless neutrino. We perform numerical calculations that show that the dominance of the ℓ and ℓ^3 twist disclination terms depend on the extent ℓ of the disclination: at low values of ℓ , the “weak interaction” term ℓ predominates up to about 10^{-18} m, which is the generally accepted range of the weak force, while at larger values of ℓ , the “electromagnetic interaction” term ℓ^3 predominates. The value of ℓ at which the two interactions in the total strain energy are equal is given by $\ell = 2.0 \times 10^{-18}$ m.

1 Introduction

Elementary quantum particles are classified into bosons and fermions based on integral and half-integral multiples of \hbar respectively, where \hbar is Planck’s reduced constant. Bosons obey Bose-Einstein statistics while fermions obey Fermi-Dirac statistics and the Pauli Exclusion Principle. These determine the number of non-interacting indistinguishable particles that can occupy a given quantum state: there can only be one fermion per quantum state while there is no such restriction on bosons.

This is explained in quantum mechanics using the combined wavefunction of two indistinguishable particles when they are interchanged:

$$\begin{aligned} \text{Bosons : } \quad & \Psi(1, 2) = \Psi(2, 1) \\ \text{Fermions : } \quad & \Psi(1, 2) = -\Psi(2, 1). \end{aligned} \quad (1)$$

Bosons commute and as seen from (1) above, only the symmetric part contributes, while fermions anticommute and only the antisymmetric part contributes. There have been attempts at a formal explanation of this phenomenon, the spin-statistics theorem, with Pauli’s being one of the first [1]. Jabs [2] provides an overview of these and also offers his own attempt at an explanation.

However, as Feynman comments candidly [3, see p. 4-3],

We apologize for the fact that we cannot give you an elementary explanation. An explanation has been worked out by Pauli from complicated arguments of quantum field theory and relativity. He has shown that the two must necessarily go together, but we have not been able to find a way of reproducing his arguments on an elementary level. It appears to be one of the few places in physics where there is a rule which can be stated

very simply, but for which no one has found a simple and easy explanation. The explanation is deep down in relativistic quantum mechanics. This probably means that we do not have a complete understanding of the fundamental principle involved. For the moment, you will just have to take it as one of the rules of the world.

The question of a simple and easy explanation is still outstanding. Eq. (1) is still the easily understood explanation, even though it is based on the exchange properties of particles, rather than on how the statistics of the particles are related to their spin properties. At this point in time, it is an empirical description of the phenomenon.

2 Quantum particles from STC defects

Ideally, the simple and easy explanation should be a *physical* explanation to provide a complete understanding of the fundamental principles involved. The Elastodynamics of the Spacetime Continuum (*STCED*) [6,7] provides such an explanation, based on dislocations and disclinations in the spacetime continuum. Part of the current problem is that there is no understandable physical picture of the quantum level. *STCED* provides such a picture.

The first point to note is that based on their properties, bosons obey the superposition principle in a quantum state. In *STCED*, the location of quantum particles is given by their deformation displacement u^μ . Dislocations [7, see chapter 9] are translational displacements that commute, satisfy the superposition principle and behave as bosons. As shown in section §3-6 of [7], particles with spin-0, 1 and 2 are described by

$$u^{\mu;\nu} = \varepsilon_{(0)}^{\mu\nu} + \varepsilon_{(2)}^{\mu\nu} + \omega_{(1)}^{\mu\nu}, \quad (2)$$

i.e. a combination of spin-0 $\varepsilon_{(0)}^{\mu\nu}$ (mass as deformation particle aspect), spin-1 $\omega_{(1)}^{\mu\nu}$ (electromagnetism) and spin-2 $\varepsilon_{(2)}^{\mu\nu}$

(deformation wave aspect), where

$$\epsilon^{\mu\nu} = \frac{1}{2} (u^{\mu;\nu} + u^{\nu;\mu}) = u^{(\mu;\nu)} \quad (3)$$

and

$$\omega^{\mu\nu} = \frac{1}{2} (u^{\mu;\nu} - u^{\nu;\mu}) = u^{[\mu;\nu]} \quad (4)$$

which are solutions of wave equations in terms of derivatives of the displacements $u^{\mu;\nu}$ as given in chapter 3 of [7].

Disclinations [7, see chapter 10], on the other hand, are rotational displacements that do not commute and that do not obey the superposition principle. You cannot have two rotational displacements in a given quantum state. Hence their number is restricted to one per quantum state. They behave as fermions.

Spinors represent spin one-half fermions. Dirac spinor fields represent electrons. Weyl spinors, derived from Dirac's four complex components spinor fields, are a pair of fields that have two complex components. Interestingly enough, "[u]sing just one element of the pair, one gets a theory of massless spin-one-half particles that is asymmetric under mirror reflection and ... found ... to describe the neutrino and its weak interactions" [4, p. 63].

"From the point of view of representation theory, Weyl spinors are the fundamental representations that occur when one studies the representations of rotations in four-dimensional space-time... spin-one-half particles are representation of the group SU(2) of transformations on two complex variables." [4, p. 63]. To clarify this statement, each rotation in three dimensions (an element of SO(3)) corresponds to two distinct elements of SU(2). Consequently, the SU(2) transformation properties of a particle are known as the particle's spin.

Hence, the unavoidable conclusion is that bosons are dislocations in the spacetime continuum, while fermions are disclinations in the spacetime continuum. Dislocations are translational displacements that commute, satisfy the superposition principle and behave as bosons. Disclinations, on the other hand, are rotational displacements that do not commute, do not obey the superposition principle and behave as fermions.

The equations in the following sections of this paper are derived in Millette [7]. The constants $\bar{\lambda}_0$ and $\bar{\mu}_0$ are the Lamé elastic constants of the spacetime continuum, where $\bar{\mu}_0$ is the shear modulus (the resistance of the continuum to *distortions*) and $\bar{\lambda}_0$ is expressed in terms of $\bar{\kappa}_0$, the bulk modulus (the resistance of the continuum to *dilatations*) according to

$$\bar{\lambda}_0 = \bar{\kappa}_0 - \bar{\mu}_0/2 \quad (5)$$

in a four-dimensional continuum.

3 Dislocations (bosons)

Two types of dislocations are considered in this paper: screw dislocations (see Fig. 1) and edge dislocations (see Fig. 2).

Fig. 1: A stationary screw dislocation in cartesian (x, y, z) and cylindrical polar (r, θ, z) coordinates.

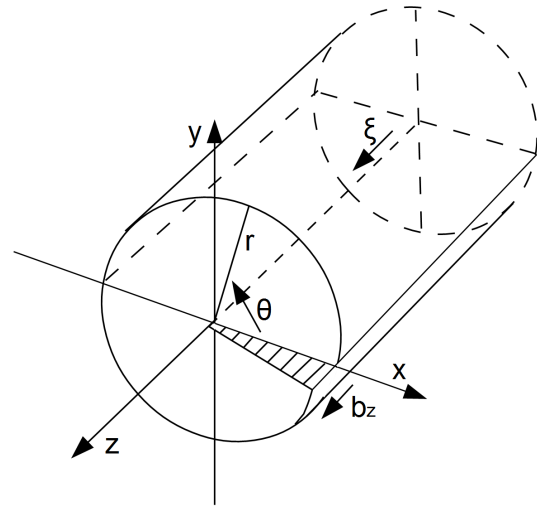
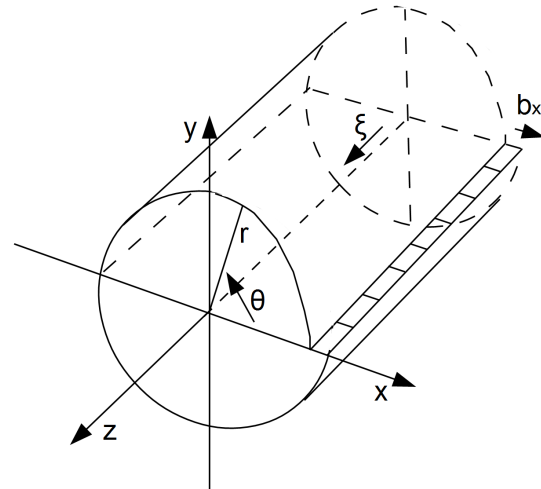


Fig. 2: A stationary edge dislocation in cartesian (x, y, z) and cylindrical polar (r, θ, z) coordinates.



Dislocations, due to their translational nature, are defects that are easier to analyze than disclinations.

3.1 Screw dislocation

The screw dislocation is analyzed in sections §9-2 and §15-1 of [7]. It is the first defect that we identified with the photon due to its being massless and of spin-1. Consequently, its longitudinal strain energy is zero

$$W_{\parallel}^S = 0. \quad (6)$$

Its transverse strain energy is given by [7, eq. (16.5)]

$$W_{\perp}^S = \frac{\bar{\mu}_0}{4\pi} b^2 \ell \ln \frac{\Lambda}{b_c}, \quad (7)$$

where b is the spacetime Burgers dislocation vector [9], ℓ is the length of the dislocation, b_c is the size of the core of the dislocation, of order b_0 , the smallest spacetime Burgers dislocation vector [10], and Λ is a cut-off parameter corresponding to the radial extent of the dislocation, limited by the average distance to its nearest neighbours.

3.2 Edge dislocation

The edge dislocation is analyzed in sections §9-3, §9-5 and §15-2 of [7]. The longitudinal strain energy of the edge dislocation is given by [7, eq. (16.29)]

$$W_{\parallel}^E = \frac{\bar{\kappa}_0}{2\pi} \bar{\alpha}_0^2 (b_x^2 + b_y^2) \ell \ln \frac{\Lambda}{b_c} \quad (8)$$

where

$$\bar{\alpha}_0 = \frac{\bar{\mu}_0}{2\bar{\mu}_0 + \bar{\lambda}_0}, \quad (9)$$

ℓ is the length of the dislocation and as before, Λ is a cut-off parameter corresponding to the radial extent of the dislocation, limited by the average distance to its nearest neighbours. The edge dislocations are along the z -axis with Burgers vector b_x for the edge dislocation proper represented in Fig. 2, and a different edge dislocation with Burgers vector b_y which we call the gap dislocation. The transverse strain energy is given by [7, eq. (16.54)]

$$W_{\perp}^E = \frac{\bar{\mu}_0}{4\pi} (\bar{\alpha}_0^2 + 2\bar{\beta}_0^2) (b_x^2 + b_y^2) \ell \ln \frac{\Lambda}{b_c} \quad (10)$$

where

$$\bar{\beta}_0 = \frac{\bar{\mu}_0 + \bar{\lambda}_0}{2\bar{\mu}_0 + \bar{\lambda}_0}. \quad (11)$$

The total longitudinal (massive) dislocation strain energy W_{\parallel}^D is given by (8)

$$W_{\parallel}^D = W_{\parallel}^S + W_{\parallel}^E = W_{\parallel}^E, \quad (12)$$

given that the screw dislocation longitudinal strain energy is zero, while the total transverse (massless) dislocation strain energy is given by the sum of the screw (along the z axis) and edge (in the $x-y$ plane) dislocation transverse strain energies

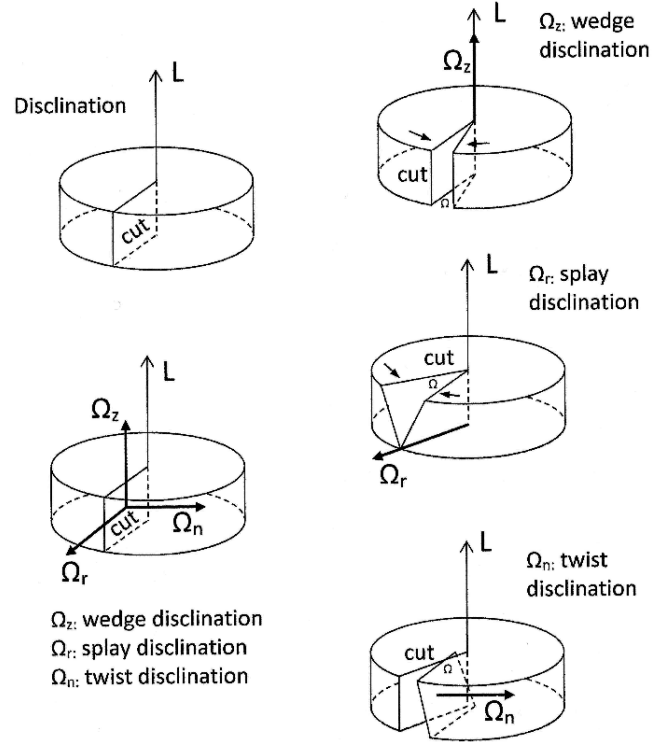
$$W_{\perp}^D = W_{\perp}^S + W_{\perp}^E \quad (13)$$

to give

$$W_{\perp}^D = \frac{\bar{\mu}_0}{4\pi} \left[b_z^2 + (\bar{\alpha}_0^2 + 2\bar{\beta}_0^2) (b_x^2 + b_y^2) \right] \ell \ln \frac{\Lambda}{b_c}. \quad (14)$$

It should be noted that as expected, the total longitudinal (massive) dislocation strain energy W_{\parallel}^D involves the spacetime bulk modulus $\bar{\kappa}_0$, while the total transverse (massless)

Fig. 3: Three types of disclinations: wedge (top), splay (middle), twist (bottom) [5, 7].



dislocation strain energy W_{\perp}^D involves the spacetime shear modulus $\bar{\mu}_0$.

The total strain energy of dislocations

$$W^D = W_{\parallel}^D + W_{\perp}^D \quad (15)$$

provides the total energy of massive and massless bosons, with W_{\parallel}^D corresponding to the longitudinal particle aspect of the bosons and W_{\perp}^D corresponding to the wave aspect of the bosons. As seen in [11], the latter is associated with the wavefunction of the boson. The spin characteristics of these was considered previously in section 2, where they were seen to correspond to spin-0, spin-1 and spin-2 solutions.

4 Disclinations (fermions)

The different types of disclinations considered in this paper are given in Fig. 3. Disclinations are defects that are more difficult to analyze than dislocations, due to their rotational nature. This mirrors the case of fermions, which are more difficult to analyze than bosons.

4.1 Wedge disclination

The wedge disclination is analyzed in sections §10-6 and §15-3 of [7]. The longitudinal strain energy of the wedge discli-

nation is given by [7, eq. (16.62)]

$$W_{\parallel}^W = \frac{\bar{\kappa}_0}{4\pi} \Omega_z^2 \ell \left[\bar{\alpha}_0^2 (2\Lambda^2 \ln^2 \Lambda - 2b_c^2 \ln^2 b_c) + \bar{\alpha}_0 \bar{\gamma}_0 (2\Lambda^2 \ln \Lambda - 2b_c^2 \ln b_c) + \frac{1}{2} (\bar{\alpha}_0^2 + \bar{\gamma}_0^2) (\Lambda^2 - b_c^2) \right] \quad (16)$$

where Ω^μ is the spacetime Frank vector,

$$\bar{\gamma}_0 = \frac{\bar{\lambda}_0}{2\bar{\mu}_0 + \bar{\lambda}_0} \quad (17)$$

and the other constants are as defined previously. In most cases $\Lambda \gg b_c$, and (16) reduces to

$$W_{\parallel}^W \simeq \frac{\bar{\kappa}_0}{2\pi} \Omega_z^2 \ell \Lambda^2 \left[\bar{\alpha}_0^2 \ln^2 \Lambda + \bar{\alpha}_0 \bar{\gamma}_0 \ln \Lambda + \frac{1}{4} (\bar{\alpha}_0^2 + \bar{\gamma}_0^2) \right] \quad (18)$$

which is rearranged as

$$W_{\parallel}^W \simeq \frac{\bar{\kappa}_0}{2\pi} \bar{\alpha}_0^2 \Omega_z^2 \ell \Lambda^2 \left[\ln^2 \Lambda + \frac{\bar{\gamma}_0}{\bar{\alpha}_0} \ln \Lambda + \frac{1}{4} \left(1 + \frac{\bar{\gamma}_0^2}{\bar{\alpha}_0^2} \right) \right]. \quad (19)$$

The transverse strain energy of the wedge disclination is given by [7, eq. (16.70)]

$$W_{\perp}^W = \frac{\bar{\mu}_0}{4\pi} \Omega_z^2 \ell \left[\bar{\alpha}_0^2 (\Lambda^2 \ln^2 \Lambda - b_c^2 \ln^2 b_c) - (\bar{\alpha}_0^2 - 3\bar{\alpha}_0 \bar{\beta}_0) (\Lambda^2 \ln \Lambda - b_c^2 \ln b_c) + \frac{1}{2} \left(\bar{\alpha}_0^2 - 3\bar{\alpha}_0 \bar{\beta}_0 + \frac{3}{2} \bar{\beta}_0^2 \right) (\Lambda^2 - b_c^2) \right]. \quad (20)$$

In most cases $\Lambda \gg b_c$, and (20) reduces to

$$W_{\perp}^W \simeq \frac{\bar{\mu}_0}{4\pi} \Omega_z^2 \ell \left[\bar{\alpha}_0^2 \Lambda^2 \ln^2 \Lambda - (\bar{\alpha}_0^2 - 3\bar{\alpha}_0 \bar{\beta}_0) \Lambda^2 \ln \Lambda + \frac{1}{2} \left(\bar{\alpha}_0^2 - 3\bar{\alpha}_0 \bar{\beta}_0 + \frac{3}{2} \bar{\beta}_0^2 \right) \Lambda^2 \right] \quad (21)$$

which is rearranged as

$$W_{\perp}^W \simeq \frac{\bar{\mu}_0}{4\pi} \bar{\alpha}_0^2 \Omega_z^2 \ell \Lambda^2 \left[\ln^2 \Lambda - \left(1 - 3 \frac{\bar{\beta}_0}{\bar{\alpha}_0} \right) \ln \Lambda + \frac{1}{2} \left(1 - 3 \frac{\bar{\beta}_0}{\bar{\alpha}_0} + \frac{3}{2} \frac{\bar{\beta}_0^2}{\bar{\alpha}_0^2} \right) \right]. \quad (22)$$

We first note that both the longitudinal strain energy W_{\parallel}^W and the transverse strain energy W_{\perp}^W are proportional to Λ^2 in the limit $\Lambda \gg b_c$. The parameter Λ is equivalent to the extent of the wedge disclination, and we find that as it becomes more extended, its strain energy is increasing parabolically. This

behaviour is similar to that of quarks (confinement) which are fermions. In addition, as $\Lambda \rightarrow b_c$, the strain energy decreases and tends to 0, again in agreement with the behaviour of quarks (asymptotic freedom).

We thus identify wedge disclinations with quarks. The total strain energy of wedge disclinations

$$W^W = W_{\parallel}^W + W_{\perp}^W \quad (23)$$

provides the total energy of the quarks, with W_{\parallel}^W corresponding to the longitudinal particle aspect of the quarks and W_{\perp}^W corresponding to the wave aspect of the quarks. We note that the current classification of quarks include both ground and excited states – the current analysis needs to be extended to excited higher energy states.

We note also that the rest-mass energy density $\rho^W c^2$ of the wedge disclination (see [7, eq. (10.102)]) is proportional to $\ln r$ which also increases with increasing r , while the rest-mass energy density $\rho^E c^2$ of the edge dislocation and $\rho^T c^2$ of the twist disclination (see [7, eqs. (9.134) and (10.123)]) respectively are both proportional to $1/r^2$ which decreases with increasing r as expected of bosons and leptons.

4.2 Twist disclination

The twist disclination is analyzed in sections §10-7 and §15-4 of [7]. Note that as mentioned in that section, we do not differentiate between twist and splay disclinations in this subsection as twist disclination expressions include both splay disclinations and twist disclinations proper. Note also that the Frank vector $(\Omega_x, \Omega_y, \Omega_z)$ corresponds to the three axes $(\Omega_r, \Omega_n, \Omega_z)$ used in Fig. 3 for the splay, twist and wedge disclinations respectively.

The longitudinal strain energy of the twist disclination is given by [7, eq. (16.80)]

$$W_{\parallel}^T = \frac{\bar{\kappa}_0}{6\pi} \bar{\alpha}_0^2 (\Omega_x^2 + \Omega_y^2) \ell^3 \ln \frac{\Lambda}{b_c}. \quad (24)$$

One interesting aspect of this equation is that the twist disclination longitudinal strain energy W_{\parallel}^T is proportional to the cube of the length of the disclination (ℓ^3), and we can't dispose of it by considering the strain energy per unit length of the disclination as done previously. We can say that the twist disclination longitudinal strain energy W_{\parallel}^T is thus proportional to the space volume of the disclination, which is reasonable considering that disclinations are rotational deformations. It is also interesting to note that W_{\parallel}^T has the familiar dependence $\ln \Lambda/b_c$ of dislocations, different from the functional dependence obtained for wedge disclinations in section 4.1. The form of this equation is similar to that of the longitudinal strain energy for the stationary edge dislocation (see [7, eq. (16.15)]) except for the factor $\ell^3/3$.

The transverse strain energy of the twist disclination is

given by [8]

$$\begin{aligned}
W_{\perp}^T = & \frac{\bar{\mu}_0}{2\pi} \frac{\ell^3}{3} \left[(\Omega_x^2 + \Omega_y^2) (\bar{\alpha}_0^2 + \frac{1}{2} \bar{\beta}_0^2) + \right. \\
& + 2 \Omega_x \Omega_y (\bar{\alpha}_0^2 - 2 \bar{\beta}_0^2) \left. \right] \ln \frac{\Lambda}{b_c} + \\
& + \frac{\bar{\mu}_0}{2\pi} \ell \left[(\Omega_x^2 + \Omega_y^2) (\bar{\alpha}_0^2 (\Lambda^2 \ln^2 \Lambda - b_c^2 \ln^2 b_c) + \right. \\
& + \bar{\alpha}_0 \bar{\gamma}_0 (\Lambda^2 \ln \Lambda - b_c^2 \ln b_c) - \frac{1}{2} \bar{\alpha}_0 \bar{\gamma}_0 (\Lambda^2 - b_c^2) + \\
& + 2 \bar{\beta}_0^2 \ln \frac{\Lambda}{b_c}) - 2 \Omega_x \Omega_y (\bar{\alpha}_0 \bar{\beta}_0 (\Lambda^2 \ln \Lambda - b_c^2 \ln b_c) + \\
& \left. + \frac{1}{2} \bar{\beta}_0 \bar{\gamma}_0 (\Lambda^2 - b_c^2)) \right].
\end{aligned} \tag{25}$$

In most cases $\Lambda \gg b_c$, and (25) reduces to

$$\begin{aligned}
W_{\perp}^T \simeq & \frac{\bar{\mu}_0}{2\pi} \frac{\ell^3}{3} \left[(\Omega_x^2 + \Omega_y^2) (\bar{\alpha}_0^2 + \frac{1}{2} \bar{\beta}_0^2) + \right. \\
& + 2 \Omega_x \Omega_y (\bar{\alpha}_0^2 - 2 \bar{\beta}_0^2) \left. \right] \ln \frac{\Lambda}{b_c} + \\
& + \frac{\bar{\mu}_0}{2\pi} \ell \Lambda^2 \left[(\Omega_x^2 + \Omega_y^2) (\bar{\alpha}_0^2 \ln^2 \Lambda + \bar{\alpha}_0 \bar{\gamma}_0 \ln \Lambda - \right. \\
& \left. - \frac{1}{2} \bar{\alpha}_0 \bar{\gamma}_0) - 2 \Omega_x \Omega_y (\bar{\alpha}_0 \bar{\beta}_0 \ln \Lambda + \frac{1}{2} \bar{\beta}_0 \bar{\gamma}_0) \right]
\end{aligned} \tag{26}$$

which can be rearranged to give

$$\begin{aligned}
W_{\perp}^T \simeq & \frac{\bar{\mu}_0}{2\pi} \bar{\alpha}_0^2 \frac{\ell^3}{3} \left[(\Omega_x^2 + \Omega_y^2) \left(1 + \frac{1}{2} \frac{\bar{\beta}_0^2}{\bar{\alpha}_0^2} \right) + \right. \\
& + 2 \Omega_x \Omega_y \left(1 - 2 \frac{\bar{\beta}_0^2}{\bar{\alpha}_0^2} \right) \left. \right] \ln \frac{\Lambda}{b_c} + \\
& + \frac{\bar{\mu}_0}{2\pi} \bar{\alpha}_0^2 \ell \Lambda^2 \left[(\Omega_x^2 + \Omega_y^2) \left(\ln^2 \Lambda + \frac{\bar{\gamma}_0}{\bar{\alpha}_0} \ln \Lambda - \right. \right. \\
& \left. \left. - \frac{1}{2} \frac{\bar{\gamma}_0}{\bar{\alpha}_0} \right) - 2 \Omega_x \Omega_y \left(\frac{\bar{\beta}_0}{\bar{\alpha}_0} \ln \Lambda + \frac{1}{2} \frac{\bar{\beta}_0 \bar{\gamma}_0}{\bar{\alpha}_0^2} \right) \right].
\end{aligned} \tag{27}$$

As noted previously, W_{\parallel}^T depends on the space volume ℓ^3 of the disclination and has a functional dependence of $\ln \Lambda/b_c$ as do the dislocations. The transverse strain energy W_{\perp}^T depends on the space volume ℓ^3 of the disclination with a functional dependence of $\ln \Lambda/b_c$, but it also includes terms that have a dependence on the length ℓ of the disclination with a functional dependence similar to that of the wedge disclination including Λ^2 in the limit $\Lambda \gg b_c$. The difference in the case of the twist disclination is that its transverse strain energy W_{\perp}^T combines ℓ^3 terms with the functional dependence $\ln \Lambda/b_c$ of dislocations, associated with the “electromagnetic interaction”, and ℓ terms with the $\Lambda^2 \ln^2 \Lambda$ functional dependence of wedge disclinations, associated with the “strong interaction”. This, as we will see in later sections, seems to be

the peculiar nature of the weak interaction, and uniquely positions twist disclinations to represent leptons and neutrinos as participants in the weak interaction.

This leads us to thus separate the longitudinal strain energy of the twist disclination as

$$W_{\parallel}^T = W_{\parallel}^{\ell^3} + W_{\parallel}^{\ell} = W_{\parallel}^{\ell^3} \tag{28}$$

given that $W_{\parallel}^{\ell} = 0$, and the transverse strain energy of the twist disclination as

$$W_{\perp}^T = W_{\perp}^{\ell^3} + W_{\perp}^{\ell}. \tag{29}$$

We consider both ℓ^3 twist disclination and ℓ twist disclination terms in the next subsections.

4.2.1 ℓ^3 twist disclination

The longitudinal strain energy of the ℓ^3 twist disclination is thus given by the ℓ^3 terms of (24)

$$W_{\parallel}^{\ell^3} = \frac{\bar{\kappa}_0}{6\pi} \bar{\alpha}_0^2 (\Omega_x^2 + \Omega_y^2) \ell^3 \ln \frac{\Lambda}{b_c}. \tag{30}$$

The transverse strain energy of the ℓ^3 twist disclination is given by the ℓ^3 terms of (25)

$$\begin{aligned}
W_{\perp}^{\ell^3} = & \frac{\bar{\mu}_0}{2\pi} \frac{\ell^3}{3} \left[(\Omega_x^2 + \Omega_y^2) (\bar{\alpha}_0^2 + \frac{1}{2} \bar{\beta}_0^2) + \right. \\
& \left. + 2 \Omega_x \Omega_y (\bar{\alpha}_0^2 - 2 \bar{\beta}_0^2) \right] \ln \frac{\Lambda}{b_c}.
\end{aligned} \tag{31}$$

In most cases $\Lambda \gg b_c$, and (31) is left unchanged due to its functional dependence on $\ln \Lambda/b_c$.

The total strain energy of the ℓ^3 twist disclination terms is given by

$$W^{\ell^3} = W_{\parallel}^{\ell^3} + W_{\perp}^{\ell^3}. \tag{32}$$

It is interesting to note that $W_{\parallel}^{\ell^3}$ of (30) and $W_{\perp}^{\ell^3}$ of (31) are proportional to $\ln \Lambda/b_c$, as are the screw dislocation (photon) and edge dislocation (bosons). This, and the results of the next subsection, leads us to identify the ℓ^3 twist disclination terms with the leptons (electron, muon, tau) fermions, where the heavier muon and tau are expected to be excited states of the electron.

4.2.2 ℓ twist disclination

The longitudinal strain energy of the ℓ twist disclination terms in this case is zero as mentioned previously

$$W_{\parallel}^{\ell} = 0. \tag{33}$$

The transverse strain energy of the ℓ twist disclination is thus also given by the ℓ terms of (25):

$$\begin{aligned} W_{\perp}^{\ell} = & \frac{\bar{\mu}_0}{2\pi} \ell \left[(\Omega_x^2 + \Omega_y^2) \left(\bar{\alpha}_0^2 (\Lambda^2 \ln^2 \Lambda - b_c^2 \ln^2 b_c) + \right. \right. \\ & + \bar{\alpha}_0 \bar{\gamma}_0 (\Lambda^2 \ln \Lambda - b_c^2 \ln b_c) - \frac{1}{2} \bar{\alpha}_0 \bar{\gamma}_0 (\Lambda^2 - b_c^2) + \\ & + 2 \bar{\beta}_0^2 \ln \frac{\Lambda}{b_c} - 2 \Omega_x \Omega_y (\bar{\alpha}_0 \bar{\beta}_0 (\Lambda^2 \ln \Lambda - b_c^2 \ln b_c) + \\ & \left. \left. + \frac{1}{2} \bar{\beta}_0 \bar{\gamma}_0 (\Lambda^2 - b_c^2) \right) \right]. \end{aligned} \quad (34)$$

In most cases $\Lambda \gg b_c$, and (34) reduces to

$$\begin{aligned} W_{\perp}^{\ell} = & \frac{\bar{\mu}_0}{2\pi} \ell \Lambda^2 \left[(\Omega_x^2 + \Omega_y^2) (\bar{\alpha}_0^2 \ln^2 \Lambda + \bar{\alpha}_0 \bar{\gamma}_0 \ln \Lambda - \right. \\ & \left. - \frac{1}{2} \bar{\alpha}_0 \bar{\gamma}_0) - 2 \Omega_x \Omega_y (\bar{\alpha}_0 \bar{\beta}_0 \ln \Lambda + \frac{1}{2} \bar{\beta}_0 \bar{\gamma}_0) \right] \end{aligned} \quad (35)$$

which can be rearranged to give

$$\begin{aligned} W_{\perp}^{\ell} = & \frac{\bar{\mu}_0}{2\pi} \bar{\alpha}_0^2 \ell \Lambda^2 \left[(\Omega_x^2 + \Omega_y^2) \left(\ln^2 \Lambda + \frac{\bar{\gamma}_0}{\bar{\alpha}_0} \ln \Lambda - \right. \right. \\ & \left. \left. - \frac{1}{2} \frac{\bar{\gamma}_0}{\bar{\alpha}_0} \right) - 2 \Omega_x \Omega_y \left(\frac{\bar{\beta}_0}{\bar{\alpha}_0} \ln \Lambda + \frac{1}{2} \frac{\bar{\beta}_0 \bar{\gamma}_0}{\bar{\alpha}_0^2} \right) \right]. \end{aligned} \quad (36)$$

The total strain energy of the ℓ twist disclination is given by

$$W^{\ell} = W_{\parallel}^{\ell} + W_{\perp}^{\ell} = W_{\perp}^{\ell} \quad (37)$$

given that the ℓ twist disclination does not have a longitudinal (massive) component. Since the ℓ twist disclination is a massless fermion, this leads us to identify the ℓ twist disclination with the neutrino.

There is another aspect to the strain energy W_{\perp}^T given by (25) that is important to note. As we have discussed, the ℓ^3 twist disclination terms and the $\ln \Lambda/b_c$ functional dependence as observed for the screw dislocation (photon) and edge dislocation (bosons) has led us to identify the ℓ^3 portion with the leptons (electron, muon, tau) fermions, where the heavier muon and tau are expected to be excited states of the electron. These are coupled with transverse ℓ twist disclination terms which are massless and which have a functional dependence similar to that of the wedge disclination, which has led us to identify the ℓ portion with the weakly interacting neutrino. If the muon and tau leptons are excited states of the electron derivable from (25), this would imply that the neutrino portion would also be specific to the muon and tau lepton excited states, thus leading to muon and tau neutrinos.

We will perform numerical calculations in the next section which will show that the dominance of the ℓ and ℓ^3 twist disclination terms depend on the extent ℓ of the disclination, with the ℓ “weak interaction” terms dominating for small values of ℓ and the ℓ^3 “electromagnetic interaction” terms dominating for larger values of ℓ . The ℓ twist disclination terms

would correspond to weak interaction terms while the ℓ^3 twist disclination terms would correspond to electromagnetic interaction terms. The twist disclination represents the unification of both interactions under a single “electroweak interaction”.

This analysis also shows why leptons (twist disclinations) are participants in the weak interaction but not the strong interaction, while quarks (wedge disclinations) are participants in the strong interaction but not the weak interaction.

It should be noted that even though the mass of the neutrino is currently estimated to be on the order of 10’s of eV, this estimate is based on assuming neutrino oscillation between the currently known three lepton generations, to explain the anomalous solar neutrino problem. This is a weak explanation for that problem, which more than likely indicates that we do not yet fully understand solar astrophysics. One can only hope that a fourth generation of leptons will not be discovered! Until the anomaly is fully understood, we can consider the twist disclination physical model where the mass of the neutrino is zero to be at least a first approximation of the neutrino STC defect model.

4.3 Twist disclination sample numerical calculation

In this section, we give a sample numerical calculation that shows the lepton-neutrino connection for the twist disclination. We start by isolating the common strain energy elements that don’t need to be calculated in the example. Starting from the longitudinal strain energy of the twist disclination (24) and making use of the relation $\bar{\kappa}_0 = 32\bar{\mu}_0$ [7, eq. (5.53)], (24) can be simplified to

$$W_{\parallel}^T = \frac{\bar{\mu}_0}{2\pi} \bar{\alpha}_0^2 2\Omega^2 \left[32 \frac{\ell^3}{3} \ln \frac{\Lambda}{b_c} \right] \quad (38)$$

where an average Ω is used instead of Ω_x and Ω_y . Defining K as

$$K = \frac{\bar{\mu}_0}{2\pi} \bar{\alpha}_0^2 2\Omega^2, \quad (39)$$

then (38) is written as

$$\frac{W_{\parallel}^T}{K} = 32 \frac{\ell^3}{3} \ln \frac{\Lambda}{b_c}. \quad (40)$$

Similarly for the transverse strain energy of the twist disclination, starting from (27), the equation can be simplified to

$$\begin{aligned} W_{\perp}^T \simeq & \frac{\bar{\mu}_0}{2\pi} \bar{\alpha}_0^2 2\Omega^2 \left\{ \left[\frac{\ell^3}{3} \left(1 + \frac{1}{2} \frac{\bar{\beta}_0^2}{\bar{\alpha}_0^2} + 1 - 2 \frac{\bar{\beta}_0^2}{\bar{\alpha}_0^2} \right) \ln \frac{\Lambda}{b_c} \right] + \right. \\ & + \left[\ell \Lambda^2 \left(\ln^2 \Lambda + \frac{\bar{\gamma}_0}{\bar{\alpha}_0} \ln \Lambda - \frac{1}{2} \frac{\bar{\gamma}_0}{\bar{\alpha}_0} - \right. \right. \\ & \left. \left. - \frac{\bar{\beta}_0}{\bar{\alpha}_0} \ln \Lambda - \frac{1}{2} \frac{\bar{\beta}_0 \bar{\gamma}_0}{\bar{\alpha}_0^2} \right) \right] \right\}. \end{aligned} \quad (41)$$

Using the definition of K from (39), this equation becomes

$$\frac{W_{\perp}^T}{K} \simeq \frac{\ell^3}{3} \left(2 - \frac{3\bar{\beta}_0^2}{2\bar{\alpha}_0^2} \right) \ln \frac{\Lambda}{b_c} + \ell \Lambda^2 \left(\ln^2 \Lambda + \frac{\bar{\gamma}_0 - \bar{\beta}_0}{\bar{\alpha}_0} \ln \Lambda - \frac{1}{2} \frac{\bar{\gamma}_0}{\bar{\alpha}_0} (1 + \bar{\beta}_0) \right). \quad (42)$$

Using the numerical values of the constants $\bar{\alpha}_0$, $\bar{\beta}_0$ and $\bar{\gamma}_0$ from [7, eqs. (19.14) and (19.35)], (42) becomes

$$\frac{W_{\perp}^T}{K} \simeq \frac{\ell^3}{3} (1.565) \ln \frac{\Lambda}{b_c} + \ell \Lambda^2 (\ln^2 \Lambda - \ln \Lambda - 0.62). \quad (43)$$

For this sample numerical calculation, we use $b_c \sim 10^{-35}$ m of the order of the spacetime Burgers dislocation constant b_0 , and the extent of the disclination $\Lambda \sim 10^{-18}$ m of the order of the range of the weak force. Then

$$\frac{W_{\parallel}^T}{K} = \frac{32}{3} (39.1) \ell^3 = 417 \ell^3. \quad (44)$$

and

$$\frac{W_{\perp}^T}{K} \simeq 0.522 (39.1) \ell^3 + \Lambda^2 (1714 + 41.4 - 0.62) \ell \quad (45)$$

which becomes

$$\frac{W_{\perp}^T}{K} \simeq 20.4 \ell^3 + 1755 \Lambda^2 \ell \quad (46)$$

and finally

$$\frac{W_{\perp}^T}{K} \simeq 20.4 \ell^3 + 1.76 \times 10^{-33} \ell. \quad (47)$$

We consider various values of ℓ to analyze its effect on the strain energy. For $\ell = 10^{-21}$ m,

$$\frac{W_{\parallel}^T}{K} = 4.2 \times 10^{-61} \quad (\ell^3 \text{ term}) \quad (48)$$

$$\frac{W_{\perp}^T}{K} = 2.0 \times 10^{-62} + 1.8 \times 10^{-54} \quad (\ell^3 \text{ term} + \ell \text{ term}). \quad (49)$$

For $\ell = 10^{-18}$ m,

$$\frac{W_{\parallel}^T}{K} = 4.2 \times 10^{-52} \quad (\ell^3 \text{ term}) \quad (50)$$

$$\frac{W_{\perp}^T}{K} = 2.0 \times 10^{-53} + 1.8 \times 10^{-51} \quad (\ell^3 \text{ term} + \ell \text{ term}). \quad (51)$$

For $\ell = 10^{-15}$ m,

$$\frac{W_{\parallel}^T}{K} = 4.2 \times 10^{-43} \quad (\ell^3 \text{ term}) \quad (52)$$

$$\frac{W_{\perp}^T}{K} = 2.0 \times 10^{-44} + 1.8 \times 10^{-48} \quad (\ell^3 \text{ term} + \ell \text{ term}). \quad (53)$$

For $\ell = 10^{-12}$ m,

$$\frac{W_{\parallel}^T}{K} = 4.2 \times 10^{-34} \quad (\ell^3 \text{ term}) \quad (54)$$

$$\frac{W_{\perp}^T}{K} = 2.0 \times 10^{-35} + 1.8 \times 10^{-45} \quad (\ell^3 \text{ term} + \ell \text{ term}). \quad (55)$$

In the sums of W_{\perp}^T/K above, the first term ℓ^3 represents the electromagnetic interaction, while the second term ℓ represents the weak interaction. Thus we find that at low values of ℓ , the weak force predominates up to about 10^{-18} m, which is the generally accepted range of the weak force. At larger values of ℓ , the electromagnetic force predominates. The value of ℓ at which the two interactions in the transverse strain energy are equal is given by

$$20.4 \ell^3 = 1.76 \times 10^{-33} \ell, \quad (56)$$

from which we obtain

$$\ell = 0.9 \times 10^{-17} \text{ m} \sim 10^{-17} \text{ m}. \quad (57)$$

At that value of ℓ , the strain energies are given by

$$\frac{W_{\parallel}^T}{K} = 3.0 \times 10^{-49} \quad (58)$$

$$\frac{W_{\perp}^T}{K} = 3.1 \times 10^{-50}. \quad (59)$$

The longitudinal (massive) strain energy predominates over the transverse strain energy by a factor of 10.

Alternatively, including the longitudinal ℓ^3 strain energy in the calculation, the value of ℓ at which the two interactions in the total strain energy are equal is given by

$$417 \ell^3 + 20.4 \ell^3 = 1.76 \times 10^{-33} \ell, \quad (60)$$

from which we obtain

$$\ell = 2.0 \times 10^{-18} \text{ m}. \quad (61)$$

At that value of ℓ , the strain energies are given by

$$\frac{W_{\parallel}^T}{K} = 3.3 \times 10^{-51} \quad (62)$$

$$\frac{W_{\perp}^T}{K} = 3.7 \times 10^{-51}. \quad (63)$$

The longitudinal (massive) strain energy and the transverse strain energy are then of the same order of magnitude.

5 Quantum particles and their associated spacetime defects

Table 1 provides a summary of the identification of quantum particles and their associated spacetime defects as shown in this paper.

STC defect	Type of particle	Particles
Screw dislocation	Massless boson	Photon
Edge dislocation	Massive boson	Spin-0 particle Spin-1 Proca eqn Spin-2 graviton
Wedge disclination	Massive fermion	Quarks
ℓ^3 Twist disclination	Massive fermion	Leptons
ℓ Twist disclination	Massless fermion	Neutrinos

Table 1: Identification of quantum particles and their associated defects.

6 Discussion and conclusion

In this paper, we have investigated the case for dislocations and disclinations in the Spacetime Continuum corresponding to bosons and fermions respectively. Dislocations are translational displacements that commute, satisfy the superposition principle and behave as bosons. Disclinations, on the other hand, are rotational displacements that do not commute, do not obey the superposition principle and behave as fermions, including having their number restricted to one per quantum state as it is not possible to have two rotational displacements in a given quantum state.

We have considered screw and edge dislocations. The massless, spin-1 screw dislocation is identified with the photon. The total strain energy of dislocations W^D corresponds to the total energy of massive and massless bosons, with W_{\parallel}^D corresponding to the longitudinal particle aspect of the bosons and W_{\perp}^D corresponding to the wave aspect of the bosons, with the latter being associated with the wavefunction of the boson. Their spin characteristics correspond to spin-0, spin-1 and spin-2 solutions.

We have considered wedge and twist disclinations, of which the splay disclination is a special case. Wedge disclinations are identified with quarks. The strain energy of wedge disclinations is proportional to Λ^2 in the limit $\Lambda \gg b_c$. The parameter Λ is equivalent to the extent of the wedge disclination, and we find that as it becomes more extended, its strain energy is increasing parabolically. This behaviour is similar to that of quarks (confinement) which are fermions. In addition, as $\Lambda \rightarrow b_c$, the strain energy decreases and tends to 0, again in agreement with the behaviour of quarks (asymptotic freedom). The total strain energy of wedge disclinations W^W thus corresponds to the total energy of the quarks, with W_{\parallel}^W corresponding to the longitudinal particle aspect of the quarks and W_{\perp}^W corresponding to the wave aspect of the quarks.

The twist disclination longitudinal strain energy W_{\parallel}^T is found to be proportional to the cube of the length of the disclination (ℓ^3), and hence depends on the space volume ℓ^3 of the disclination with a functional dependence of $\ln \Lambda/b_c$ as do the dislocations. The transverse strain energy W_{\perp}^T also depends

on the space volume ℓ^3 of the disclination with a functional dependence of $\ln \Lambda/b_c$, but it also includes terms that have a dependence on the length ℓ of the disclination with a functional dependence similar to that of the wedge disclination including Λ^2 in the limit $\Lambda \gg b_c$.

We have considered both ℓ^3 twist disclination and ℓ twist disclination terms. We note that $W_{\parallel}^{\ell^3}$ and $W_{\perp}^{\ell^3}$ are proportional to $\ln \Lambda/b_c$, as are the screw dislocation (photon) and edge dislocation (bosons), which leads us to identify the ℓ^3 twist disclination terms with the leptons (electron, muon, tau) fermions, where the heavier muon and tau are expected to be excited states of the electron. Given that the ℓ twist disclination does not have a longitudinal (massive) component, it is a massless fermion and this leads us to identify the ℓ twist disclination with the neutrino. Thus the twist disclination transverse strain energy W_{\perp}^T combines ℓ^3 terms with the functional dependence $\ln \Lambda/b_c$ of dislocations and ℓ terms with the functional dependence Λ^2 of wedge disclinations.

We have performed numerical calculations that show that the dominance of the ℓ and ℓ^3 twist disclination terms depend on the length ℓ of the disclination. We find that at low values of ℓ , the “weak interaction” term ℓ predominates up to about 10^{-18} m, which is the generally accepted range of the weak force. At larger values of ℓ , the “electromagnetic interaction” term ℓ^3 predominates. The value of ℓ at which the two interactions in the total strain energy are equal is given by $\ell = 2.0 \times 10^{-18}$ m. We conclude that in W_{\perp}^T , the ℓ twist disclination terms represent the weak interaction terms while the ℓ^3 twist disclination terms represent the electromagnetic interaction terms. The twist disclination hence represents the unification of both interactions under a single “electroweak interaction”.

This analysis also shows why leptons (twist disclinations) are participants in the weak interaction but not the strong interaction (wedge disclinations). In addition, if the muon and tau leptons are excited states of the electron derivable from (25), this would imply that the neutrino portion would also be specific to the muon and tau lepton excited states, thus leading to muon and tau neutrinos. A summary of the identification

of quantum particles and their associated spacetime defects as shown in this paper is provided in Table I.

Received on October 25, 2017

References

1. Pauli W. The Connection Between Spin and Statistics. *Phys. Rev.*, 1940, v. 58, 716–722. Reprinted in Schwinger, J., ed. *Selected Papers on Quantum Electrodynamics*. Dover Publications, New York, 1958, pp 372–378.
2. Jabs A. Connecting Spin and Statistics in Quantum Mechanics. arXiv: quant-ph/0810.2300v4.
3. Feynman R. P., Leighton R. B., Sands M. *Lectures on Physics, Volume III: Quantum Mechanics*. Addison-Wesley Publishing Company, Reading, Massachusetts, 1965.
4. Woit P. *Not Even Wrong: The Failure of String Theory and the Search for Unity in Physical Law*. Basic Books, New York, 2006.
5. Kleinert H. *Multivalued Fields in Condensed Matter, Electromagnetism, and Gravitation*. World Scientific Publishing, Singapore, 2008.
6. Millette P. A. Elastodynamics of the Spacetime Continuum. *The Abraham Zelmanov Journal*, 2012, v. 5, 221–277.
7. Millette P. A. *Elastodynamics of the Spacetime Continuum: A Spacetime Physics Theory of Gravitation, Electromagnetism and Quantum Physics*. American Research Press, Rehoboth, NM, 2017.
8. Corrected eq. (16.87) of [7].
9. Millette P. A. Dislocations in the Spacetime Continuum: Framework for Quantum Physics. *Progress in Physics*, 2015, vol. 11 (4), 287–307.
10. Millette P. A. The Burgers Spacetime Dislocation Constant b_0 and the Derivation of Planck's Constant. *Progress in Physics*, 2015, vol. 11 (4), 313–316.
11. Millette P. A. Wave-Particle Duality in the Elastodynamics of the Spacetime Continuum (STCED). *Progress in Physics*, 2014, vol. 10 (4), 255–258.

Gravity as Attractor Effect of Stability Nodes in Chain Systems of Harmonic Quantum Oscillators

Hartmut Müller

E-mail: hm@interscalar.com

In this paper we apply our fractal model of matter as chain systems of harmonic quantum oscillators to the analysis of gravimetric characteristics of the Solar system and introduce a model of gravity as macroscopic cumulative attractor effect of stability nodes in chain systems of oscillating protons and electrons.

Introduction

Gravity has still a special place in physics as it is the only interaction that is not described by a quantum theory. Nevertheless, the big G is considered to be a fundamental constant of nature, involved in the calculation of gravitational effects in Newton's law of universal gravitation and in Einstein's general theory of relativity. The currently recommended [1] value is $G = 6.67408(31) \cdot 10^{-11} \text{ m}^3 \text{ kg}^{-1} \text{ s}^{-2}$ and it seems that we know G only to three significant figures.

For several objects in the Solar System, the value of the standard gravitational parameter μ is known to greater accuracy than G . The value μ for the Sun is the heliocentric gravitational constant and equals $1.32712440042(1) \cdot 10^{20} \text{ m}^3 \text{ s}^{-2}$. The geocentric gravitational constant equals $3.986004418(8) \cdot 10^{14} \text{ m}^3 \text{ s}^{-2}$ [2]. The precision is 10^{-8} because this quantity is derived from the movement of artificial satellites, which basically involves observations of the distances from the satellite to earth stations at different times, which can be obtained to high accuracy using radar or laser ranging.

However, not the μ is directly measured, but the orbital elements of a natural or artificial satellite. For instance, the orbital elements of the Earth can be used to estimate the heliocentric gravitational constant. Already the basic solution for a circular orbit gives a good approximation:

$$\begin{aligned} \mu &= \frac{4\pi^2 R^3}{T^2} = \frac{4\pi^2 (149597870700 \text{ m})^3}{(31558149.54 \text{ s})^2} = \\ &= 1.327128 \cdot 10^{20} \text{ m}^3 \text{ s}^{-2} \end{aligned}$$

where R is the semi-major axis and T is the orbital period of the Earth. These orbital elements are directly measured, although $\mu = GM$ is an interpretation that provides mass as source of gravity and the universality of G . Within the principle of equivalence, gravity is a universal property like inertia and does not depend on the type or scale of matter.

Though, the big G is known only from laboratory measurements of the attraction force between two known masses. The precision of those measures is only 10^{-3} , because gravity appears too weak on the scale of laboratory-sized masses for to be measurable with the desired precision. However, as mentioned Quinn and Speake [3], the discrepant results may

demonstrate that we do not understand the metrology of measuring weak forces or they may signify some new physics.

On the other hand, the measured G values seem to oscillate over time [4]. It's not G itself that is varying, Anderson and coauthors proposed, but more likely something else is affecting the measurements, because the 5.9-year oscillatory period of the measured G values seems to correlate with the 5.9-year oscillatory period of Earth's rotation rate, as determined by recent Length of Day (LOD) measurements [5]. However, this hypothesis is still under discussion [6].

In 1981, Stacey, Tuck, Holding, Maher and Morris [7] reported anomalous measures of the gravity acceleration in mines. They proposed an explanation of this anomaly by introducing a short-range potential, of the Yukawa type, that overlaps the Newtonian potential and describes the intensity and the action range of a hypothetical fifth interaction. In 2005, Reginald T. Cahill [8] introduced an additional dimensionless constant that coincides with the fine structure constant and determines the strength of a new 3-space self-interaction that can explain various gravitational anomalies, such as the 'borehole anomaly' and the 'dark matter anomaly' in the rotation speeds of spiral galaxies.

Obviously, the origin of gravity and the nature of particle mass generation are key topics in modern physics and they seem to have a common future. In [9] we have introduced a fractal model of matter as a chain system of harmonic quantum oscillators and have shown that particle rest masses coincide with the eigenstates of the system. This is valid not only for hadrons, but for mesons and leptons as well. Andreas Ries [10] demonstrated that this model allows for the prediction of the most abundant isotope of a given chemical element. Already in [11] we could show that scale invariance is a fundamental property of this model. On this background we proposed quantum scaling as model of mass generation [12].

Our model of matter also provides a good approximation of the mass distribution of large celestial bodies in the Solar system [13]. Metric characteristics of celestial bodies can be understood as macroscopic quantized eigenstates in chain systems of oscillating protons and electrons [14].

In [15] we have calculated the model masses of new planets in the Solar system and in [16, 17] were estimated the orbital elements of these hypothetical bodies. Our calculations



Fig. 1: The canonical projection of \mathcal{F} (natural logarithmic representation).

correspond well with the hypothesis of Batygin and Brown [18] about a new gas giant called “planet 9” and with the hypothesis of Volk and Malhotra [19] about a Mars-to-Earth mass “planet 10” beyond Pluto.

Our model allows us to see a connection between the stability of the Solar system and the stability of the electron and proton and consider global scaling as a forming factor of the Solar system. This may be of cosmological significance.

In this paper we apply our model of matter to the analysis of gravimetric characteristics of large bodies of the Solar system and propose an interpretation of gravity as macroscopic cumulative attractor effect of stability nodes in chain systems of oscillating protons and electrons.

Methods

In [11] we have shown that the set of natural frequencies of a chain system of similar harmonic oscillators coincides with a set of finite continued fractions \mathcal{F} , which are natural logarithms:

$$\ln(\omega_{jk}/\omega_{00}) = n_{j0} + \frac{z}{n_{j1} + \frac{z}{n_{j2} + \dots + \frac{z}{n_{jk}}}} = [z, n_{j0}; n_{j1}, n_{j2}, \dots, n_{jk}] = \mathcal{F}, \quad (1)$$

where ω_{jk} is the set of angular frequencies and ω_{00} is the fundamental frequency of the set. The denominators are integer: $n_{j0}, n_{j1}, n_{j2}, \dots, n_{jk} \in \mathbb{Z}$, the cardinality $j \in \mathbb{N}$ of the set and the number $k \in \mathbb{N}$ of layers are finite. In the canonical form, the numerator z equals 1.

For finite continued fractions \mathcal{F} (1), ranges of high distribution density (nodes) arise near reciprocal integers $1, 1/2, 1/3, 1/4, \dots$ which are the attractor points of the distribution.

Any finite continued fraction represents a rational number [20]. Therefore, all natural frequencies ω_{jk} in (1) are irrational, because for rational exponents the natural exponential function is transcendental [21]. It is probable that this circumstance provides for high stability of an oscillating chain system because it prevents resonance interaction between the elements of the system [22]. Already in 1987 we have applied continued fractions of the type \mathcal{F} (1) as criterion of stability in engineering [23, 24].

In the case of harmonic quantum oscillators, the continued fractions \mathcal{F} (1) not only define fractal sets of natural angular frequencies ω_{jk} , angular accelerations $a_{jk} = c \cdot \omega_{jk}$, oscillation periods $\tau_{jk} = 1/\omega_{jk}$ and wavelengths $\lambda_{jk} = c/\omega_{jk}$ of

the chain system, but also fractal sets of energies $E_{jk} = \hbar \cdot \omega_{jk}$ and masses $m_{jk} = E_{jk}/c^2$ which correspond with the eigenstates of the system. For this reason, we call the continued fraction \mathcal{F} (1) the “fundamental fractal” of eigenstates in chain systems of harmonic quantum oscillators.

In the canonical form ($z = 1$) of the fundamental fractal \mathcal{F} (1), shorter continued fractions correspond with more stable eigenstates of a chain system of harmonic oscillators. Therefore, integer logarithms represent the most stable eigenstates (main attractor nodes).

Normal matter is formed by nucleons and electrons because they are exceptionally stable. Furthermore, protons and neutrons have similar rest masses (the difference being only 0.14 percent). This allows us to interpret the proton and the neutron as similar quantum oscillators with regard to their rest masses. Therefore, in [12, 14] we have introduced a fractal model of matter as a chain system of oscillating protons and electrons.

Table 1 shows the basic set of electron and proton units that can be considered as a fundamental metrology (c is the speed of light in vacuum, \hbar is the reduced Planck constant).

Table 1: The basic set of physical properties of the electron and proton. Data taken from Particle Data Group [25]. Frequencies, oscillation periods, accelerations and the proton wavelength are calculated.

property	electron	proton
rest mass m	$9.10938356(11) \cdot 10^{-31}$ kg	$1.672621898(21) \cdot 10^{-27}$ kg
energy $E = mc^2$	$0.5109989461(31)$ MeV	$938.2720813(58)$ MeV
angular frequency $\omega = E/\hbar$	$7.76344071 \cdot 10^{20}$ Hz	$1.42548624 \cdot 10^{24}$ Hz
angular oscillation period $\tau = 1/\omega$	$1.28808867 \cdot 10^{-21}$ s	$7.01515 \cdot 10^{-25}$ s
wavelength $\lambda = c/\omega$	$3.8615926764(18) \cdot 10^{-13}$ m	$2.1030891 \cdot 10^{-16}$ m
angular acceleration $a = c\omega$	$2.327421 \cdot 10^{29}$ ms ⁻²	$4.2735 \cdot 10^{32}$ ms ⁻²

The natural logarithm of the proton-to-electron mass ratio is approximately 7.5 and consequently, the fundamental fractal \mathcal{F} calibrated on the proton will be shifted by 7.5 logarithmic units relative to the \mathcal{F} calibrated on the electron:

$$\ln \frac{1.672621898 \cdot 10^{-27} \text{ kg}}{9.10938356 \cdot 10^{-31} \text{ kg}} \approx 7.5$$

We hypothesize that scale invariance based on the fundamental fractal \mathcal{F} (1), calibrated on the metric properties of the proton and electron, is a universal characteristic of organized matter. This hypothesis we have called ‘global scaling’ [14, 26].

Results

In [12] we have shown that the Planck mass coincides with the main attractor node [44; ∞] of the \mathcal{F} (1) calibrated on the proton:

$$\ln \frac{m_{\text{Planck}}}{m_{\text{proton}}} = \ln \frac{2.17647 \cdot 10^{-8}}{1.6726219 \cdot 10^{-27}} = 44.01$$

This circumstance allows us to calculate the big G from the proton rest mass:

$$G = \frac{\hbar c}{m_p^2} \exp(-88) = 6.8420676 \cdot 10^{-11} \text{ m}^3 \text{ kg}^{-1} \text{ s}^{-2}$$

The calculated G value is larger than the currently recommended by CODATA [1], although the published [27,28] values of G show immense variations and some recent measurements of high precision deliver, in fact, larger values than the recommended.

Applying our model (1), we can see that the Solar equatorial surface gravity acceleration $g_{\text{Sun}} = 274 \text{ m/s}^2$ corresponds with a main attractor node of the \mathcal{F} (1) calibrated on the angular acceleration of the electron $a_{\text{electron}} = 2.327421 \cdot 10^{29} \text{ ms}^{-2}$ (see table 1). In fact, the logarithm of the electron-to-Solar gravity acceleration ratio is close to an integer:

$$\ln \frac{a_{\text{electron}}}{g_{\text{Sun}}} = \ln \frac{2.327421 \cdot 10^{29} \text{ ms}^{-2}}{274 \text{ ms}^{-2}} = 62.00$$

This coincidence supports our hypothesis of global scaling and allows us to understand that the current amount of the surface gravity acceleration of the Sun is not casual, but an essential aspect of stability of the chain system of quantum oscillators that appears as the star we call 'Sun'.

Also the current amount of the Solar mass we recognise as criterion of stability, because it corresponds to a main attractor node of the \mathcal{F} (1) calibrated on the electron. In fact, the natural logarithm of the Sun-to-electron mass ratio is close to an integer number:

$$\ln \frac{M_{\text{Sun}}}{m_{\text{electron}}} = \ln \frac{1.9884 \cdot 10^{30} \text{ kg}}{9.10938356 \cdot 10^{-31} \text{ kg}} = 138.94$$

Furthermore, the main attractor node [62; ∞] of the \mathcal{F} (1) calibrated on the electron corresponds with the node [69; 2] calibrated on the proton that is half of the logarithm of the Solar-to-electron mass ratio: $69.5 = 139/2$. This allows us to write down an equation that connects the Sun-to-electron mass ratio with the proton-to-Solar surface gravity acceleration ratio:

$$\frac{M_{\text{Sun}}}{m_{\text{electron}}} = \left(\frac{a_{\text{proton}}}{g_{\text{Sun}}} \right)^2$$

As well, the correspondence of the current radius of the Sun with a main attractor node (integer logarithm) of the \mathcal{F} (1)

calibrated on the electron now we can understand as additional criterion of stability of the Sun:

$$\ln \frac{R_{\text{Sun}}}{\lambda_{\text{electron}}} = \ln \frac{6.96407 \cdot 10^8 \text{ m}}{3.8615926764 \cdot 10^{-13} \text{ m}} = 48.95$$

The logarithm of the proton-to-Jupiter surface gravity acceleration ratio is also close to an integer:

$$\ln \frac{a_{\text{proton}}}{g_{\text{Jupiter}}} = \ln \frac{4.2735 \cdot 10^{32} \text{ ms}^{-2}}{24.79 \text{ ms}^{-2}} = 71.92$$

Jupiter's body mass coincides with the main attractor node [132; ∞] of the electron-calibrated \mathcal{F} (1):

$$\ln \frac{M_{\text{Jupiter}}}{m_{\text{electron}}} = \ln \frac{1.8986 \cdot 10^{27} \text{ kg}}{9.10938356 \cdot 10^{-31} \text{ kg}} = 131.98$$

The surface gravity accelerations of Saturn (10.4 m/s^2), Uranus (8.7 m/s^2), Neptune (11.1 m/s^2), Earth (9.81 m/s^2) and Venus (8.87 m/s^2) approximate the main attractor node [73; ∞] of the \mathcal{F} (1) calibrated on the proton:

$$\ln \frac{a_{\text{proton}}}{g_{\text{Venus}}} = \ln \frac{4.2735 \cdot 10^{32} \text{ ms}^{-2}}{8.87 \text{ ms}^{-2}} = 72.95$$

The mass of Venus corresponds to the main attractor node [126; ∞] of the electron-calibrated \mathcal{F} (1):

$$\ln \frac{M_{\text{Venus}}}{m_{\text{electron}}} = \ln \frac{4.8675 \cdot 10^{24} \text{ kg}}{9.10938356 \cdot 10^{-31} \text{ kg}} = 126.01$$

Finally, the surface gravity accelerations of Mercury and Mars (3.71 m/s^2) approximate the main attractor node [74; ∞] of the \mathcal{F} (1) calibrated on the proton:

$$\ln \frac{a_{\text{proton}}}{g_{\text{Mars}}} = \ln \frac{4.2735 \cdot 10^{32} \text{ ms}^{-2}}{3.71 \text{ ms}^{-2}} = 73.83$$

The body mass of Mars corresponds to the main attractor node [124; ∞] of the \mathcal{F} (1) calibrated on the electron:

$$\ln \frac{M_{\text{Mars}}}{m_{\text{electron}}} = \ln \frac{6.4171 \cdot 10^{23} \text{ kg}}{9.10938356 \cdot 10^{-31} \text{ kg}} = 123.99$$

In [14] we have shown that the body masses, the rotation and orbital periods of the planets and the Sun are quantized. They follow the sequence of attractor nodes of stability of the fundamental fractal \mathcal{F} (1). Now we can affirm that the surface gravity accelerations of the planets and the Sun are quantized as well. The surface gravity accelerations of the planets correspond with the main attractor nodes [72; ∞], [73; ∞], [74; ∞] of the \mathcal{F} (1) calibrated on the proton while the surface gravity acceleration of the Sun corresponds with the main attractor node [62; ∞] of the \mathcal{F} (1) calibrated on the electron.

Considering that the angular acceleration of the electron is $a_{\text{electron}} = c\omega_{\text{electron}}$, we can express the Solar surface gravity acceleration in terms of the speed of light

$$g_{\text{Sun}} = c\omega_{\text{Sun}}$$

and receive the angular oscillation period $1/\omega_{\text{Sun}} = 12.7$ sidereal days that is the first harmonic of the equatorial rotation period 25.4 days of the Sun. This coincidence suggests to analyse also the gravity accelerations of the planets in terms of the speed of light.

If we express the Earth surface gravity acceleration $g = 9.8 \text{ ms}^{-2}$ in terms of the speed of light, we receive an oscillation period of $c/g = 355$ sidereal days that is in the range of the Earth orbital period and coincides perfectly with the attractor node [63; 2] of the \mathcal{F} (1) calibrated on the electron oscillation period $2\pi\tau_{\text{electron}} = 8.0933 \cdot 10^{-21} \text{ s}$:

$$2\pi\tau_{\text{electron}} \exp(63.5) = 355 \text{ days}$$

The period of 355 days coincides with 12 synodic lunar months, the lunar year. The surface gravity accelerations of Saturn (10.4 m/s^2), Uranus (8.7 m/s^2), Neptune (11.1 m/s^2) and Venus (8.87 m/s^2) are of the same range and consequently, they approximate the same attractor node [63; 2].

The surface gravity acceleration of Saturn $g_{\text{Saturn}} = 10.4 \text{ m/s}^2$ corresponds with an oscillation period of $c/g_{\text{Saturn}} = 334$ sidereal days that is in the range of the duration of lightning storms on Saturn which appear once every 30 Earth years. The lightning storm of 2009 on Saturn in the planet's southern hemisphere lasted over 334 days [29].

Mars and Mercury have similar surface gravity accelerations of about 3.7 ms^{-2} that corresponds to an oscillation period of $c/3.7 \text{ ms}^{-2} = 938$ sidereal days near the attractor node [64; 2] of the \mathcal{F} (1) calibrated on the electron:

$$2\pi\tau_{\text{electron}} \exp(64.5) = 966 \text{ days}$$

The sidereal rotation period of Mars is 24.62278 hours and coincides perfectly to the main node [67; ∞] of the proton-calibrated \mathcal{F} (1):

$$\ln \frac{\tau_{\text{Mars}}}{\tau_{\text{proton}}} = \ln \frac{24.62278 \cdot 3600 \text{ s}}{7.01515 \cdot 10^{-25} \text{ s}} = 67.00$$

In addition, the orbital period of Mars 686.971 days meets precisely the condition of global scaling:

$$\ln \frac{T_{\text{Mars}}}{\tau_{\text{electron}}} = \ln \frac{686.971 \cdot 86164 \text{ s}}{1.28808867 \cdot 10^{-21} \text{ s}} = 66.00$$

The surface gravity acceleration of Jupiter $g_{\text{Jupiter}} = 24.79 \text{ ms}^{-2}$ corresponds to an oscillation period of $c/g_{\text{Jupiter}} = 140$ sidereal days near the main attractor node of the \mathcal{F} calibrated on the electron:

$$2\pi\tau_{\text{electron}} \exp(62.5) = 131 \text{ days}$$

The sidereal rotation period of Jupiter is 9.925 hours and corresponds with the main attractor node [66; ∞] of the proton \mathcal{F} (1):

$$\ln \frac{\tau_{\text{Jupiter}}}{\tau_{\text{proton}}} = \ln \frac{9.9251 \cdot 3600 \text{ s}}{7.01515 \cdot 10^{-25} \text{ s}} = 66.10$$

Jupiter's orbital period of 4332.59 days fulfils the conditions of global scaling very precisely:

$$\ln \frac{T_{\text{Jupiter}}}{2\pi\tau_{\text{electron}}} = \ln \frac{4332.59 \cdot 86164 \text{ s}}{2\pi \cdot 1.28808867 \cdot 10^{-21} \text{ s}} = 66.00$$

When the logarithm of the sidereal rotation period of Jupiter slows down to [66; ∞], the orbital-to-rotation period ratio of Jupiter can be described by the equation:

$$\frac{T_{\text{Jupiter}}}{\tau_{\text{Jupiter}}} = \frac{2\pi\tau_{\text{electron}}}{\tau_{\text{proton}}}$$

We can see that both the orbital periods of Jupiter and Mars correspond with the main attractor node [66; ∞] of stability, but in the case of Jupiter with the electron oscillation period as fundamental and in the case of Mars with the electron angular oscillation period as fundamental. Therefore, both orbital periods are simply connected by 2π :

$$T_{\text{Jupiter}} = 2\pi T_{\text{Mars}}$$

Also these circumstances support our model of matter as chain system of harmonic quantum oscillators and our hypothesis of global scaling.

Conclusion

Applying our fractal model of matter as chain system of harmonic quantum oscillators to the analysis of gravimetric characteristics of large bodies of the Solar system we did show that the surface gravity accelerations of the planets and the Sun are quantized and correspond to nodes of stability in chain systems of oscillating protons and electrons and therefore, they can be estimated without any information about the masses or sizes of the celestial bodies.

Furthermore, the quantized surface gravity accelerations of the planets and the Sun seem to be connected with their quantized orbital and rotation periods.

We presume that the accretion of gravitational mass is a macroscopic cumulative attractor effect of stability nodes in chain systems of oscillating protons and electrons. From this point of view, Newton's constant of gravitation defines the corresponding amount of gravitational mass a given attractor node can accumulate.

Acknowledgements

The author is grateful to Viktor Panchelyuga for valuable discussions.

Submitted on November 23, 2017

References

1. CODATA recommended 2014 values of the fundamental physical constants: physics.nist.gov/constants.
2. Numerical Standards for Fundamental Astronomy. maia.usno.navy.mil, IAU Working Group, 2017.

3. Quinn T., Speake C. The Newtonian constant of gravitation – a constant too difficult to measure? An introduction. *Phil. Trans. Royal Society A*, v. 372, 20140253.
4. Anderson J. D. et al. Measurements of Newton's gravitational constant and the length of day. *EPL*, v. 110, 10002, 2015.
5. Holme R., de Viron O. Characterization and implications of intradecadal variations in length of day. *Nature*, v. 499, 202-204, 2013.
6. Schlamminger S. et al. Recent measurements of the gravitational constant as a function of time. arXiv:1505.01774v2 [gr-qc] 21 May 2015.
7. Stacey F. D. et al. Constraint on the planetary scale value of the Newtonian gravitational constant from the gravity profile within a mine. *Phys. Rev.* v. D23, 1683, 1981.
8. Cahill R. T. 3-Space In-Flow Theory of Gravity: Boreholes, Blackholes and the Fine Structure Constant. *Progress in Physics*, v. 2, 9–16, 2006.
9. Müller H. Fractal Scaling Models of Natural Oscillations in Chain Systems and the Mass Distribution of Particles. *Progress in Physics*, v. 3, 61–66, 2010.
10. Ries A. Qualitative Prediction of Isotope Abundances with the Bipolar Model of Oscillations in a Chain System. *Progress in Physics*, v. 11, 183–186, 2015.
11. Müller H. Fractal Scaling Models of Resonant Oscillations in Chain Systems of Harmonic Oscillators. *Progress in Physics*, v. 2, 72–76, 2009.
12. Müller H. Emergence of Particle Masses in Fractal Scaling Models of Matter. *Progress in Physics*, v. 4, 44–47, 2012.
13. Müller H. Fractal scaling models of natural oscillations in chain systems and the mass distribution of the celestial bodies in the Solar System. *Progress in Physics*, v. 3, 61–66, 2010.
14. Müller H. Scale-Invariant Models of Natural Oscillations in Chain Systems and their Cosmological Significance. *Progress in Physics*, v. 4, 187–197, 2017.
15. Müller H. Global Scaling as Heuristic Model for Search of Additional Planets in the Solar System. *Progress in Physics*, v. 4, 204–206, 2017.
16. Müller H. Scaling of body masses and orbital periods in the Solar System. *Progress in Physics*, v. 11, 133–135, 2015.
17. Müller H. Scaling of body masses and orbital periods in the Solar System as consequence of gravity interaction elasticity. Abstracts of the XII. International Conference on Gravitation, Astrophysics and Cosmology, dedicated to the centenary of Einstein's General Relativity theory. Moscow, PFUR, 2015.
18. Batygin K., Brown M. E. Evidence for a distant giant planet in the Solar System. *The Astronomical Journal*, 151 / 22, February 2016.
19. Volk K., Malhotra R. The curiously warped mean plane of the Kuiper belt. arXiv:1704.02444v2 [astro-ph.EP], 19 June 2017.
20. Khintchine A.Ya. Continued fractions. University of Chicago Press, Chicago, 1964.
21. Hilbert D. Über die Transcendenz der Zahlen e und π . *Mathematische Annalen*, v. 43, 216–219, 1893.
22. Panchelyuga V. A., Panchelyuga M. S. Resonance and Fractals on the Real Numbers Set. *Progress in Physics*, v. 4, 48–53, 2012.
23. Müller H. The general theory of stability and objective evolutionary trends of technology. Applications of developmental and construction laws of technology in CAD. Volgograd, VPI, 1987 (in Russian).
24. Müller H. Superstability as a developmental law of technology. Technology laws and their Applications. Volgograd-Sofia, 1989 (in Russian)
25. Olive K.A. et al. (Particle Data Group), *Chin. Phys. C*, v. 38, 090001, 2016.
Patrignani C. et al. (Particle Data Group), *Chin. Phys. C*, v. 40, 100001, 2016.
26. Müller H. Scaling as Fundamental Property of Natural Oscillations and the Fractal Structure of Space-Time. Foundations of Physics and Geometry. Peoples Friendship University of Russia, 2008 (in Russian).
27. Newell D.B. CODATA and the Newtonian Gravitational Constant. Newtonian constant of gravitation workshop NIST, 9–10 October, 2014.
28. Gillies G.T. The Newtonian gravitational constant: recent measurements and related studies. *Rep. Prog. Phys.*, v. 60, 151–225, 1997.
29. NASA's Cassini watches storm choke on its own tail. NASA/JPL-Caltech/SSI/Hampton University, Jan. 31, 2013.

LETTERS TO PROGRESS IN PHYSICS

On the Ultimate Energy of Cosmic Rays

Anatoly V. Belyakov

E-mail: belyakov.lih@gmail.com

It is established that the upper limit of cosmic-ray energy due to the Greisen-Zatsepin-Kuzmin effect is local. On the basis of the mechanistic interpretation of J. Wheeler's geometrodynamical concept, a more fundamental limitation on this limit was established, which, in the final analysis, depends on Planck's size $(\hbar\gamma/c^3)^{1/2}$ and for protons the limit is 4.51×10^{18} eV. The inflection in the spectrum curve, the "knee", corresponds to the mass-energy of the vortex tube of the limiting proton-electron contour, 1.46×10^{15} eV. For other nuclei these energies increase in proportion to the atomic number of the element.

Cosmic rays are a flow of nuclei of chemical elements — hydrogen (~ 90%), helium (~ 8%), and the nuclei of the heavier elements (~ 2%). The energy spectrum of cosmic rays or the dependence of the cosmic ray flux on energy extends from 10^3 to 10^{20} eV. The main sources of primary cosmic rays are supernova explosions (galactic cosmic rays) and the Sun, as well as extragalactic sources — radio galaxies and quasars. The protons and heavier nuclei emitted during supernova explosions are further accelerated in specific astrophysical processes. Falling into the earth's atmosphere, cosmic ray particles transmit their energy to a multitude of secondary particles. Thus, the particles cascade is formed; it is called an extensive air shower (EAS) and covers a large area.

Nature ultrahigh energy cosmic rays (more than 10^{17} eV) has not yet been unambiguously interpreted, their sources have not yet been identified, and there is no complete understanding of the mechanisms of their acceleration and even the nature of the accelerated particles [1]. There are reasons to assume that they are of extragalactic origin. It is believed that the upper limit of cosmic-ray energy is limited by a threshold of 5×10^{19} eV, because cosmic ray particles interact energetically with relic radiation, which leads to their absorption and reduction of their energy to a threshold value at distances of the order of several tens of megaparsecs (Greisen-Zatsepin-Kuzmin effect) [2, 3]. The presence of particles with energies exceeding this threshold does not yet find a satisfactory explanation, since within range of up to one hundred megaparsec powerful radiation sources are absent.

The question arises: what energy could be cosmic rays, if the distance between the source and the Earth would be much less than the Greisen-Zatsepin-Kuzmin limit, and could not microparticle produce a huge macroscopic effect? Here we see a paradox, since theoretically relativistic mass and energy of the particle can approach infinity. It seems that the Greisen-Zatsepin-Kuzmin effect is of local importance, and there are more fundamental causes that limit the energy of cosmic rays.

A fundamental limitation can be derived by considering a charged microparticle from the point of view of John Wheel-

er's geometrodynamical concept. Wheeler's concept assumes that charged microparticles are singular points on a topologically non-unitary coherent two-dimensional surface of our world, connected by a "wormhole", a vortex tube or a current line of the input-output kind in an additional dimension, generally forming a closed counter. According to the mechanistic interpretation of Wheeler's idea when the contour (proton-electronic, for example) is opened individual charged particles retain part of the contour vortex tube (boson mass) whose momentum is numerically equal to the charge [4, 5]. In these works formulas are derived for the vortex tube parameters: its boson mass m_y , the circulation velocity of the medium along the contour v , the radius r , and the length l_y :

$$m_y = (an)^2 m_e, \quad (1)$$

$$v = \frac{c_0^{1/3}}{(an)^2} c, \quad (2)$$

$$r = \frac{c_0^{2/3}}{(an)^4} r_e, \quad (3)$$

$$l_y = (an)^2 r_e, \quad (4)$$

where n is the principal quantum number of the contour, a is the inverse of the fine structure constant, m_e and r_e are the mass and classical radius of the electron, c_0 is the dimensionless speed of light equal to $c/[m/sec]$. Depending on the size of the contour, i.e. from its quantum number, its parameters vary, but the momentum (charge equivalent) in a closed counter remains constant. At the same time, *both the contour size and the parameters of the vortex tube have their ultimate values.*

In [6], in determining the neutrino mass, it was shown that the Planck size $r_h = (\hbar\gamma/c^3)^{1/2}$ has a physical meaning and is the limiting size inherent in the neutrino, and, obviously, in general for the microcosm, i.e. $r_{\min} = r_h = 1.62 \times 10^{-35}$ m or $5.74 \times 10^{-21} r_e$. Then from (1) and (3) we get other ultimate values: $n = 21700$ and $m_y = 8.83 \times 10^{12} m_e$. The boson mass is compared with that of mass-energy in units of

$m_e c^2$, provided that $v \rightarrow c$ (here the boson mass can be considered as the mass of the excited or “associated” vacuum). It is this condition that is satisfied for cosmic rays whose particles relative to their source move with velocities close to the speed of light. Thus, the energy equivalent of the mass m_j is $E = 8.83 \times 10^{12} \times 511000 = 4.51 \times 10^{18}$ eV.

This quantity is the ultimate energy for cosmic-ray protons. Obviously, for heavier nuclei, the energy increases in proportion to the atomic number A . This conclusion agrees with the fact of “weight increasing” the primary cosmic ray component with increasing energy, and the heavy nuclei flux (most likely iron) in the region of $\sim 10^{18}$ eV is much larger than that of protons [7–9]. Consequently, the largest energy value for the heaviest nuclei can not exceed $E \sim 3.7 \times 10^{20}$ eV and even higher values, apparently, can not be. Indeed, during the entire time of observation on Earth, only a few dozen events with energies above 10^{20} eV were recorded in various installations (the maximum energy of the cosmic particle 3×10^{20} eV was registered in October 1991 on the “Fly’s Eye” device [10]).

The figure adopted from [11] shows the observed spectrum of cosmic radiation, on which the energy limits for protons (II) and heavy nuclei (III) are noted (the values along the ordinate are reduced to the energy in GeV). The region of the graph is marked, where the intensity of cosmic rays is about 1 particle per square meter per year. A narrow scatter of the experimental data over the entire length of the spectrum, with the exception of the region of ultrahigh energies, gives grounds to assume that the intensity of cosmic rays depends slightly on the nature of their sources and the mechanism for their acceleration, and this can be shown.

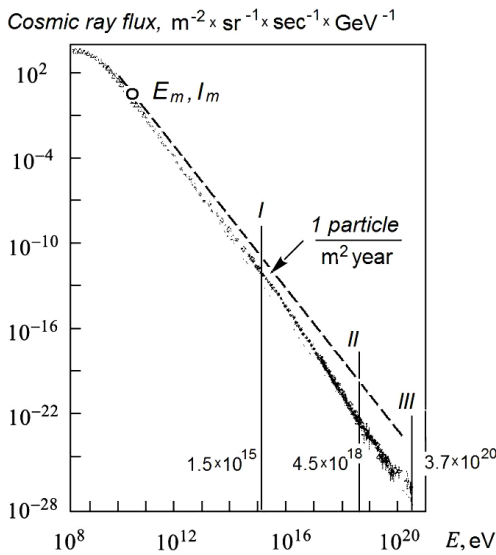


Fig. 1: The observed spectrum of cosmic radiation in the energy range 10^8 – 10^{20} eV.

Let us assume that the particle velocity increases proportionally to the distance from the source, and the number of

particles falling per unit area of the receiver is inversely proportional to the cube of the distance from the source. This is true in the case of unimpeded particle propagation. Then, by simple computations, we obtain a relation that is independent of the distance:

$$I = (E_m/E)^{1.5} I_m, \quad (5)$$

where E_m and I_m are the coordinates of some reference point on the $I(E)$ dependence in units of [eV] and [flux \times m $^{-2}$ \times sr $^{-1}$ \times sec $^{-1}$]. When the ordinates are divided by energy in GeV, formula (5) becomes:

$$I = 10^9 (E_m^{1.5}/E^{2.5}) I_m \quad (6)$$

and shown in the figure with a dashed line. The actual dependence is somewhat more steeply and approximated by the relation $dI/dE \sim E^{-2.7}$, which is explained by the presence of magnetic fields and other cosmogenic factors affecting charged particles. Nevertheless, it turns out that the shape of the energy spectrum is largely determined by the increase in the particles energy and the decrease in their number as radiation sources are removed from the Earth.

In the energy range 10^{15} – 10^{16} eV, the dependence $I(E)$ undergoes an inflection increasing index at E , the so-called “knee”. The energy value at the inflection point matches with the mass-energy of the contour corresponding to the *ultimate size of the hydrogen atom*. For this atom, the ultimate value of the quantum number $n = 390$ [5]. In general, detailed formula for the inflection point energy, given the results of [5], and assuming that the energy increases in proportion to the atomic number of nuclei can be represented as:

$$E_{\text{knee}} = 5.11 \times 10^5 \left(\frac{2\pi\gamma\rho_e m_p \times [\text{sec}^2]}{c_0^{1/3} \cos q_w} \right)^2 A = 1.46 \times 10^{15} \times A \text{ eV}, \quad (7)$$

where γ is the gravitational constant, $\rho_e = m_e/r_e^3$ is the electron density equal to 4.07×10^{13} kg/m 3 , m_p is the relative mass of the proton, and q_w is the Weinberg angle of 28.7° .

For protons, this energy value is indicated in the figure by the vertical (I), which matches with the beginning of the inflection of the energy spectrum. The removal of the inflection point towards higher energies for heavier nuclei is confirmed in [12].

One can propose the following explanation for the increase in the energy spectrum incline. At energies up to 1.46×10^{15} eV ($n < 390$), protons and electrons in cosmic rays can be in a bound state — either as atoms having a neutral charge or in some associations that have a total positive charge less than the protons total charge. It may reduce their interaction with magnetic fields.

At higher energies, protons are not accompanied by electrons, their total positive charge remains, and they are fully exposed to magnetic fields. Perhaps this is the reason for the

abrupt decrease in the number of electrons in the EAS when primary particles have energies about 10^{15} – 10^{16} eV [13].

As for the neutrinos, then, bearing in mind their inherent size limit of r_h , their maximum energy, possible, can reach the same value as that of the proton, 4.51×10^{18} eV. At the moment, the highest recorded neutrino energy is 2×10^{15} eV [14].

Conclusion

The ultimate energy of cosmic rays is limited by the maximum mass-energy of the proton vortex tube, which in turn is determined by the fundamental parameter — the Planck size inherent in a neutrino. The reason for the inflection of the spectrum of cosmic rays (the “knee”) is the obtaining by the proton of the energy at which a proton-electronic counter, having ultimate quantum number, opens. For other nuclei these energies increase in proportion to the atomic number of the element.

It is shown that, for all on a variety of radiation sources and the mechanism of acceleration of cosmic particles, the shape of the spectrum of cosmic rays, provided that they spread without interference, is largely determined by the most common factors — the increase in their particle energy and the decrease in their number — as the distance between the sources and the Earth is increasing.

Submitted on June 24, 2017

References

1. Kalashev O.E. Cosmic rays of ultrahigh and ultrahigh energies. Associated neutrino and photon radiation. 01.04.02 — theoretical physics. Thesis for the degree of Doctor of Physical and Mathematical Sciences. Moscow, 2016.
2. Greisen K. End to the cosmic ray spectrum? *Phys. Rev. Lett.*, 1966, v. 16, 748–750.
3. Zatsepin G.T., Kuzmin V.A. On the upper boundary of the spectrum of cosmic rays. *JETP-Letters*, 1966, v. 4, 78–80.
4. Belyakov A.V. Charge of the electron, and the constants of radiation according to J. A. Wheeler’s geometrodynamical model. *Progress in Physics*, 2010, v. 4, 90–94.
5. Belyakov A.V. Macro-analogies and gravitation in the micro-world: further elaboration of Wheeler’s model of geometrodynamics. *Progress in Physics*, 2012, v. 2, 47–57.
6. Belyakov A.V. Determination of the neutrino mass. *Progress in Physics*, 2016, v. 12, issue 1, 34–38.
7. Troitsky S.V. Cosmic rays of ultrahigh energies: composition and source problem. 01.04.16 — physics of the atomic nucleus and elementary particles. The dissertation author’s abstract on competition of a scientific degree of the doctor of physical and mathematical sciences. Institute of Nuclear Research, Russian Academy of Sciences, Moscow, 2008.
8. Grigorov N.L. et al. In: *Proc. 12th Int. Cosmic Ray Conf.*, Hobart, 1971, v. 5, 1746.
9. Isaev P.S. Some problems of the physics of cosmic rays of ultrahigh energies. P2-99-33. Joint Institute for Nuclear Research, Dubna, 1999.
10. Bird D.J. et al. *Astrophys. J.*, 1994, v. 424, 491.
11. Bednyakov V.A. Why research of cosmic rays of ultrahigh energies should be produced in a near-earth orbit. *Physics of Elementary Particles and the Atomic Nucleus*, Joint Institute for Nuclear Research, Dubna, 2002, v. 33, no. 5.
12. Kalmykov V.N. Mass composition of primary cosmic radiation in the region of the break according to the data of the installation EAS of the MSU. The dissertation and the author’s abstract on VAK 01.04.23 (Moscow, Russia), the candidate of physical and mathematical sciences.
13. Kulikov G.V., Christiansen G.B. *Journal of Experimental and Theoretical Physics*, 1958, v. 35, 635.
14. Aartsen et al. Evidence for astrophysical muon neutrinos from the Northern Sky with IceCube. *Physical Review Letters*, 2015, v. 115, 081102; arXiv: 1507.04005 [astro-ph.HE].

LETTERS TO PROGRESS IN PHYSICS

Cosmological Redshift in the De Sitter Stationary Universe

Larissa Borissova and Dmitri Rabounski

E-mail: borissova@ptep-online.com; rabounski@ptep-online.com

Here we focus on our previous studies, wherein we deduced the redshift formula in the de Sitter metric space. The non-Newtonian gravitational forces of repulsion, acting in the de Sitter universe, increase with distance. Thus these forces produce the redshift effect on photons coming from distant objects. The redshift in the de Sitter universe increases with distance from the observed objects, and is hyperbolic that matches with the non-linear redshift recently registered by astronomers. As a result, we no longer need the expanding model of the Friedmann metric to correctly explain the redshift in the spectra of galaxies and quasars. The observed “cosmological” redshift is as well good explained in the de Sitter universe which is stationary as is well known.

Earlier, we studied the metric of the inner space of a liquid sphere — the spherical space filled with an ideal incompressible liquid (the so-called Schwarzschild 2nd metric). The obtained results were published in all necessary detail in [1–3]. In particular, in our book *Inside Stars* [2] we considered stars as liquid spheres. Our computations made by the mathematical methods of the General Theory of Relativity showed a good coincidence with the observational data known in astronomy. We also showed, in the journal papers [1, 2] and in §1.2 of the book *Inside Stars* [2], that the liquid sphere metric transforms into the de Sitter metric (the metric of a spherical space filled with physical vacuum) under the following two common conditions. First, under the gravitational collapse condition, when the radius of the liquid sphere becomes equal to its gravitational radius (i.e. when the liquid sphere becomes gravitational collapsar). And second, when the space-time breaking matches with the radius of the liquid sphere. We also showed that the observed Universe is equivalent to a sphere in the state, which is very close to gravitational collapse (See Chapter 6 in [2] for detail). Thus the space of our Universe can be described by the metric of the de Sitter vacuum sphere. This means, in particular, that the non-Newtonian gravitational forces acting in the de Sitter metric space must manifest themselves in some astronomical phenomena observed in our Universe (read about the non-Newtonian forces of gravitational attraction and repulsion in §5.5 of our book *Fields, Vacuum and the Mirror Universe* [4]). For example, the non-Newtonian gravitational forces may also be the source of the observed redshift in the spectra of galaxies and quasars.

Now, this observed phenomenon is known as the “cosmological redshift” due to Lemaître who in 1927 showed [5] that such redshift may be originated due the Doppler effect on photons in an expanding universe (the universe of the Friedmann metric). On the other hand, proceeding from the aforementioned theoretical results [1–3] we can now state that the observed redshift in the spectra of galaxies and quasars has no relation to cosmology but is the “effect of distance” in the

stationary universe of the de Sitter metric. Such a redshift formula was derived in our publications [1–3]. But because those publications were focused on the internal constitution of stars, the redshift effect in the de Sitter space was not emphasized and analysed properly.

We now aim to emphasize it for better understanding of the obtained result.

The redshift formula is derived by integration of the scalar geodesic equation for photons. There are the scalar geodesic equation and the vectorial geodesic equation. They are the respective projections of the four-dimensional geodesic equation (the equation of motion along the shortest/geodesic lines) onto the time line and the three-dimensional spatial section of the observer. The scalar geodesic equation, the projection onto the time line, is the equation of energy. The vectorial geodesic equation is the equation of three-dimensional motion. So, integrating the scalar geodesic equation of a photon along its path, we obtain how its energy and, hence, its frequency changes during its travel. As a result, we obtain the redshift formula. As a matter of fact that the geodesic equations and, hence, their integration, depends on the metric of the particular space wherein the photons travel.

The three-dimensional sub-space of the de Sitter space (space-time) does not rotate and deform. But there is the gravitational inertial force. This force acting inside a sphere filled with physical vacuum, i.e. in the de Sitter space, in the radial coordinates takes the form (5.74) [4, §5.5]

$$F = \frac{\lambda c^2}{3} r = \frac{c^2}{a^2} r,$$

where $\lambda = \kappa\rho_0$ is the Einstein cosmological constant, κ is the Einstein gravitational constant, while ρ_0 is the density of the physical vacuum that fills the de Sitter space (see §5.3 [4]).

The Hubble constant $H = (2.3 \pm 0.3) \times 10^{-18} \text{ sec}^{-1}$ is expressed through the radius of the Universe $a = 1.3 \times 10^{28} \text{ cm}$ as $H = c/a$. Thus, we obtain (6.11) [1]

$$F = H^2 r,$$

where the Hubble constant plays the rôle of a fundamental frequency

$$H = \frac{2\pi}{T}$$

expressed through the time T of the existence of the Universe. So, the gravitational inertial force F acting in the de Sitter space depends the Hubble constant H .

Because $F > 0$ in the de Sitter space, this is a force of repulsion. This force is proportional to the radial distance r to the observer: each system of reference is connected with its own observer and his reference body, which is the “centre” of his own universe.

Consider the scalar and vectorial geodesic equations for a photon. This is the system of equations (6.22) [2]. Because the de Sitter space does not rotate and deform, the equations take the simplified form (6.23), where the photon is affected by only the gravitational inertial force and the space non-uniformity (expressed with the Christoffel symbols). Integrating the scalar geodesic equation (the equation of energy) for the photon travelling along the radial coordinate r in the de Sitter space, with taking the vectorial geodesic equation, we obtain the formula of the photon’s frequency ω (6.27) [2]

$$\omega = \frac{\omega_0}{\sqrt{1 - r^2/a^2}},$$

where $\omega_0 = \omega_{(r=0)}$ is the photon’s frequency in the coordinate origin $r=0$ (where the observer is located). We see that the photon’s frequency is asymptotically increasing when the photon’s source approaches to the event horizon (radius) of the Universe ($r=a$).

At distances much shorter than the Universe’s radius i.e. much shorter than the event horizon of the Universe ($r \ll a$), the formula for the photon’s frequency becomes (6.28)

$$\omega \approx \omega_0 \left(1 + \frac{r^2}{2a^2} \right).$$

That is we get the quadratic additive to the initially frequency of the photon or, in another word, the redshift effect z of parabolic type (6.29–6.31)

$$z = \frac{\omega - \omega_0}{\omega_0} = \frac{1}{\sqrt{1 - r^2/a^2}} - 1 \approx \frac{r^2}{2a^2} > 0,$$

which, in terms of the Hubble constant $H = c/a$, is

$$z \approx \frac{H^2 r^2}{2c^2}.$$

As is seen, the photon frequency shift is positive in this case: $z > 0$ (otherwise it would be blueshift). This means that the redshift effect takes place in the de Sitter universe. The space of the de Sitter metric is stationary: it neither expands nor compresses. The redshift effect in the de Sitter universe is due to the non-Newtonian gravitational force of repulsion.

In the last decades, astronomical observations of the most distant galaxies showed an increase of the redshift effect in the spectra of the most distant galaxies, which are located close to the event horizon. The astronomers supposed therefore, on the basis of the Friedmann metric of an expanding universe, that the space of our Universe expands with acceleration. On the other hand, the non-linear redshift at large distances is easily explained in the framework of the de Sitter static universe: see formula for z that above. This non-linear effect is due to only the non-linearity of the non-Newtonian gravitational force of repulsion acting on the photon. From the viewpoint of an earthy observer this effect looks as the increasing redshift with the increasing distance from the Earth to the observed object (the source of the photon).*

The observed high redshift in the spectra of quazars is as well explained due to the powerful inner non-Newtonian forces of repulsion (not the far intergalactic distances in the Friedmann expanding universe). As we conclude on the basis of our book *Inside Stars* [2], the ratio of the gravitational radius and the space breaking radius to the physical radius a (i.e. the ratio r_g/a and r_{br}/a) is close to 1 for neutron stars and quazars. If a star is in the state of gravitational collapse, the space breaking matches with both the gravitational radius of the star r_g and the star’s surface a , i.e. $a = r_g = r_{br}$. If the space breaking matches with only the star’s surface ($r_{br} = a$), gravitational collapse occurs at the radius

$$r_c = \sqrt{9a^2 - 8a^3/r_g}$$

(2.7) in [1]. The physical radius a of such a star is

$$r_g < a < 1.125 r_g$$

see (2.8–2.9) in [1]. In other words, neutron stars and quazars are objects in the state, which is very close to collapse. The latter means that the inner non-Newtonian gravitational force of repulsion is so strong near the surface of a neutron star or a quazar that photons emitted from its surface into the cosmos bear a high redshift independent on the distance from the observer. For this reason, quazars may be located not somewhere near the event horizon of our Universe, but somewhere much much closer to us.

In the end, a few words about our Universe as a whole. According to the contemporary astronomical data, its average density is $\sim 10^{-29}$ g/cm³, while the ultimate large observed distance (the radius of the Universe, or the event horizon) is $\sim 1.3 \times 10^{28}$ cm. With such characteristics, the collapse radius is $\sim 1.2 \times 10^{28}$ cm (a little lesser than the event horizon,

*This conclusion on the unnecessary of the Friedmann metric meets another study [6–8] showing that the observed redshift, including its non-linearity, may be caused by the light-speed rotation of the isotropic space (the partially degenerate space, wherein light-like particles e.g. photons travel). The found basic redshift effect in a flat space has the form of exponent, while the particular space metrics make only an additional goal to it.

while the space breaking radius is the same as the event horizon $\sim 1.3 \times 10^{28}$ cm. These observed facts mean that we live in the inner space of an object which is either collapsar or is in the state which is very close to the state of collapse. The description of such an object anyhow excludes the expanding model. That is the Friedmann metric of an expanding universe is non-applicable to the observed Universe.

Finally, the observed non-linear redshift in the spectra of galaxies and quazars is well explained in the de Sitter stationary space, wherein it is merely a “distant effect” due to the non-Newtonian forces of repulsion which increase with distance from the observer. The de Sitter universe is stationary — it is a bubble that has closed space and time on itself, and is floating in the surrounding outer space (because we have no reason to assert that our Universe exists in isolation as an exceptional object).

Submitted on December 5, 2017

References

1. Borissova L. De Sitter bubble as a model of the observable Universe. *The Abraham Zelmanov Journal*, 2010, v.3, 3–24.
2. Borissova L. and Rabounski D. Inside Stars: A Theory of the Internal Constitution of Stars, and the Sources of Stellar Energy According to General Relativity. 2nd Edition, American Research Press, Rehoboth (NM), 2014.
3. Borissova L. A telemetric multispace formulation of Riemannian geometry, General Relativity, and cosmology: implications for relativistic cosmology and the true reality of time. *Progress in Physics*, 2017, v.13. Issue 2, 57–75.
4. Borissova L. and Rabounski D. Fields, Vacuum, and the Mirror Universe. 2nd edition, Svenska fysikarkivet, Stockholm, 2009.
5. Block D.L. Georges Lemaître and Stiglers Law of Eponymy. arXiv: 1106.3928.
6. Rabounski D. An explanation of Hubble redshift due to the global non-holonomy of space. *Progress in Physics*, 2009, v. 5, issue 1, L1–L2.
7. Rabounski D. Hubble redshift due to the global non-holonomy of space. *The Abraham Zelmanov Journal*, 2009, v. 2, 11–28.
8. Rabounski D. Non-linear cosmological redshift: the exact theory according to General Relativity. *The Abraham Zelmanov Journal*, 2012, v. 5, 4–30.

Nuclear Structure of $^{154,156}\text{Dy}$ Isotopes

Salah A. Eid¹, Sohair M. Diab²

¹Faculty of Engineering, Phys. Dept., Ain Shams University, Cairo, Egypt.

²Faculty of Education, Phys. Dept., Ain Shams University, Cairo, Egypt.

E-mail: mppe2@yahoo.co.uk

The Interacting Boson Approximation model, *IBA-1*, has been used in studying the nuclear structure of $^{154,156}\text{Dy}$. The excited positive and negative parity states, potential energy surfaces, $V(\beta, \gamma)$, electromagnetic transition probabilities, $B(E1)$, $B(E2)$, back bending, staggering effect, $\Delta I = 1$, and electric monopole strength, $X(E0/E2)$, were calculated successfully. The calculated values are compared to the available experimental data and show reasonable agreement. The energy and electromagnetic transition probabilities ratios as well as the contour plot of the potential energy surfaces show that the ^{156}Dy nucleus is an $X(5)$ candidate.

1 Introduction

The nuclear shape and shape phase transitions in the rare earth dysprosium isotopes have been investigated by many authors theoretically and experimentally. Theoretically, analytical solution of the Bohr Hamiltonian derived with the Titz-Hua potential [1] as well as Bohr-Mottelson Hamiltonian [2,3] were used in calculating energy levels, spin, parity and electromagnetic ratios. The effect of the nuclear structure on the α -decay are investigated by many authors [4-6] and found that the shape and deformation has an effect on the branching ratio as well as the change in the half-life of α -emission. Experimentally, the low-lying positive and negative parity states were produced in the ^{148}Nd ($^{12}\text{C}, 4n$), ^{155}Gd ($^3\text{He}, 4n$), $E = 37.5$ MeV, ^{122}Sn ($^{36}\text{S}, 4n$), $E = 165$ MeV and ^{114}Cd ($^{48}\text{Ca}, 6n$), $E = 215$ MeV [7-9] reactions. The levels' energy, spin, parity, γ -bands, branching ratios, level energy differences between the positive and negative parity bands, octupole deformation, γ - γ coincidences and angular distribution were measured. Conversion electrons were detected by mini-orange spectrometer, $E0$ transitions were observed and the strength of the electric monopole transitions were calculated [10].

$X(5)$ is the critical point symmetry of phase transition between $U(5)$ and $SU(3)$ nuclei. The aim of the present work is to:

1. Calculate the potential energy surfaces, $V(\beta, \gamma)$;
2. Calculate the levels' energy and electromagnetic transition rates $B(E1)$ and $B(E2)$;
3. Show $X(5)$ symmetry to ^{156}Dy ;
4. Calculate the back bending;
5. Calculate the staggering effect, and
6. Calculate the electric monopole strength, $X(E0/E2)$.

2 Interacting Boson Approximation model *IBA-1*

2.1 Levels' energy

The *IBA-1* Hamiltonian [11] employed on $^{154,156}\text{Dy}$, in the present calculation, is:

$$H = EPS \cdot n_d + PAIR \cdot (P \cdot P) + \frac{1}{2} ELL \cdot (L \cdot L) + \frac{1}{2} QQ \cdot (Q \cdot Q) + 5 OCT \cdot (T_3 \cdot T_3) + 5 HEX \cdot (T_4 \cdot T_4), \quad (1)$$

where

$$P \cdot P = \frac{1}{2} \left[\begin{array}{c} \{(s^\dagger s^\dagger)_0^{(0)} - \sqrt{5}(d^\dagger d^\dagger)_0^{(0)}\} x \\ \{(ss)_0^{(0)} - \sqrt{5}(\tilde{d}\tilde{d})_0^{(0)}\} \end{array} \right]_0^{(0)}, \quad (2)$$

$$L \cdot L = -10\sqrt{3} \left[(d^\dagger \tilde{d})^{(1)} x (d^\dagger \tilde{d})^{(1)} \right]_0^{(0)}, \quad (3)$$

$$Q \cdot Q = \sqrt{5} \left[\begin{array}{c} \{(S^\dagger \tilde{d} + d^\dagger s)^{(2)} - \frac{\sqrt{7}}{2} (d^\dagger \tilde{d})^{(2)}\} x \\ \{(s^\dagger \tilde{d} + +\tilde{d}s)^{(2)} - \frac{\sqrt{7}}{2} (d^\dagger \tilde{d})^{(2)}\} \end{array} \right]_0^{(0)}, \quad (4)$$

$$T_3 \cdot T_3 = -\sqrt{7} \left[(d^\dagger \tilde{d})^{(2)} x (d^\dagger \tilde{d})^{(2)} \right]_0^{(0)}, \quad (5)$$

$$T_4 \cdot T_4 = 3 \left[(d^\dagger \tilde{d})^{(4)} x (d^\dagger \tilde{d})^{(4)} \right]_0^{(0)}. \quad (6)$$

and n_d is the number of d bosons; $P \cdot P$, $L \cdot L$, $Q \cdot Q$, $T_3 \cdot T_3$ and $T_4 \cdot T_4$ represent pairing, angular momentum, quadrupole, octupole and hexadecupole interactions respectively between the bosons; EPS is the boson energy; and $PAIR$, ELL , QQ , OCT , HEX are the strengths of the pairing, angular momentum, quadrupole, octupole and hexadecupole interactions respectively, Table 1.

nucleus	<i>EPS</i>	<i>PAIR</i>	<i>ELL</i>	<i>QQ</i>	<i>OCT</i>	<i>HEX</i>	<i>E2SD(eb)</i>	<i>E2DD(eb)</i>
¹⁵⁴ Dy	0.6240	0.000	0.0084	-0.0244	0.0000	0.0000	0.1510	-0.4467
¹⁵⁶ Dy	0.4450	0.000	0.0084	-0.0244	0.0000	0.0000	0.1274	-0.3769

Table 1: Parameters used in IBA-1 Hamiltonian (all in MeV).

nucleus	$E_{4_1^+}/E_{2_1^+}$	$E_{6_1^+}/E_{2_1^+}$	$E_{8_1^+}/E_{2_1^+}$	$E_{0_2^+}/E_{2_1^+}$	$E_{6_1^+}/E_{0_2^+}$	$E_{0_3^+}/E_{2_1^+}$	$BE2(4_1^+ - 2_1^+)/BE2(2_1^+ - 0_1^+)$
¹⁵⁴ Dy	2.09	3.12	4.86	2.12	1.46	2.95	1.91
¹⁵⁶ Dy	2.86	5.36	8.43	6.15	0.87	8.78	1.56
<i>X</i> (5)	3.02	5.83	9.29	5.65	1.53	6.03	1.58

Table 2: Energy and transition probability ratios.

2.2 Transition rates

The electric quadrupole transition operator employed is:

$$T^{(E2)} = E2SD \cdot (s^\dagger \tilde{d} + d^\dagger s)^{(2)} + \frac{1}{\sqrt{5}} E2DD \cdot (d^\dagger \tilde{d})^{(2)}. \quad (7)$$

E2SD and *E2DD* are adjustable parameters.

The reduced electric quadrupole transition rates between $I_i \rightarrow I_f$ states are given by:

$$B(E2, I_i - I_f) = \frac{[\langle I_f || T^{(E2)} || I_i \rangle]^2}{2I_i + 1}. \quad (8)$$

3 Results and discussion

3.1 The potential energy surfaces

The potential energy surfaces [12], $V(\beta, \gamma)$, as a function of the deformation parameters β and γ are calculated using:

$$\begin{aligned} E_{N_\pi N_\nu}(\beta, \gamma) &= \langle N_\pi N_\nu; \beta\gamma | H_{\pi\nu} | N_\pi N_\nu; \beta\gamma \rangle = \\ &= \zeta_d (N_\nu N_\pi) \beta^2 (1 + \beta^2) + \beta^2 (1 + \beta^2)^{-2} \times \\ &\times \left\{ k N_\nu N_\pi [4 - (\bar{X}_\pi \bar{X}_\nu) \beta \cos 3\gamma] \right\} + \\ &+ \left\{ [\bar{X}_\pi \bar{X}_\nu \beta^2] + N_\nu (N_\nu - 1) \left(\frac{1}{10} c_0 + \frac{1}{7} c_2 \right) \beta^2 \right\}, \end{aligned} \quad (9)$$

where

$$\bar{X}_\rho = \left(\frac{2}{7} \right)^{0.5} X_\rho, \quad \rho = \pi \text{ (proton) or } \nu \text{ (neutron)}, \quad (10)$$

and ζ_d : the energy of *d* bosons.

The calculated potential energy surfaces, $V(\beta, \gamma)$, are presented in Figs. 1, 2. Fig. 1 shows that ¹⁵⁴Dy is a vibrational-like nucleus, U(5), while ¹⁵⁶Dy nucleus is deviated from vibrational-like to rotational-like with slight prolate deformation, SU(3), Fig. 2. The levels' energy, transition probability ratios presented in Table 2, as well as the potential energy surfaces, are in favour to consider ¹⁵⁶Dy as an *X*(5) candidate.

$I_i^- I_f^+$	B (E2)	$I_i^- I_f^+$	B (E1)
2 ₁ 0 ₁	0.4744	1 ₁ 0 ₁	0.0282
2 ₂ 0 ₁	0.0100	1 ₁ 0 ₂	0.1336
2 ₂ 0 ₂	0.3040	3 ₁ 2 ₁	0.1683
3 ₁ 2 ₁	0.0198	3 ₁ 2 ₂	0.0658
4 ₁ 2 ₁	0.9074	3 ₂ 2 ₁	0.0069
3 ₁ 2 ₂	0.2666	3 ₂ 2 ₂	0.0235
4 ₂ 4 ₁	0.1409	3 ₂ 2 ₃	0.1520
4 ₂ 2 ₁	0.0017	5 ₁ 4 ₁	0.3035
4 ₂ 2 ₂	0.5520	5 ₁ 4 ₂	0.0698
6 ₁ 4 ₁	1.1581	7 ₁ 6 ₁	0.4380
6 ₂ 4 ₁	0.0005	7 ₁ 6 ₂	0.0665
6 ₂ 4 ₂	0.8200	9 ₁ 8 ₁	0.5734
8 ₁ 6 ₁	1.2916	9 ₁ 8 ₂	0.0610
8 ₁ 6 ₂	0.0700	9 ₂ 8 ₁	0.1750
8 ₁ 6 ₃	0.0641	9 ₂ 8 ₂	0.3501
8 ₂ 6 ₂	0.9584	9 ₂ 8 ₃	0.2144
10 ₁ 8 ₁	1.3384	11 ₁ 10 ₁	0.7103
10 ₁ 8 ₂	0.0579	11 ₁ 10 ₂	0.0543

Table 3: Calculated *B*(E2) and *B*(E1) in ¹⁵⁴Dy.

3.2 Energy spectra and electric transition rates

The energy of the positive and negative parity states of isotopes ^{154,156}Dy are calculated using computer code PHINT [11]. A comparison between the experimental spectra [13,14] and our calculations, using values of the model parameters given in Table 1 for the ground state, $\beta_1, \beta_2, \gamma_1$ and γ_2 bands are illustrated in Figs. 3, 4. The agreement between the calculated levels' energy and their corresponding experimental values are fair, but they are slightly higher especially for the higher excited states. We believe this is due to the change of the projection of the angular momentum which is due mainly to band crossing. Fig. 5 shows the position of *X*(5) and *E*(5) between the other types of nuclei.

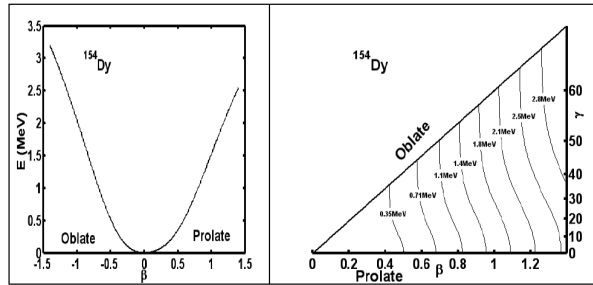


Fig. 1: Potential energy surfaces for ^{154}Dy .

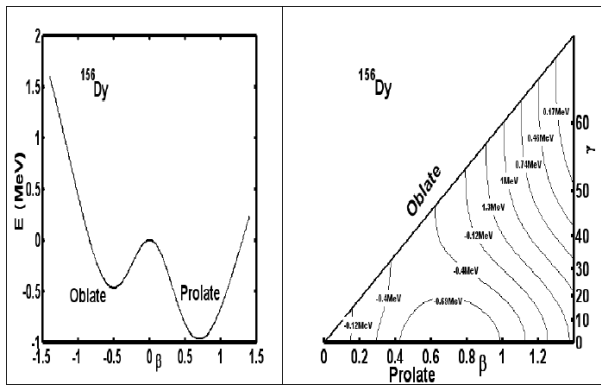


Fig. 2: Potential energy surfaces for ^{156}Dy .

$I_i^+ I_f^+$	$B(E2)$	$I_i^- I_f^+$	$B(E1)$
2 ₁ 0 ₁	0.7444	1 ₁ 0 ₁	0.1309
2 ₂ 0 ₁	0.0023	1 ₁ 0 ₂	0.0696
2 ₂ 0 ₂	0.4652	3 ₁ 2 ₁	0.2353
3 ₁ 2 ₁	0.0169	3 ₁ 2 ₂	0.0854
4 ₁ 2 ₁	1.1073	3 ₂ 2 ₁	0.0481
3 ₁ 2 ₂	0.0026	3 ₂ 2 ₂	0.0092
4 ₂ 4 ₁	0.0356	3 ₂ 2 ₃	0.0110
4 ₂ 2 ₁	0.0016	5 ₁ 4 ₁	0.3934
4 ₂ 2 ₂	0.0041	5 ₁ 4 ₂	0.0778
6 ₁ 4 ₁	1.2446	7 ₁ 6 ₁	0.5149
6 ₂ 4 ₁	0.0007	7 ₁ 6 ₂	0.0675
6 ₂ 4 ₂	0.9083	9 ₁ 8 ₁	0.6377
8 ₁ 6 ₁	1.3003	9 ₁ 8 ₂	0.0585
8 ₁ 6 ₂	0.0410	9 ₂ 8 ₁	0.0129
8 ₁ 6 ₃	0.0162	9 ₂ 8 ₂	0.3474
8 ₂ 6 ₂	0.9817	9 ₂ 8 ₃	0.2687
10 ₁ 8 ₁	1.3025	11 ₁ 10 ₁	0.7631
10 ₁ 8 ₂	0.0332	11 ₁ 10 ₂	0.0507

Table 4: Calculated $B(E1)$ and $B(E2)$ in ^{156}Dy .

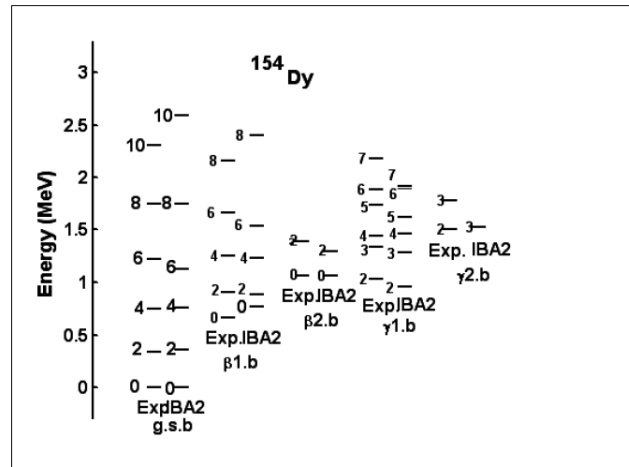


Fig. 3: Experimental[13] and calculated levels' energy.

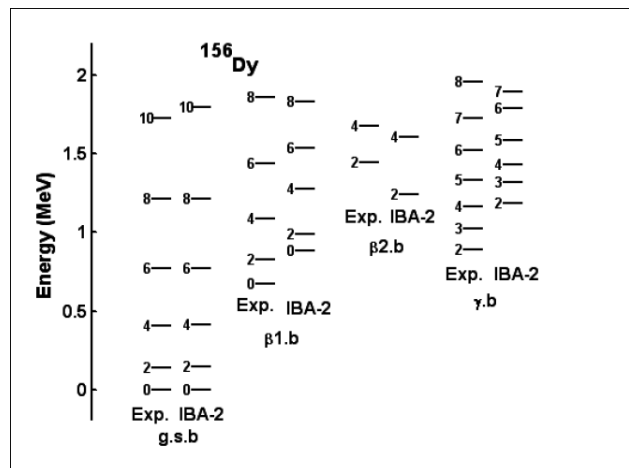
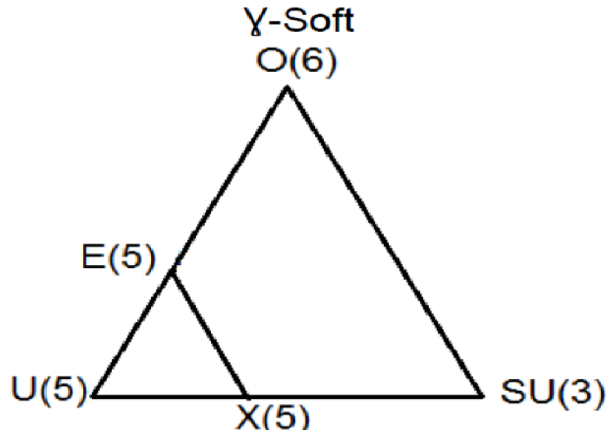
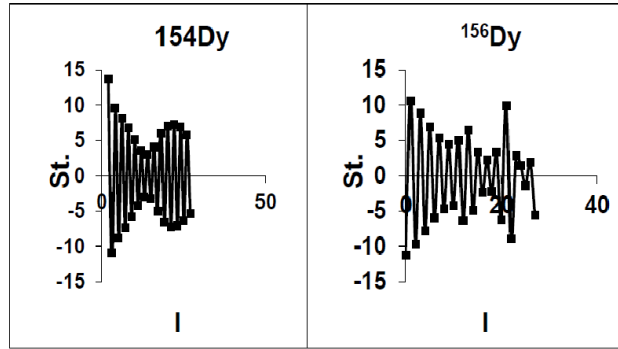


Fig. 4: Experimental[14] and calculated levels' energy.

Unfortunately there is no available measurements of electromagnetic transition rates $B(E2)$ for $^{154,156}\text{Dy}$ nuclei. The only measured values of $B(E2, 2_1^+ \rightarrow 0_1^+)$ for $^{154,156}\text{Dy}$ [15] are used in normalizing our calculated values presented in Tables 3, 4. Also, there is no experimental data available for $B(E1, I^- \rightarrow I^+)$ for normalization. Parameters $E2SD$ and $E2DD$ displayed in Table 1 are used in the computer code FBEM [11] for calculating the electromagnetic transition rates. No new parameters are introduced for calculating electromagnetic transition rates $B(E1)$ and $B(E2)$ of intraband and interband.

3.3 Staggering effect

The presence of positive and negative parity states has encouraged us to study the staggering effect [16] for $^{154,156}\text{Dy}$ isotopes using staggering functions (11) and (12) with the

Fig. 5: Triangle showing the position of $X(5)$ and $E(5)$.Fig. 6: Staggering effect on ^{154}Dy and ^{156}Dy .

help of the available experimental data [13,14].

$$St(I) = 6 \Delta E(I) - 4 \Delta E(I-1) - 4 \Delta E(I+1) + \Delta E(I+2) + \Delta E(I-2), \quad (11)$$

with

$$\Delta E(I) = E(I+1) - E(I). \quad (12)$$

The calculated staggering patterns are illustrated in Fig. 6 and show an interaction between the positive and negative parity states for the ground state band of $^{154,156}\text{Dy}$.

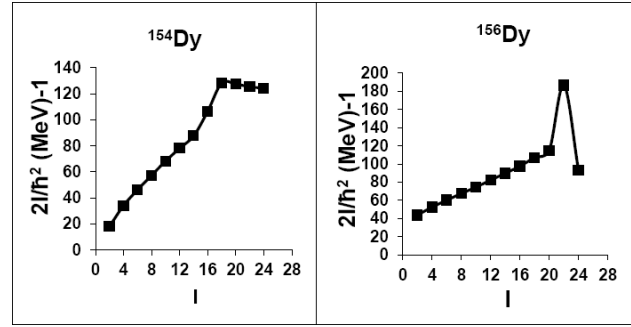
3.4 Back bending

The moment of inertia J and energy parameters $\hbar\omega$ are calculated using (13) and (14):

$$\frac{2J}{\hbar^2} = \frac{4I-2}{\Delta E(I \rightarrow I-2)}, \quad (13)$$

$$(\hbar\omega)^2 = (I^2 - I + 1) \left[\frac{\Delta E(I \rightarrow I-2)}{(2I-1)} \right]^2. \quad (14)$$

The plots in Fig. 7 show forward bending for ^{154}Dy at $I^+ = 18$ and upper bending at $I^+ = 22$ for ^{156}Dy . Bending in higher states may be explained as due to band crossing.

Fig. 7: Back bending ^{154}Dy and ^{156}Dy .

I_i^+	I_f^+	I_f^-	^{154}Dy	^{156}Dy
0 ₂	0 ₁	2 ₁	0.0778	0.3526
0 ₃	0 ₂	2 ₂	0.2455	0.0285
0 ₃	0 ₁	2 ₂	0.0108	6.9000
0 ₄	0 ₃	2 ₃	0.1403	0.0000
0 ₄	0 ₂	2 ₃	0.0363	1.7686
0 ₄	0 ₁	2 ₃	0.0247	0.1903
2 ₂	2 ₁	0 ₂	2.4500	1.3870
2 ₃	2 ₁	0 ₂	0.2679	0.0454
2 ₃	2 ₂	0 ₂	0.1114	2.2727
4 ₃	4 ₁	2 ₃	0.0434	0.0785
4 ₃	4 ₂	2 ₃	0.0193	1.4117
4 ₄	4 ₁	2 ₃	0.0303	0.3177
4 ₄	4 ₂	2 ₃	5.3636	0.254
4 ₂	4 ₁	2 ₂	0.2384	0.0027
6 ₂	6 ₁	4 ₂	0.2422	0.1347
8 ₂	8 ₁	6 ₂	0.0609	0.0173
10 ₂	10 ₁	8 ₂	0.0337	0.0134

Table 5: $X_{if'f}(E0/E2)$ ratios in $^{154,156}\text{Dy}$.

3.5 Electric monopole transitions

The electric monopole transitions, $E0$, are normally occurring between two states of the same spin and parity by transferring energy and zero unit of angular momentum. The strength of the electric monopole transition, $X_{if'f}(E0/E2)$ [17] can be calculated using (15) and (16) and are presented in Table 5

$$X_{if'f}(E0/E2) = \frac{B(E0, I_i - I_f)}{B(E2, I_i - I_f)}, \quad (15)$$

where $I_i = I_f=0$, $I_f=2$ and $I_i = I_f \neq 0$, $I_f = I_f$.

$$X_{if'f}(E0/E2) = (2.54 \times 10^9) A^{3/4} \frac{E_\gamma^5(\text{MeV})}{\Omega_{KL}} \times \alpha(E2) \frac{T_e(E0, I_i - I_f)}{T_e(E2, I_i - I_f)}, \quad (16)$$

A : mass number;

I_i : spin of the initial state where $E0$ and $E2$ transitions are depopulating it;

I_f : spin of the final state of $E0$ transition;

I'_f : spin of the final state of $E2$ transition;

E_γ : gamma ray energy;

Ω_{KL} : electronic factor for K, L shells [18];

$\alpha(E2)$: conversion coefficient of the $E2$ transition;

$T_e(E0, I_i - I_f)$: absolute transition probability of the $E0$ transition between I_i and I_f states; and

$T_e(E2, I_i - I'_f)$: absolute transition probability of the $E2$ transition between I_i and I'_f states.

Unfortunately, there is no experimental data available for comparison with the calculated values.

3.6 Conclusions

The $IBA-1$ model has been applied successfully to $^{154,156}\text{Dy}$ isotopes and:

1. Levels' energy are successfully reproduced;
2. Potential energy surfaces are calculated and show vibrational-like characteristics to ^{154}Dy and slight prolate deformation to ^{156}Dy ;
3. Electromagnetic transition rates $B(E1)$ and $B(E2)$ are calculated;
4. Bending has been observed at $I^+ = 18$ for ^{154}Dy and at $I^+ = 22$ for ^{156}Dy ;
5. Staggering effect has been calculated and beat patterns observed which show an interaction between the positive and negative parity states;
6. Strength of electric monopole transitions $X_{if'}(E0/E2)$ are calculated; and
7. The potential energy surfaces, transition probability rates and energy show that ^{156}Dy has the $X(5)$ symmetry.

Received on November 28, 2017

References

1. Chabab M., El Batoul A., Hamzavi M., Lahbas A., Oulne M. Excited collective states of nuclei within Bohr Hamiltonian with Tietz-Hua potential. *Eur. Phys. J. A*, 2017, v. 53, 157.
2. Baganu P. and Budaca R. Sextic potential for γ -rigid prolate nuclei. *J. Phys. G*, 2015, v. 42, 105106.
3. Alimohammadi M., Zare S. Investigation of Bohr-Mottelson Hamiltonian in γ -rigid version with position dependent mass. *Nucl. Phys. A*, 2017, v. 960, 78.
4. Xiao-Dong Sun, Ping Guo, and Xiao-Hua Li. Systematic study of α -decay half-lives for even-even nuclei within a two-potential approach. *Phys. Rev. C*, 2016, v. 93, 034316.
5. Li Z.P., Niksic T. and Vretenar D. Coexistence of nuclear shapes: self-consistent mean-field and beyond. *J. Phys. G*, 2015, v. 43, 024005.
6. Giriya K. K. Role of shape and quadrupole deformation of parents in the cluster emission of rare earth nuclei. *Int. J. Mod. Phys. E*, 2014, v. 23, 1450002.
7. Zimba G. L., Sharpey-Schafer J. F., Jones P., Bvumbi S. P., Masiteng L. P., Majola S. N. T., Dinoko T. S., Lawrie E. A., Lawrie J. J., Negi D., Papka P., Roux D., Shirinda O., Easton J. E., Khumalo N. A. Octupole correlations in $N=88$ ^{154}Dy : Octupole vibration versus stable deformation. *Phys. Rev. C*, 2016, v. 94, 054303.
8. Ijaz Q. A., Ma W. C., Abusara H., Afanasjev A. V., Xu Y. B., Yadav R. B., Zhang Y. C., Carpenter M. P., Janssens R. V. F., Khoo T. L., Lauritsen T., Nisius D. T. Excited superdeformed bands in ^{154}Dy and cranked relativistic mean field interpretation. *Phys. Rev. C*, 2009, v. 80, 034322.
9. Paul E. S., Rigby S. V., Riley M. A., Simpson J., Appelbe D. E., Campbell D. B., Choy P. T. W., Clark R. M., Cromaz M., Evans A. O., Fallon P., Gorgen A., Joss D. T., Lee I. Y., Macchiavelli A. O., Nolan P. J., Pipidis A., Ward D., Ragnarsson I. Loss of collectivity in the transitional ^{156}Er nucleus at high spin. *Phys. Rev. C*, 2009, v. 79, 044324.
10. Blasi N., Atanasova L., Balabanski D., Das Gupta S., Gladinski K., Guerro L., Nardelli S., and Saltarelli A. $E0$ decay from the first 0^+ state in ^{156}Dy and ^{160}Er . *Phys. Rev. C*, 2014, v. 90, 044317.
11. Scholten O. The program package PHINT (1980) version. Internal report KVI-63, Keryfysisch Versneller Instituut, Gronigen, 1979.
12. Ginocchio J. N. and Kirson M. W. An intrinsic state for the interacting boson model and its relationship to the Bohr-Mottelson approximation. *Nucl. Phys. A*, 1980, v. 350, 31.
13. Reich C. W. ADOPTED LEVELS, GAMMAS for ^{154}Dy . *Nuclear Data Sheets*, 2009, v. 110, 2257.
14. Reich C. W. ADOPTED LEVELS, GAMMAS for ^{156}Dy . *Nuclear Data Sheets*, 2012, v. 113, 2537.
15. Pritychenko B., Birch M., Singh B. and Horoi M. Tables of $E2$ transition probabilities from the first 2^+ states in even-even nuclei. *Atomic Data and Nuclear Data Tables*, 2016, v. 107, 1.
16. Minkov N., Yotov P., Drenska S. and Scheid W. Parity shift and beat staggering structure of octupole bands in a collective model for quadrupole-octupole deformed nuclei. *J. Phys. G*, 2006, v. 32, 497.
17. Rasmussen J. O. Theory of $E0$ transitions of spheroidal nuclei. *Nucl. Phys.*, 1960, v. 19, 85.
18. Bell A. D., Avelo C. E., Davidson M. G. and Davidson J. P. Table of $E0$ conversion probability electronic factors. *Can. J. Phys.*, 1970, v. 48, 2542.

Soliton-effect Spectral Self-compression for Different Initial Pulses

Armine Grigoryan¹, Aghavni Kutuzyan², and Garegin Yesayan³

Chair of Optics, Department of Physics, Yerevan State University, 1 Alex Manoogian, 0025 Yerevan, Armenia.

E-mails: ¹arminegrigor@gmail.com, ²akutuzyan@ysu.am, ³gyesayan@ysu.am

Our numerical studies demonstrate a spectral analogue of soliton-effect self-compression for different initial pulses. The evolution of transform-limited pulses during the propagation in a single-mode fiber with anomalous dispersion is studied. It is shown that the spectral analogue of soliton-effect self-compression is realized in the case of different initial pulses: periodicity of the spectral compression and stretching is different for different initial pulses. The approximation of curves introducing the frequency of the spectral compression and stretching dependence on nonlinearity parameter is implemented.

1 Introduction

The spectral compression (SC) process has numerous interesting applications in ultrafast optics and laser technology [1–5], such as the spectrotemporal imaging of ultrashort pulses by means of Fourier transformation [1]. In [5], the authors offer to apply SC in a fiber laser instead of strong spectral filtering. This allows to obtain transform-limited pulses and benefits the laser's power efficiency. As another practical application of SC, it is important to mention the transfer of femtosecond pulses without distortion at a relatively large distance [6]. Diverse applications of SC remain urgent in relation to the development and analysis of new effective compression systems. For example, in [7] the compression efficiency is improved by means of amplitude modulation.

The traditional spectral compressor consists of prism as a dispersive delay line, where the pulse is stretched and negatively chirped, and single-mode fiber (SMF) with the normal group-velocity dispersion, where nonlinear self-phase modulation leads to the chirp compensation and spectral narrowing. At the wavelength range of $<1.3 \mu\text{m}$, the group-velocity dispersion is positive for standard silica fibers. The role of the normal dispersion in SC of subpicosecond laser pulses is analyzed in [8]. As it is known, the combined impact of negative dispersion and the nonlinear self-phase modulation leads to the formation of solitons in SMF [9, 10], when the impact of dispersion and nonlinear self-phase modulation balance each other out. The pulse self-compression phenomenon is also known [11], which is obtained when the impact of the nonlinear self-phase modulation exceeds the dispersion. Under the opposite condition, i.e. when the impact of dispersion exceeds the nonlinearity, we can expect spectral self-compression (self-SC) by the analogy of the pulse self-compression. Recently, the self-SC implementation directly in a fiber with negative group-velocity dispersion (at the wavelength range $\geq 1.3 \mu\text{m}$ for standard silica fibers) was proposed [12] and studied [13]. In this work, we carried out detailed numerical studies on the process of soliton-effect self-SC for different initial pulses. Simulations were carried out for initial Gaussian and secant-hyperbolic pulses. We

have shown the soliton-effect self-SC in the fiber “directly”, without dispersive delay line, in the fiber with anomalous dispersion for different initial pulses. It is shown that there is an analogy between the processes of soliton self-compression and soliton-effect self-SC for different initial pulses: the periodicity of the process changes in the case of different initial pulses. The studies show that the periodicity of the process decreases when the nonlinearity parameter reduces. Our detailed study has shown that the frequency of compression has polynomial and exponential approximations.

2 Numerical studies and results

In the SMF, the pulse propagation is described by the nonlinear Schrödinger equation for normalized complex amplitude of field, considering only the influence of group-velocity dispersion and Kerr nonlinearity [14]:

$$i \frac{\partial \psi}{\partial \zeta} = \frac{1}{2} \frac{\partial^2 \psi}{\partial \eta^2} + R |\psi|^2 \psi \quad (1)$$

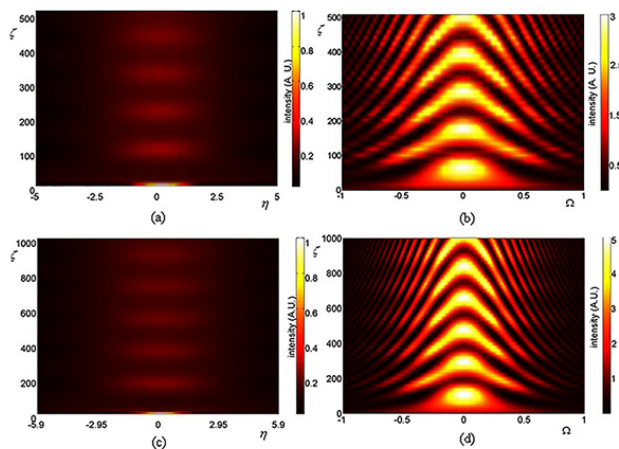


Fig. 1: The 3D map of the propagation of Gaussian (a, b) and secant-hyperbolic (c, d) pulses and its spectra. $\Omega = (\omega - \omega_0)/\Delta\omega_0$.

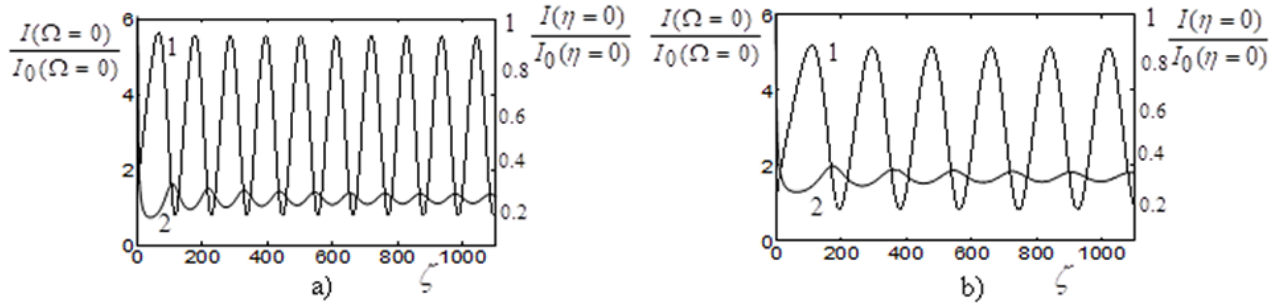


Fig. 2: The peak values of spectra (1) and pulses (2) vs fiber length for initial Gaussian (a) and secant-hyperbolic (b) pulses.

where $\zeta = z/L_D$ is the dimensionless propagation distance, $\eta = (t - z/u)/\tau_0$ is the running time, which are normalized to the dispersive length $L_D = \tau_0^2/|k_2|$ (k_2 is the coefficient of second-order dispersion), and initial pulse duration τ_0 , respectively. The nonlinearity parameter R is given by the expression $R = L_D/L_{NL}$, where $L_{NL} = (k_0 n_2 I_0)^{-1}$ is the nonlinearity length, n_2 is the Kerr index of silica, I_0 is the peak intensity. The first and second terms of the right side of (1) describe the impact of group-velocity dispersion and nonlinearity, respectively. We use the split-step Fourier method during the numerical solution of the equation, with the Fast Fourier Transform algorithm on the dispersive step [15, 16].

The objective of our numerical studies is the soliton-effect self-SC, which takes place when the dispersive length in the fiber is shorter than the nonlinear length ($L_D < L_{NL}$, i.e. $R < 1$). Therefore, at first, the group-velocity dispersion stretches the pulse by acquiring a chirp. Afterwards, the accumulated impact of nonlinear self-phase modulation leads to the compensation of the chirp. As a result, the spectrum is compressed. The process has periodic character. We study the pulse behavior in a fiber with negative group-velocity dispersion for different initial pulses and different values of the nonlinearity parameter and fiber length.

Fig. 1 illustrates the process of propagation of Gaussian (a, b, $R = 0.6$) and secant-hyperbolic (c, d, $R = 0.4$) pulses and their spectra. In this case, we study the process for short fiber lengths where the efficiency of the process is high for the nonlinearity parameter values of $R = 0.6$ (Gaussian pulse) and $R = 0.4$ (secant-hyperbolic pulse). It can be observed that the pulse is stretched and the spectrum is compressed in the initial propagation step. Afterwards, the width of central peak of the spectrum decreases and the main part of the pulse energy goes to the spectral satellites. At the certain fiber length, the reverse process starts the pulse self-compression.

The process can be explained in the following way: in the initial propagation step the spectrum is compressed, which leads to the decreasing of dispersion impact. As a result, the dispersive length increases, therefore, the nonlinearity parameter also increases. When the condition $R > 1$ is satisfied ($L_D > L_{NL}$), the pulse is compressed. Then, the spectrum is

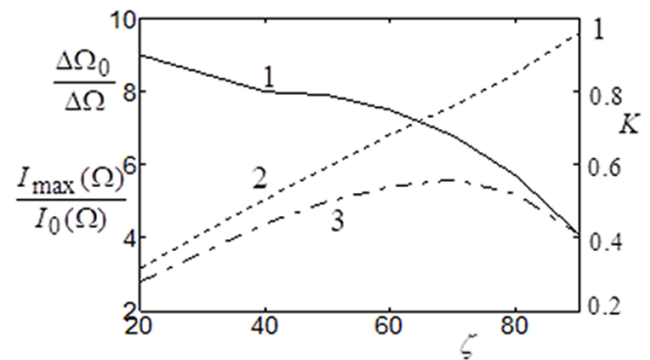


Fig. 3: The K (1) and self-SC ($\Delta\Omega_0/\Delta\Omega$) (2), $I_{max}(\Omega)/I_0(\Omega)$ (3) vs fiber length for initial Gaussian pulse.

stretched, which leads to the increasing of dispersion impact (the decreasing of L_D and R). When the condition $R < 1$ is satisfied ($L_D < L_{NL}$), the spectrum is compressed.

The process, which is described above has periodic character, but in the case of every next cycle, the quality of the SC is worse than in the case of the previous SC as spectral satellites increase within propagation.

Fig. 2 shows the peak value of spectra (1) and pulses (2) for initial Gaussian (a) and secant-hyperbolic (b) pulses, which shows that the process has a periodic character not only for Gaussian pulses but also for secant-hyperbolic pulses. The difference between Gaussian and secant-hyperbolic pulses is the speed of the process: as we see in Fig. 2, every next spectrum compression occurs in the short distance in the case of Gaussian pulses in comparison with the case of secant-hyperbolic pulses.

As we see in Fig. 2, the peak value decreases within the distance which is conditioned by the fact that the energy of spectral satellites increases. This fact is proved by the coefficient of SC quality, K , (the ratio of the energy in the central part of pulse to the whole energy). As we see in Fig. 3, the coefficient of SC quality decreases within the fiber length.

In the process of propagation, the behavior of the spec-

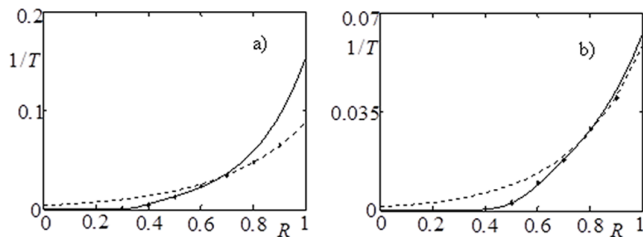


Fig. 4: The frequency vs nonlinearity parameter for initial secant-hyperbolic (a) and Gaussian (b) pulses. The points correspond to the numerical investigations, solid lines introduce the approximation of results (Eqs. 2, 3) by all points, while the dotted lines correspond to the approximation by last 3 points (Eqs. 4, 5).

trum is similar to the pulse behavior in the case of the soliton compression. As it is known, the propagation of the high-order solitons have periodic character with a $(\pi/2)L_D$ periodicity. On the distance equal to the periodicity, at first pulse is compressed, then it is stretched taking initial shape. In our case, the spectrum has similar behavior. However, due to the incomplete cancellation of the chirp, the changing of the spectrum does not have the strict periodic character. The process is different from soliton compression due to the fact that spectrum changes depend on a nonlinear phase, which depends on the shape of the pulse. In the case of soliton propagation, the changes of the pulse depend on a dispersive phase, which depends on neither spectral nor temporal shape of the pulse.

The study shows that the periodicity of the SC and stretching decreases with the reduction of nonlinearity parameter (Fig. 4). It is shown that there are polynomial (Eqs. 2, 3) and exponential (Eqs. 4, 5) approximations of the curve introducing nonlinearity parameter dependent frequency (Fig. 4), which is the frequency of the SC and stretching.

$$1/T = 1/(1.6 \times 10^7 \times 10^{-30R} + 7821 \times 10^{-4.79R}) \quad (2)$$

$$1/T = 1/(5.09 \times 10^6 \times 10^{-19.8R} + 731.3 \times 10^{-3.83R}) \quad (3)$$

$$1/T = 1/(0.004 \times e^{3.08R}) \quad (4)$$

$$1/T = 1/(0.001 \times e^{3.73R}) \quad (5)$$

3 Conclusion

Through the detailed study, we study the soliton-effect self-SC for initial Gaussian and secant-hyperbolic pulses. The process is realized in the fiber with a negative group-velocity dispersion. The study shows that there is an analogy between soliton self-compression and soliton-effect self-SC processes. We show that the periodicity of the process decreases when the nonlinearity parameter reduces. It is shown that the frequency dependence on the nonlinearity parameter has polynomial and exponential approximations.

Acknowledgements

The authors acknowledges Prof. R. Hakobyan for fruitful discussions and help during the work.

Received on December 4, 2017

References

1. Mouradian L., Louradour F., Messenger V., Barthélémy A., Froehly C. Spectrotemporal imaging of femtosecond events. *IEEE J. Quantum Electron.*, 2000, v. 36, 795.
2. Mansuryan T., Zeytunyan A., Kalashyan M., Yesayan G., Mouradian L., Louradour F., and Barthélémy A. Parabolic temporal lensing and spectrotemporal imaging: a femtosecond optical oscilloscope. *J. Opt. Soc. Am. B*, 2008, v. 25, A101–A110.
3. Kutuzyan A., Mansuryan T., Kirakosian A., Mouradian L. Self-forming of temporal dark soliton in spectral compressor. *Proc. SPIE*, 2003, v. 5135, 156–160.
4. Louradour F., Lopez-Lago E., Couderc V., Messenger V., Barthélémy A. Dispersive-scan measurement of the fast component of the third-order nonlinearity of bulk materials and waveguides. *Optics Lett.*, 1999, v. 24, 1361–1363.
5. Boscolo S., Turitsyn S., and Finot Ch. Amplifier similariton fiber laser with nonlinear spectral compression. *Optics Lett.*, 2012, v. 37, 4531–4533.
6. Clark S., Ilday F., Wise F. Fiber delivery of femtosecond pulses from a Ti:sapphire laser. *Optics Lett.*, 2001, v. 26, 1320–1322.
7. Andresen E., Dudley J., Oron D., Finot Ch., and Rigneault H. Transform-limited spectral compression by self-phase modulation of amplitude-shaped pulses with negative chirp. *Optics Lett.*, 2011, v. 36, 707–709.
8. Kutuzyan A., Mansuryan T., Yesayan G., Hakobyan R., Mouradian L. Dispersive regime of spectral compression. *Quantum Electron.*, 2008, v. 38, 383–387.
9. Hasegawa A., Tappert F. Transmission of Stationary Nonlinear Optical Pulses in the Dispersive Dielectric Fibers. I. Anomalous Dispersion. *Appl. Phys.*, 1973, v. 23, 142–144.
10. Mollenauer L., Stolen R., Gordon J. Experimental Observation of Picosecond Pulse Narrowing and Soliton in Optical Fibers Dispersive Dielectric Fibers. I. Anomalous Dispersion. *Phys. Rev. Lett.*, 1980, v. 45, 1095–1098.
11. Mollenauer L., Stolen R., Gordon J., and Tomlinson W. Extreme picosecond pulse narrowing by means of soliton effect in single-mode optical fibers Dispersive Dielectric Fibers. I. Anomalous Dispersion. *Optics Lett.*, 1983, v. 8, 289–291.
12. Yesayan G. *Journal of Contemporary Physics*, 2012, v. 45, 225.
13. Grigoryan A., Yesayan G., Kutuzyan A. and Mouradian L. Spectral domain soliton-effect self-compression. *Journal of Physics: Conference Series*, 2016, v. 672.
14. Akhmanov S. A., Vysloukh V. A. and Chirkin A. S. *Optics of Femtosecond Laser Pulses*. AIP, New York, 1992.
15. Hardin R., Tappert F. Applications of the Split-Step Fourier Method to the Numerical Solution of Nonlinear and Variable Coefficient Wave Equations. *Cronicle*, 1973, v. 15, 423.
16. Fisher R., Bischel W. The role of linear dispersion in plane-wave self-phase modulation. *Appl. Phys. Lett.*, 1973, v. 23, 661–663.

A Symplectic Cosmological Model

Jean-Pierre Petit

Former director of scientific research at Observatoire de Marseille, France

E-mail: jp.petit@mailaps.org

In this paper, we use the Lie algebra of the dual Poincaré dynamical group which when acted upon by its coadjoint, displays energy momentum and spin as pure geometrical quantities. When extended to the full group, one obtains negative mass species in accordance with our *Janus Cosmological Model* and the twin universe model conjectured by A. Sakharov. Within a *5D Kaluza space*, the theory leads to a new matter/antimatter duality implying negative energy photons emitted on the negative domain of this twin Universe. This accounts for the dark matter and dark energy which are thereof impossible to detect in our domain. Finally, we show that shifting to a Hermitean space-time with an associated complex dynamic group yields imaginary energy, imaginary energy and imaginary charges all embedded in a symplectic (complex) framework which remains open to wide investigations.

Notations

Space time indices: $m, n = 0, 1, 2, 3$.

Space-time signature: -2 .

Einstein's constant: \varkappa .

Introduction

Symplectic geometry relies on symplectic manifolds. Those are said symplectic when they are endowed with a so-called *symplectic form* that allows for the measurement of sizes of 2-dimensional objects. In Riemannian geometry, the metric tensor probes lengths and angles, whereas the symplectic form measures areas.

The term symplectic was first coined by *H. Weyl* in 1939 as a substitute to rather confusing (line) complex groups and/or Abelian linear groups. The relativistic symplectic mechanics [1] was primarily developed by the french mathematician *J. M. Souriau* from dynamic groups theory. It provides a new description of energy, momentum and spin only in terms of pure geometrical quantities. This arises from two objects: n -dimensional space and its isometry group.

In what follows, we briefly describe its properties which we apply to a particular cosmological model featuring two types of masses and energies comparable to the *twin Universe* originally conjectured by *A. Zakharov*.

1 The Janus Cosmological Model (JCM)

The main mathematical tool used here is the so-called "*momentum map*" which is inferred from the *co-adjoint* action of the group on the dual of its *Lie algebra*. (The coadjoint of the Lie group is the dual of the adjoint representation.) Applying the technique of this coadjoint action leads to the appearance of generalized linear and angular momenta: {energy E , 3-momentum p , spin s }. The action of the group corresponds to

$$M' = L M^T M + N^T P^T L - L P^T N, \quad (1)$$

$$P' = L P, \quad (2)$$

where P is the generalized energy-momentum 4-vector

$$\begin{pmatrix} E \\ p_1 \\ p_2 \\ p_3 \end{pmatrix}, \quad (3)$$

L is here the element of the *Lorentz group* and N is the *boost 4-vector*. In the classical treatment, one merely considers the *restricted Poincaré Group* which is formed with orthochronous components L_0 . Hence, the *full Poincaré Group* can be written as

$$\begin{pmatrix} \lambda L_0 & N \\ 0 & 1 \end{pmatrix} \quad (4)$$

with $\lambda = \pm 1$.

We then obtain two kinds of matters and two kinds of photons with each an opposite mass and energy. This copes with the *Janus Cosmological Model* (JCM) we developed earlier [2–4]. Such a model involves particles with opposite masses and energy. However, as shown by *H. Bondi* [5], the field equations cannot sustain this duality due to the subsequent and unmanageable "*run away*" effect. In short, General Relativity deals with positive masses that are attractive, while negative masses would exhibit repelling forces. Therefore, if one considers a couple $(+m, -m)$, the negative mass escapes and is "chased" by the positive one while at the same time experiencing a uniform acceleration.

This issue can be evaded by considering a bi-metric (our *JCM model*) within a single manifold \mathfrak{M}_4 equipped with two metric tensors $(+g)_{\mu\nu}$ and $(-g)_{\mu\nu}$, which define two field equations [5]:

$$(+R)_{\mu\nu} - \frac{1}{2} (+g)_{\mu\nu} (+R) = \varkappa \left[(+T)_{\mu\nu} + \left(\frac{(-)g}{(+g)} \right)^{1/2} (-T)_{\mu\nu} \right], \quad (5)$$

$$(-R)_{\mu\nu} - \frac{1}{2} (-g)_{\mu\nu} (-R) = \varkappa \left[(-T)_{\mu\nu} + \left(\frac{(+g)}{(-g)} \right)^{1/2} (+T)_{\mu\nu} \right]. \quad (6)$$

Those time dependent and time independent solutions fit the observational data.

2 Extension to a wider geometrical framework

We now turn consider an extension of the group to a five dimensional scheme so as to obtain an *isometry group* which acts on the basic *Kaluza space-time*

$$\begin{pmatrix} \lambda\mu & 0 & \phi \\ 0 & \lambda L_0 & N \\ 0 & 0 & 1 \end{pmatrix} \quad (7)$$

with $\mu = \pm 1$ and $\lambda = \pm 1$.

By extending to the fifth dimension, the *Noether theorem* induces an additional conserved scalar quantity which is readily identified with the electric charge q .

The $\mu = -1$ implies both the inversion of this charge and the inversion of the fifth dimension, which is just the geometrical expression of the matter-antimatter duality as primarily shown by J. M. Souriau [6]. Therefore the physics ruled by the dynamical group (7) exhibits straightforwardly the matter-antimatter symmetry in the two domains with opposed mass and energy. If we now add p -Kaluza-like dimensions, we obtain the metric under the form:

$$ds^2 = dx_0^2 - dx_1^2 - dx_2^2 - dx_3^2 - d\xi_1^2 - d\xi_2^2 - \dots - d\xi_p^2. \quad (8)$$

This can be coupled to an isometry group

$$\begin{pmatrix} \lambda\mu & 0 & \dots & 0 & 0 & \phi_1 \\ 0 & \lambda\mu & \dots & 0 & 0 & \phi_2 \\ \dots & \dots & \dots & \dots & \dots & \dots \\ 0 & 0 & \dots & \lambda\mu & 0 & \phi_p \\ 0 & 0 & \dots & 0 & \lambda\mu & N \\ 0 & 0 & \dots & 0 & 0 & 1 \end{pmatrix} \quad (9)$$

with $\mu = \pm 1$ and $\lambda = \pm 1$.

The electric charge is just one of the quantum charges. Here again, the ($\mu = -1$) terms reflect the C -symmetry: they account for the classical matter-antimatter representation. The ($\mu = -1$; $\lambda = -1$) correspond to the PT -symmetry classically associated with the ‘‘Feynman antimatter’’ which is no longer identified with the ‘‘ C -antimatter’’. This is due to the presence of the time reversal T inducing both the mass and energy inversion. In other words, the group representation (9) which is the basis of the *JC Model*, provides two distinct types of antimatters:

- The C -type corresponding to Dirac’s antimatter.
- The PT -type corresponding to Feynman’s antimatter.

3 Remark about Andrei Sakharov’ scheme

In classical cosmology a severe problem remains, due to the absence of observation of primordial antimatter. In 1967,

Sakharov suggested that the Universe comprises two domains: the actual Universe and its twin Universe, each connected through a singularity [8–10]. Both are CPT -symmetrical. Since the mass inversion goes with T -symmetry, our *JC Model* [3,4] corresponds to such CPT -symmetry. The so-called *twin matter* becomes nothing but a copy of ordinary particles with opposite masses and charges. If, as suggested by Sakharov, positive masses are synthesized by positive energy quarks faster than the synthesis of negative masses from positive energy antiquarks, then in the *positive energy domain* we find:

- Remnant positive masses matter.
- The equivalent (ratio 3/1) of positive energy antiquarks.
- Positive energy photons.

In analogy to Sakharov’s ideas, the negative energy domain would be thus composed of:

- Remnant negative masses matter.
- The equivalent (ratio 3/1) of negative energy quarks.
- Negative energy photons.

As shown in [3,4], the negative material suitably replaces both dark matter and so-called dark energy. Accordingly, by emitting negative energy photons, the remnant negative masses matter are genuinely invisible.

4 Remark about the Quantum Theory of Fields (QFT)

In QFT the time reversal operator is a complex operator which can be *linear* and *unitary*, as well as *antilinear* and *anti-unitary*. If chosen linear and unitary, this operator implies the existence of negative energy states, which are *à priori* banned by QFT. In Weinberg [7], we quote: ‘‘*In order to avoid this disastrous conclusion, we are forced to conclude that T is antilinear and anti-unitary*’’. On page 104, Weinberg also writes: ‘‘*no examples are known of particles that furnish unconventional representation of inversions, so these possibilities will not be pursued further here*’’. Actually, this was true until the discovery of the acceleration of the expanding universe which implies the action of a negative pressure. As a pressure is likened to an energy density, this new phenomenon implies in turn the existence of negative energy states and as a result, it questions QFT by itself. In the same manner, it also raises some questions as to the validity of the so-called CPT theorem and the vacuum instability. Indeed, classically, one considers that a particle may loose energy through the emission of a photon, so that such a process would lead to negative energy states. But if we consider that a negative mass particle emits negative energy photons, this process would lead to stable zero energy state.

5 Extension of the method to a complex field

If one replaces the Minkowski coordinates $\{x_0, x_1, x_2, x_3\}$ with complex coordinates we may form the *Hermitean Riemann*

metric:

$$ds^2 = dx_0^* dx_0 - dx_1^* dx_1 - dx_2^* dx_2 - dx_3^* dx_3. \quad (10)$$

This metric is defined on a *Hermitean manifold*.

Lest us now consider the real matrix G

$$\begin{pmatrix} 1 & 0 & 0 & 0 \\ 0 & -1 & 0 & 0 \\ 0 & 0 & -1 & 0 \\ 0 & 0 & 0 & -1 \end{pmatrix} \quad (11)$$

and the complex Lorentz group defined as

$${}^*LGL = G, \quad (12)$$

*L stands for the *adjoint* of L .

One can then easily show that the *complex Poincaré group*

$$\begin{pmatrix} L & N \\ 0 & 1 \end{pmatrix} \quad (13)$$

is an isometry group of such a Hermitean space and can be considered as a dynamic group. Surprisingly, all classical (matrix) calculations can be extended to such complex framework, by simply substituting the matrices *A to the transpose matrices ${}^T A$.

As a result, the complex momentum obeys the law:

$$M' = LM^*L + N^*P^*L - LP^*N, \quad (14)$$

$$P' = LP, \quad (15)$$

where *P is the complex energy momentum 4-vector. This extended physics grants the mass a complex nature implying the possible existence of purely real masses $\pm m$ and purely imaginary masses: $\pm(-1)^{1/2} m$. At the same time, such masses can exchange imaginary photons whose energies are: $\pm(-1)^{1/2} E$.

Conclusion

J. M. Souriau gave the first purely geometrical interpretation of all classical physics features, namely — energy, momenta, and spin. When extended to higher dimensions it provides a geometrical interpretation of the matter-antimatter duality. In addition, one can notice that the complex approach of space definition yields complex physical quantities. The physical meaning of these complex quantities should demand further scrutiny and as such remains a new open field of investigations.

Submitted on December 25, 2017

References

1. Souriau J. M. Structure des Systèmes Dynamiques. Dunod, Paris, 1970 (English translation: Structure of Dynamic Systems. Birkhäuser, 1997).
2. Petit J. P., D'Agostini G. Negative mass hypothesis in Cosmology and the nature of dark energy. *Astrophysics and Space Sciences*, 2014, v. 354, issue 2, 611–615
3. Petit J. P., D'Agostini G. Cosmological Bi-metric model with interacting positive and negative masses and two different speeds of light in agreement with the observed acceleration of the Universe. *Modern Physics Letters A*, 2014, v. 29, no. 34.
4. Petit J. P., D'Agostini G. Lagrangian derivation of the two coupled field equations in the Janus Cosmological Model. *Astrophysics and Space Science*, 2015, v. 357, issue 1, 67–74.
5. Bondi H. Negative mass in General Relativity. *Rev. of Mod. Physics*, 1957, v. 29, issue 3, 423.
6. Souriau J. M. Géométrie et Relativité. Hermann, 1964.
7. Weinberg S. The Quantum Theory of Fields. Cambridge University Press, 2005, p. 74–76, p. 104.
8. Sakharov A. D. *ZhETF Pis'ma*, 1967, v. 5, 32–35; *JTEP Lett.*, 1967, v. 5, 24–27.
9. Sakharov A. D. *ZhETF Pis'ma*, 1979, v. 76, 1172–1181; *JTEP*, 1979, v. 49, 594–603.
10. Sakharov A. D. Cosmological model of the Universe with a time vector inversion. *ZhETF*, 1980, v. 79, 689–693; *Tr. JTEP*, v. 52, 349–351.

Quantum Gravity Aspects of Global Scaling and the Seismic Profile of the Earth

Hartmut Müller

E-mail: hm@interscalar.com

In this paper we derive a profile of the Earth's interior from our fractal model of matter as chain system of harmonic quantum oscillators. Model claims are verified by geophysical data. Global scaling as model of quantum gravity is discussed.

Introduction

The origin of gravity is a key topic in modern physics. The universality of free fall means that the gravity acceleration of a test body at a given location does not depend on its mass, physical state or chemical composition. This discovery, made four centuries ago by Galilei, is confirmed by modern empirical research with an accuracy of 10^{-11} - 10^{-12} [1–3]. A century ago Einstein supposed that gravity is indistinguishable from, and in fact the same thing as, acceleration. In fact, Earth's surface gravity acceleration can be derived from the orbital elements of any satellite, also from Moon's orbit:

$$g = \frac{4\pi^2 R^3}{(T \cdot r)^2} = \frac{4\pi^2 (384399000 \text{ m})^3}{(2360591 \text{ s} \cdot 6371000 \text{ m})^2} = 9.83 \text{ m s}^{-2},$$

where R is the semi-major axis of Moon's orbit, T is the orbital period of the Moon and r is the average radius of the Earth. No data about the mass or chemical composition of the Earth or the Moon is needed.

The 3rd law of Johannes Kepler describes the ratio R^3/T^2 as constant for a given orbital system. Kepler's discovery is confirmed by high accuracy radar and laser ranging of the movement of artificial satellites. The geocentric gravitational constant [4] equals:

$$\mu = 4\pi^2 R^3 / T^2 = 3.986004418(8) \cdot 10^{14} \text{ m}^3 \text{ s}^{-2}.$$

Kepler's 3rd law is of geometric origin and can be derived from Gauss's flux theorem in 3D-space within basic scale considerations. It applies to all conservative fields which decrease with the square of the distance and does not require the presence of mass.

The orbital elements R and T are directly measured, while $\mu = GM$ is an interpretation that provides mass as a source of gravity and the universality of the big G . Both postulates are essential in Newton's law of universal gravitation and in Einstein's general theory of relativity.

Nevertheless, coincidence and causality is not the same thing and Newton's hypothesis about mass as source of gravity could turn out to be a dispensable assumption.

In the case of mass as source of gravity, in accordance with Newton's shell theorem, a solid body with a spherically symmetric mass distribution should attract particles outside it as if its total mass were concentrated at its center. In contrast,

the attraction exerted on a particle should decrease as the particle goes deeper into the body and it should become zero at the body's center.

A boat at the latitude 86.71 and longitude 61.29 on the surface of the Arctic Ocean would be at the location that is regarded as having the highest gravitational acceleration of 9.8337 m/s^2 on Earth. At higher or lower position to the center of the Earth, gravity should be of less intensity. This conclusion seems correct, if only mass is a source of gravity acceleration and if the big G is universal under any conditions and in all scales.

The Preliminary Reference Earth Model [5] affirms the decrease of the gravity acceleration with the depth. However, this hypothesis is still under discussion [6–8].

In 1981, Stacey, Tuck, Holding, Maher and Morris [9, 10] reported anomalous measures (larger values than expected) of the gravity acceleration in deep mines and boreholes. In [11] Frank Stacey writes: "Modern geophysical measurements indicate a 1% difference between values at 10 cm and 1 km (depth). If confirmed, this observation will open up a new range of physics". In fact, gravity is the only interaction that is not described yet by a quantum theory.

In [12] we have introduced a fractal model of matter as a chain system of harmonic quantum oscillators. The model statements are quite general, that opens a wide field of possible applications.

Already in [13] we could show that scale invariance is a fundamental characteristic of this model. On this background we proposed quantum scaling as model of particle mass generation [14] and we could show that particle rest masses coincide with the eigenstates of the system. This is valid not only for hadrons, but for mesons and leptons as well. Andreas Ries [15] demonstrated that this model allows for the prediction of the most abundant isotope of a given chemical element.

In the framework of our model, physical characteristics of celestial bodies can be understood as macroscopic quantized eigenstates in chain systems of oscillating protons and electrons [16]. This is also valid for accelerations. In [17] was shown that the surface gravity accelerations of the planets in the solar system correspond with attractor nodes of stability in chain systems of protons and electrons.

Our model allows us to see a connection between the sta-

bility of the solar system and the stability of electron and proton and consider global scaling as a forming factor of the solar system. This may be of cosmological significance.

In this paper we derive a profile of the Earth’s interior from our fractal model of matter as chain system of harmonic quantum oscillators. Model claims are verified by geophysical data. Global scaling as model of quantum gravity is discussed.

Methods

In [13] we have shown that the set of natural frequencies of a chain system of similar harmonic oscillators can be described as set of finite continued fractions \mathcal{F} , which are natural logarithms:

$$\ln(\omega_{jk}/\omega_{00}) = n_{j0} + \frac{z}{n_{j1} + \frac{z}{n_{j2} + \dots + \frac{z}{n_{jk}}}} = [z, n_{j0}; n_{j1}, n_{j2}, \dots, n_{jk}] = \mathcal{F} \tag{1}$$

where ω_{jk} is the set of angular frequencies and ω_{00} is the fundamental frequency of the set. The denominators are integer: $n_{j0}, n_{j1}, n_{j2}, \dots, n_{jk} \in \mathbb{Z}$, the cardinality $j \in \mathbb{N}$ of the set and the number $k \in \mathbb{N}$ of layers are finite. In the canonical form, the numerator z equals 1.

In the canonical form, for finite continued fractions, the distribution density of the eigenvalues reaches maxima near reciprocal integers $1, 1/2, 1/3, 1/4, \dots$ which are the attractor points of the fractal set \mathcal{F} of natural logarithms (fig. 1).

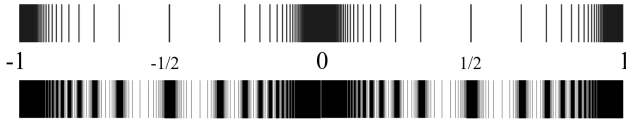


Fig. 1: The canonical form of \mathcal{F} for $k = 1$ (above) and for $k = 2$ (below) in the range $-1 \leq \mathcal{F} \leq 1$.

Any finite continued fraction represents a rational number [18]. Therefore, all natural frequencies ω_{jk} in (1) are irrational, because for rational exponents the natural exponential function is transcendental [19]. This circumstance provides for high stability of eigenstates in a chain system of harmonic oscillators because it prevents resonance interaction between the elements of the system [20]. Already in 1987 we have applied continued fractions of the type \mathcal{F} as criterion of stability in engineering [21, 22].

In the case of harmonic quantum oscillators, the continued fractions \mathcal{F} define not only fractal sets of natural angular frequencies ω_{jk} , angular accelerations $a_{jk} = c \cdot \omega_{jk}$, oscillation periods $\tau_{jk} = 1/\omega_{jk}$ and wavelengths $\lambda_{jk} = c/\omega_{jk}$ of the chain system, but also fractal sets of energies $E_{jk} = \hbar \cdot \omega_{jk}$ and masses $m_{jk} = E_{jk}/c^2$ which correspond with the eigenstates of

the system. For this reason, we call the continued fraction \mathcal{F} the “fundamental fractal” of eigenstates in chain systems of harmonic quantum oscillators.

In the canonical form ($z = 1$) of the fundamental fractal \mathcal{F} , shorter continued fractions correspond with more stable eigenstates of a chain system of harmonic oscillators. Therefore, integer logarithms represent the most stable eigenstates (main attractor nodes).

As the cardinality and number of layers of the continued fractions \mathcal{F} are finite but not limited, in each point of the space-time occupied by the chain system of harmonic quantum oscillators the scalar \mathcal{F} is defined. Consequently, any chain system of harmonic quantum oscillators can be seen as source of the scalar field \mathcal{F} , the fundamental field of the system. Figure 2 shows the linear 2D-projection of the first layer ($k = 1$) of the fundamental field \mathcal{F} in the canonical form ($z = 1$) in the interval $-1 \leq \mathcal{F} \leq 1$.

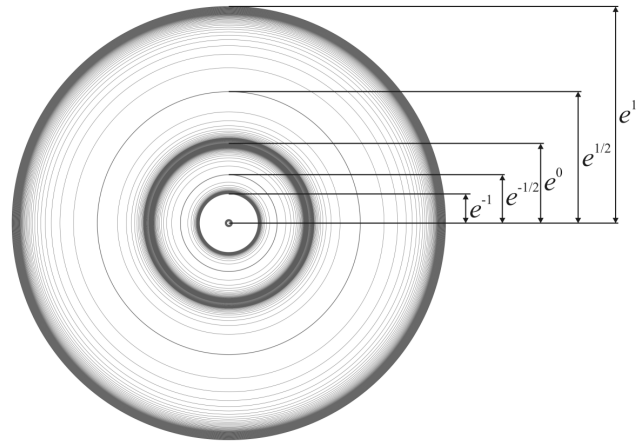


Fig. 2: The first layer ($k = 1$) of the linear 2D-projection of the fundamental field \mathcal{F} in the canonical form ($z = 1$) in the range $-1 \leq \mathcal{F} \leq 1$.

The scalar potential difference $\Delta\mathcal{F}$ of sequent equipotential surfaces at a given layer k is defined by the difference of continued fractions (1). In the canonical form ($z = 1$):

$$\Delta\mathcal{F} = \mathcal{F}(j,k) - \mathcal{F}(j+1,k) = [n_{j0}; n_{j1}, n_{j2}, \dots, n_{jk}] - [n_{j0}; n_{j1}, n_{j2}, \dots, n_{j+1,k}]$$

Normal matter is formed by nucleons and electrons because they are exceptionally stable quantum oscillators. In the concept of isospin, proton and neutron are viewed as two states of the same quantum oscillator. Furthermore, they have similar rest masses. However, a free neutron decays into a proton, an electron and antineutrino within 15 minutes while the life-spans of the proton and electron top everything that is measurable, exceeding 10^{29} years [23].

These unique properties of the electron and proton predestinate their physical characteristics as fundamental units. Table 1 shows the basic set of electron and proton units that can be considered as a fundamental metrology (c is the speed of light in a vacuum, \hbar is the Planck constant, k_B is the Boltzmann constant).

PROPERTY	ELECTRON	PROTON
rest mass m	$9.10938356(11) \cdot 10^{-31}$ kg	$1.672621898(21) \cdot 10^{-27}$ kg
energy $E = mc^2$	0.5109989461(31) MeV	938.2720813(58) MeV
angular frequency $\omega = E/\hbar$	$7.76344071 \cdot 10^{20}$ Hz	$1.42548624 \cdot 10^{24}$ Hz
angular oscillation period $\tau = 1/\omega$	$1.28808867 \cdot 10^{-21}$ s	$7.01515 \cdot 10^{-25}$ s
angular wavelength $\lambda = c/\omega$	$3.8615926764(18) \cdot 10^{-13}$ m	$2.1030891 \cdot 10^{-16}$ m
angular acceleration $a = c\omega$	$2.327421 \cdot 10^{29}$ ms ⁻²	$4.2735 \cdot 10^{32}$ ms ⁻²

Table 1: The basic set of physical properties of the electron and proton. Data taken from Particle Data Group [23]. Frequencies, oscillation periods, accelerations and the proton wavelength are calculated.

In [16] was shown that the fundamental metrology (tab. 1) is completely compatible with Planck units [24]. Originally proposed in 1899 by Max Planck, these units are also known as natural units, because the origin of their definition comes only from properties of nature and not from any human construct. Max Planck wrote [27] that these units, “regardless of any particular bodies or substances, retain their importance for all times and for all cultures, including alien and non-human, and can therefore be called natural units of measurement”. Planck units reflect the characteristics of space-time.

In [12, 14] we have introduced a fractal model of matter as a chain system of oscillating protons and electrons. We hypothesize that scale invariance of the fundamental field \mathcal{F} calibrated on the physical properties of the proton and electron (tab. 1) is a universal characteristic of organized matter and criterion of stability. This hypothesis we have called ‘global scaling’ [16, 26, 27].

Results

The proton-to-electron mass ratio is approximately 1836, so that the mass contribution of the proton to normal matter is very high, for example in the hydrogen atom (protium) it is $1 - 1/1836 = 99.95$ percent. Consequently, the mass contribution of the electron is only 0.05 percent. In heavier atoms which contain neutrons, the electron contribution to atomic mass is even smaller. Therefore, in this paper we investigate a fractal model of matter as chain system of oscillating protons and derive a profile of the Earth’s interior from it.

As figure 1 shows, in an attractor node of the layer $k = 0$, the potential difference on the layer $k = 1$ changes its signature and compression of the equipotential density is changed to decompression. The same is valid in attractor nodes of the layer $k = 1$. There the potential difference on the layer $k = 2$ changes its signature. Therefore, we expect that near the attractor nodes of \mathcal{F} the dramatic increase of the field strength and the change of compression to decompression of the equipotential density in the attractor nodes should lead to measurable consequences. This should be valid at least for the main attractor nodes on the layer $k = 0$.

Figure 3 shows the \mathcal{F} calibrated on the angular Compton wavelength of the proton in the canonical ($z = 1$) linear 2D-projection for $k = 1$ in the interval $[49; \infty] \leq \mathcal{F} \leq [52; -4]$. At the graphic’s left side the corresponding radii in km are indicated. The radial distribution of equipotential nodes represents the expected 2D-profile of the Earth’s interior.

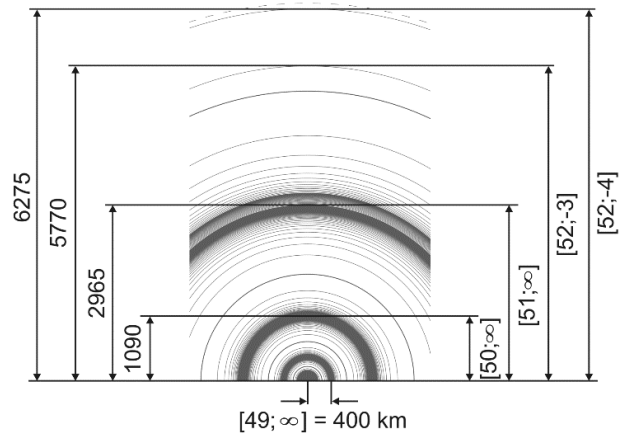


Fig. 3: The fundamental field \mathcal{F} calibrated on the proton in the canonical ($z = 1$) linear 2D-projection for $k = 1$ in the interval $[49; \infty] \leq \mathcal{F} \leq [52; -4]$. Radius in km (left side). The dotted line at the top indicates the Earth surface that coincides with the significant subnode $[44; 4] = 6372$ km of the \mathcal{F} calibrated on the electron.

The propagation speed of a seismic compression wave depends on the density and elasticity of the medium and should therefore correspond with zones of compression and decompression near the main nodes of the fundamental field \mathcal{F} .

In accordance with both empirical models of the Earth interior PREM [5] and IASP91 [28], the crust-mantle boundary (Mohorovicic discontinuity, ‘Moho’) is in between 35 and 90 km depth from the Earth surface, where seismic P-waves jump in speed abruptly from 6 to 8 km/s. In our model, the Moho corresponds with the compression zone before the significant subnode $[52; -4] = 6275$ km of the \mathcal{F} calibrated on the proton.

Detailed seismic studies have shown that the speed of P-waves (longitudinal pressure waves) in the mantle increases rather rapidly from about 9 to 11 km/s at depths between 400 and 700 km, marking a layer called the transition zone. This zone separates the upper mantle from the lower mantle. In our model, the transition zone corresponds with the compression zone before the significant subnode [52; -3] = 5770 km of the \mathcal{F} calibrated on the proton.

As they travel more deeply into the mantle, P-waves increase their speed from 8 km/s at the Moho to about 13 km/s at a depth of 2900 km. Though, once P-waves penetrate below 2900 km, their velocity suddenly drops from 13 km/s back down to about 8 km/s. This dramatic reduction in speed after a depth of 2900 km defines the boundary between the Earth's mantle and the core. The outer core seems liquid, because seismic S-waves (transversal shear waves) do not pass this boundary. In contrast, the innermost part of the core within a radius of 1210 km seems solid. Reaching the inner core, P-waves again jump to a velocity of 11 km/s.

Both models PREM and IASP91 identify these boundaries with the radius of the liquid core (3480 km) and the radius of the inner solid core (1210 km). These estimations correspond with the compression zones before the main attractors [51; ∞] and [50; ∞] of the proton \mathcal{F} and confirm that P-waves increase their velocity in the compression zone before the attractor. Then in the decompression zone after the attractor, they decrease the velocity. This coincidence is a strong confirmation of global scaling and demonstrates that the current dimension and structure of the Earth interior is not casual, but an essential criterion of its stability.

It is a notable circumstance that P-waves reach cosmic velocities. In fact, at the Moho, P-waves jump to velocities near 8 km/s that is in the range of the first cosmic velocity a rocket must have to reach a circular orbit around the Earth. In the transition zone that separates the upper mantle from the lower mantle, P-waves jump to 11 km/s that is in the range of the second cosmic velocity a rocket must have to escape the Earth gravity acceleration. Through the lower mantle, the P-wave reach 13 km/s at the core-mantle boundary that is in the range of velocities a rocket launched from Earth must have to escape the solar system.

This similarity seems not by case: cosmic escape velocities do not depend on the mass of the object escaping the Earth. The velocity a rocket must have to reach a circular orbit around the Earth depends only on the gravity acceleration g and the radius r of the departure orbit. It is notable that no data about the mass of the Earth is needed. In the case of departure from the Earth surface:

$$v_{circular} = \sqrt{gr} = \sqrt{9.8 \text{ m/s}^2 \cdot 6371000 \text{ m}} = 7.9 \text{ km/s.}$$

The second cosmic velocity a rocket must have to escape the Earth gravity acceleration is $\sqrt{2}$ times higher:

$$v_{escape} = \sqrt{2} \cdot v_{circular} = 11.2 \text{ km/s.}$$

Conversely, an object that falls under the attraction of the Earth surface gravity acceleration g from infinity, starting with zero velocity, will strike the Earth surface with a velocity equal to its escape velocity.

In accordance with our model (fig. 3), the inner core of the Earth should have a substructure that origins from the attractor node [49; ∞] = 400 km of the \mathcal{F} calibrated on the proton (fig. 4). In fact, the seismological exploration of the Earth's inner core has revealed unexpected structural complexities. There is a clear hemispherical dichotomy in anisotropy and also evidence of a subcore with a radius 300–600 km [29]. Considering that the radius of the Sun coincides with the main attractor node [49; ∞] of the \mathcal{F} calibrated on the electron:

$$\ln\left(\frac{r_{\text{Sun}}}{\lambda_{\text{electron}}}\right) = \ln\left(\frac{6.96407 \cdot 10^8 \text{ m}}{3.8615926764 \cdot 10^{-13} \text{ m}}\right) = 48.945$$

we can write down the equation for the ratio of the radii:

$$\frac{r_{\text{Sun}}}{r_{\text{Earth subcore}}} = \frac{\lambda_{\text{electron}}}{\lambda_{\text{proton}}}.$$

Already in [16] we have shown that the minimum and maximum values of the Earth's radius approximate the significant node [44; 4] of the \mathcal{F} calibrated on the electron:

$$\ln\left(\frac{r_{\text{Earth max}}}{\lambda_{\text{electron}}}\right) = \ln\left(\frac{6.384 \cdot 10^3 \text{ m}}{3.8615926764 \cdot 10^{-13} \text{ m}}\right) = 44.252,$$

$$\ln\left(\frac{r_{\text{Earth min}}}{\lambda_{\text{electron}}}\right) = \ln\left(\frac{6.353 \cdot 10^3 \text{ m}}{3.8615926764 \cdot 10^{-13} \text{ m}}\right) = 44.247.$$

Figure 3 shows the node [44; 4] of the electron \mathcal{F} as dotted line in the top of the graphic.

Conclusion

In the framework of our model of matter as chain system of harmonic quantum oscillators, the fractal fundamental field \mathcal{F} affects any type of physical interaction, including the gravitational. Fundamental particles like electron and proton are not the ultimate sources, but stability nodes of the fundamental field of any chain system of harmonic quantum oscillators. The spatial and temporal distribution of these stability nodes is determined by the ratio of fundamental constants. Already Paul Dirac [30] mentioned that "... whether a thing is constant or not does not have any absolute meaning unless that quantity is dimensionless".

Applying our fractal model of matter to the analysis of gravimetric and seismic characteristics of the Earth we did show that it corresponds well with established empirical models of the Earth interior. We interpret this correspondence as evidence of the fractality, scale invariance and macroscopic quantization of Earth's gravity field.

We presume that gravity is a scale-invariant attractor effect of stability nodes in chain systems of oscillating protons and electrons. May be this hypothesis could become a bridge that connects the island of gravity research with the continent of quantum physics.

Acknowledgements

I'm thankful to Leili Khosravi, Viktor Panchelyuga and Oleg Kalinin for valuable discussions.

Submitted on December 30, 2017

References

1. Niebauer T.M., McHugh M.P., Faller J.E. Galilean test for the fifth force. *Physical Review Letters*, 1987, v.59, 609–612.
2. Shapiro I.I. et al. Verification of the principle of equivalence for massive bodies. *Physical Review Letters*, 1976, v.36, 555–558.
3. Roll P.G., Krotov R., Dicke R.H. The equivalence of inertial and passive gravitational mass. *Annals of Physics*, 1964, v.26, 442–517.
4. Numerical Standards for Fundamental Astronomy. maia.usno.navy.mil, IAU Working Group, 2017.
5. Dziewonski A.M., Anderson D.L. Preliminary reference Earth model. *Physics of the Earth and Planetary Interiors*, 1981, v.25, 297–356.
6. Quinn T., Speake C. The Newtonian constant of gravitation — a constant too difficult to measure? An introduction. *Phil. Trans. Royal Society A*, v.372, 20140253.
7. Anderson J.D. et al. Measurements of Newton's gravitational constant and the length of day. *EPL*, 2015, v.110, 10002.
8. Cahill R.T. 3-Space In-Flow Theory of Gravity: Boreholes, Blackholes and the Fine Structure Constant. *Progress in Physics*, 2006, v. 2, issue 2, 9–16.
9. Stacey F.D. et al. Constraint on the planetary scale value of the Newtonian gravitational constant from the gravity profile within a mine. *Phys. Rev. D*, 1981, v.23, 1683.
10. Holding S.C., Stacey F.D., Tuck G.J. Gravity in mines. An investigation of Newton's law. *Phys. Rev. D*, 1986, v.33, 3487.
11. Stacey F.D. Gravity. *Science Progress*, 1984, v.69, no.273, 1–17.
12. Müller H. Fractal Scaling Models of Natural Oscillations in Chain Systems and the Mass Distribution of Particles. *Progress in Physics*, 2010, v.6, issue 3, 61–66.
13. Müller H. Fractal Scaling Models of Resonant Oscillations in Chain Systems of Harmonic Oscillators. *Progress in Physics*, 2009, v.5, issue 2, 72–76.
14. Müller H. Emergence of Particle Masses in Fractal Scaling Models of Matter. *Progress in Physics*, 2012, v.8, issue 4, 44–47.
15. Ries A. Qualitative Prediction of Isotope Abundances with the Bipolar Model of Oscillations in a Chain System. *Progress in Physics*, 2015, v.11, issue 2, 183–186.
16. Müller H. Scale-Invariant Models of Natural Oscillations in Chain Systems and their Cosmological Significance. *Progress in Physics*, 2017, v.13, issue 4, 187–197.
17. Müller H. Gravity as Attractor Effect of Stability Nodes in Chain Systems of Harmonic Quantum Oscillators. *Progress in Physics*, 2018, v.14, issue 1, 19–23.
18. Khintchine A.Ya. Continued fractions. University of Chicago Press, Chicago, 1964.
19. Hilbert D. Über die Transcendenz der Zahlen e und π . *Mathematische Annalen*, 1893, v.43, 216–219.
20. Panchelyuga V.A., Panchelyuga M.S. Resonance and Fractals on the Real Numbers Set. *Progress in Physics*, 2012, v.8, issue 4, 48–53.
21. Müller H. The general theory of stability and objective evolutionary trends of technology. *Applications of developmental and construction laws of technology in CAD*, Volgograd, VPI, 1987 (in Russian).
22. Müller H. Superstability as a developmental law of technology. *Technology laws and their Applications*, Volgograd-Sofia, 1989 (in Russian).
23. Olive K.A. et al. (Particle Data Group), *Chin. Phys. C*, 2016, v.38, 090001.
Patrignani C. et al. (Particle Data Group), *Chin. Phys. C*, 2016, v.40, 100001.
24. Astrophysical constants. Particle Data Group, pdg.lbl.gov
25. Planck M. Über Irreversible Strahlungsvorgänge. *Sitzungsbericht der Königlich Preußischen Akademie der Wissenschaften*, 1899, v.1, 479–480.
26. Müller H. Scaling as Fundamental Property of Natural Oscillations and the Fractal Structure of Space-Time. *Foundations of Physics and Geometry*, Peoples Friendship University of Russia, 2008 (in Russian).
27. Müller H. Scaling of body masses and orbital periods in the Solar System as consequence of gravity interaction elasticity. Abstracts of the *XIIIth International Conference on Gravitation, Astrophysics and Cosmology*, dedicated to the centenary of Einstein's General Relativity theory, Moscow, PFUR, 2015.
28. Kennett B.L.N. IASPEI 1991 Seismological Tables. Canberra, Australia, 1991.
Kennett B.L., Engdahl E.R. Travel times for global earthquake location and phase identification. *Geophysical Journal International*, 1991, v.105, 429–465.
29. Deguen R. Structure and dynamics of Earth's inner core. *Earth and Planetary Science Letters*, 2012, v.333–334, 211–225.
30. Dirac P.A.M. The cosmological constants. *Nature*, 1937, v.139, issue 3512, 323.

Relativistic Model for Radiating Spherical Collapse

Victor Medina¹ and Nelson Falcon²

¹Departamento de Física – Facultad de Ingeniería – Universidad de Carabobo. Valencia, Venezuela
E-mail: vmedina@uc.edu.ve

²Departamento de Física – Facultad Experimental de Ciencias y Tecnología – Universidad de Carabobo. Valencia, Venezuela
E-mail: nelsonfalconv@gmail.com

The relativistic models for radiating spherical collapse is important for to explain the emission process on very high energy in Supernova burst and Quasars. A general method is reviewed, to obtain models which describe non static radiating spheres, without having to make any hypothesis about the emission of radiation during the collapse. It is concluded that the field equations together with the conservation laws (Bianchi's Identity) form a complete set of integrable equations that do not require additional the emissivation hypothesis of a Gaussian pulse on at an arbitrary instant to trigger the collapse. The emissivation hypothesis of a Gaussian pulse is not only unnecessary, but also leads to qualitatively and quantitatively different solutions. Calculations were performed using the computer algebra package *GRTensorII*, running on *Maple 13*, along with several Maple routines that we have used specifically for this type of problems. The Schwarzschild and Tolman VI models are shown as examples where it's emphasizes the importance of using conservation equations properly, for describe the collapse for the self-gravitating sphere.

1 Introduction

The last phases of stellar evolution of massive stars are dominated by the contribution of stellar radiation due to changes of the inner or outer distribution of matter, in the gravitational potential of the radiating fluid spheres and, therefore, general relativity provides a description of the collapse of the compact objects (Neutron Stars, Black Holes). This description can be extended to explain the radiation process of very high energy in astrophysical scenarios, such as Supernova bursts and Quasars. A number of studies have been reported describing a gravitational collapse: Oppenheimer and Snyder [1], Tolman [2] and furthermore the study of the collapsing radiating fluid [3–6].

This scheme has recently been used for various scenarios of relativistic hydrodynamics. We can highlight some examples: charged fluids [7–9], isotropic [10] or anisotropic fluid [11, 12], shock waves [13, 14], in free space [15, 16] or diffusion process [17, 18]. It is necessary to contrast its quantitative results with other calculation schemes. Barreto et al. [19] have extended the semi-numerical scheme to the Schwarzschild coordinates, simulating some scenarios of the gravitational collapse.

Herrera and collaborators [6, 19–21] developed a general algorithm for modeling self gravitating spheres out of equilibrium, beginning from the known static solutions of Einstein's equations. This method divides the space-time in two spatial regions. The outer region is described by the Vaidya solution and the space-time metric in the interior is obtained by solving the Einstein field equations. Further, proper boundary conditions are imposed in order to guarantee a smooth matching of the solutions in the surface of the junction. This semi numerical technique has been used extensively to study high

energy in astrophysical scenarios [19, 21–27].

However in these numerical simulations a Gaussian pulse is introduced *ad hoc* to represent the emission of radiation that initiates the disequilibrium during the collapse of the radiating fluid ball [6, 20, 21, 23–25, 28]. These assumptions could be unnecessary and generate spurious solutions, since this loss of mass is prescribed by one of the conservation equations when applying the Bianchi Identity [29, 30]. Parts of the calculation of the Bianchi identities that were performed in this work were possible and verified using the *GRTensorII* package.

The purpose of this paper is to show the general method to obtain models which describe radiating non-static spheres without having to make any hypothesis about the emission of radiation during the collapse. This paper follows as much as possible the notation and physical description prescribed by Herrera et al. [6]. For this, the field equations and conservation laws are shown in Section 2; then section 3 establishes the procedure for the static solutions and obtaining the surface equations. The models Schwarzschild-like and Tolman VI-like are discussed in section 4 and 5 respectively, and in the last section are shown the concluding remarks.

2 The Field equations and conservation relationships

Let us consider a non static radiating spheres. The metric takes the form [4]

$$ds^2 = e^{2\beta} \frac{V}{r} du^2 + 2e^{2\beta} du dr - r^2 d\theta^2 - r^2 \sin^2 \theta d\phi^2, \quad (1)$$

where u and r are time like and radial-like coordinates respectively; β and V are functions of u and r ; θ, ϕ are the usual angle coordinates. In these coordinates the gravitational field equations are:

$$\begin{aligned}
 -8\pi T_{00} &= -\frac{V_{,0} - 2V\beta_{,0}}{r^2} - \frac{V}{r^3} (e^{2\beta} - V_{,1} + 2\beta_{,1}V) \\
 -8\pi T_{01} &= -\frac{1}{r^2} (e^{2\beta} - V_{,1} + 2\beta_{,1}V) \\
 -8\pi T_{11} &= -\frac{4\beta_{,1}}{r} \\
 -8\pi T_2^2 = -8\pi T_3^3 &= -e^{2\beta} \left(2\beta_{01} - \frac{1}{2r^2} [rV_{,11} + \right. \\
 &\quad \left. - 2\beta_{,1}V + 2r(\beta_{,11}V + \beta_{,1}V_{,1}) \right].
 \end{aligned}$$

As usual, note that we used the subscript $_{,0}$ and $_{,1}$ for the derivative for u and r , respectively; and the semicolon ($;$) for covariant differentiation. Then transformation relations between local Minkowskian and radiative coordinates are:

$$\begin{aligned}
 dt &= \left(\frac{\partial t}{\partial u} \right) du + \left(\frac{\partial t}{\partial r} \right) dr \\
 &= e^\beta \left(\frac{V}{r} \right)^{\frac{1}{2}} du + e^\beta \left(\frac{r}{V} \right)^{\frac{1}{2}} dr \quad (2)
 \end{aligned}$$

$$dx = \left(\frac{\partial x}{\partial r} \right) dr = e^\beta \left(\frac{r}{V} \right)^{\frac{1}{2}} dr \quad (3)$$

$$dy = \left(\frac{\partial y}{\partial \theta} \right) d\theta = r d\theta \quad (4)$$

$$dz = \left(\frac{\partial z}{\partial \phi} \right) d\phi = r \cdot \sin \theta d\phi. \quad (5)$$

We assumed the stellar material as perfect fluid, with energy density $\hat{\rho}$, radial pressure \hat{P} , without heat conduction neither viscosity, then

$$\hat{T}_{\alpha\beta} = (\hat{\rho} + \hat{P}) \cdot U_\alpha U_\beta - \hat{P} \cdot \eta_{\alpha\beta}, \quad (6)$$

where $U_\alpha = (1, 0, 0, 0)$, $3\hat{\sigma}$ is the isotropic radiation of the energy density, and $\hat{\varepsilon}$ no-polarized component of the energy density in radial direction. Now consider an observer in local Minkowskian system with radial velocity ω , in the Lorentzian system we can write:

$$\bar{T}_{\mu\nu} = \Lambda_\mu^\alpha \Lambda_\nu^\beta \hat{T}_{\alpha\beta}, \quad (7)$$

where the Lorentz matrix is

$$\Lambda_\mu^\alpha = \begin{bmatrix} \frac{1}{\sqrt{1-\omega^2}} & -\frac{\omega}{\sqrt{1-\omega^2}} & 0 & 0 \\ -\frac{\omega}{\sqrt{1-\omega^2}} & \frac{1}{\sqrt{1-\omega^2}} & 0 & 0 \\ 0 & 0 & 1 & 0 \\ 0 & 0 & 0 & 1 \end{bmatrix}. \quad (8)$$

We define

$$\bar{\rho} = \hat{\rho} + 3\hat{\sigma}, \quad \bar{P} = \hat{P} + \hat{\sigma}, \quad \bar{\varepsilon} = \hat{\varepsilon} \frac{1+\omega}{1-\omega}.$$

Note also that from (2-3) the velocity of matter in the radiative coordinates is given by

$$\frac{dr}{du} = \frac{V}{r} \cdot \frac{\omega}{1-\omega}, \quad (9)$$

so forth the energy-impulse tensor in the Lorentz system is

$$\begin{aligned}
 \bar{T}_{00} &= \bar{\varepsilon} + \frac{\bar{\rho} + \omega^2 \bar{P}}{1-\omega^2} \\
 \bar{T}_{01} = \bar{T}_{10} &= -\bar{\varepsilon} - \frac{\omega}{1-\omega^2} (\bar{\rho} + \bar{P}) \\
 \bar{T}_{11} &= \frac{\bar{P} + \omega^2 \bar{\rho}}{1-\omega^2} + \bar{\varepsilon} \\
 \bar{T}_{22} = \bar{T}_{33} &= \bar{P}.
 \end{aligned}$$

Using (2) - (5) we obtain the energy-impulse tensor in radiative coordinates as:

$$\begin{aligned}
 T_{00} &= e^{2\beta} \left(\frac{V}{r} \right) \left(\frac{\bar{\rho} + \omega^2 \bar{P}}{1-\omega^2} + \varepsilon \right) \\
 T_{01} = T_{10} &= e^{2\beta} \left(\frac{\bar{\rho} - \omega \bar{P}}{1+\omega} \right) \\
 T_{11} &= e^{2\beta} \left(\frac{r}{V} \right) \left(\frac{1-\omega}{1+\omega} \right) (\bar{\rho} + \bar{P}) \\
 T_{22} = \frac{T_{33}}{\sin^2 \theta} &= r^2 \bar{P}.
 \end{aligned}$$

Remember that a bar indicates that the quantity is measured in the Lorentzian system, and the effective variables are written without bar. Now

$$\rho \equiv \frac{\bar{\rho} - \omega \bar{P}}{1+\omega}, \quad P \equiv \frac{\bar{P} - \omega \bar{\rho}}{1+\omega}, \quad \varepsilon \equiv \bar{\varepsilon}. \quad (10)$$

It can be seen at once that $\rho = \bar{\rho}$ and $P = \bar{P}$ in $r = 0$, also, in the static case $\omega = 0$. As before then:

$$\begin{aligned}
 T_{00} &= e^{2\beta} \left(\frac{V}{r} \right) \left[\frac{\omega(\rho + P)}{(1-\omega)^2} + \rho + \varepsilon \right] \\
 T_{01} = T_{10} &= e^{2\beta} \rho \\
 T_{11} &= e^{2\beta} \left(\frac{r}{V} \right) (\rho + P) \\
 T_{22} = \frac{T_{33}}{\sin^2 \theta} &= r^2 \bar{P},
 \end{aligned}$$

thus the field equations are:

$$\begin{aligned}
 -\frac{V}{r^2} \left[\left(2\beta_{,0} - \frac{V_{,0}}{V} \right) - \frac{1}{r} (2V\beta_{,1} - V_{,1} + e^{2\beta}) \right] &= \\
 = 8\pi e^{2\beta} \left(\frac{V}{r} \right) \left[\varepsilon + \rho + \frac{\omega(\rho + P)}{(\omega - 1)^2} \right] & \quad (11)
 \end{aligned}$$

$$2V\beta_{,1} - V_{,1} + e^{2\beta} = 8\pi r^2 e^{2\beta} \rho \quad (12)$$

$$\frac{4\beta_{,1}}{r} = 8\pi \frac{r}{V} e^{2\beta} (\rho + P) \quad (13)$$

$$-2\beta_{,01} + \frac{1}{2r^2} [rV_{,11} - 2\beta_{,1}V + 2r(V_{,1}\beta_{,1} + V\beta_{,11})] = 8\pi e^{2\beta} \bar{P}. \tag{14}$$

Using the conservation equations (Bianchi Identity) $T^\mu_{\nu;\mu} = 0$, we obtain only three non-trivial relations:

$$T^\mu_{1;\mu} = \frac{e^{-2\beta}}{2\pi r} \beta_{,10} - \frac{\partial P}{\partial r} - \frac{1}{2} \left(2\beta_{,1} + \frac{V_{,1}}{V} - \frac{1}{r} \right) (\rho + P) - \frac{2(P - \bar{P})}{r} = 0, \tag{15}$$

$$T^\lambda_{0;\lambda} = \frac{V}{r} \left\{ \left(2\beta_{,1} + \frac{V_{,1}}{V} + \frac{1}{r} \right) \left[\varepsilon + \frac{\omega(\rho + P)}{(1 - \omega)^2} \right] + \frac{\omega}{(1 - \omega)^2} \frac{\partial(\rho + P)}{\partial r} \right\} + \frac{1}{2} \left(2\beta_{,0} - \frac{V_{,0}}{V} \right) (\rho + P) + \frac{\partial \rho}{\partial u} + \frac{V}{r} \left[\frac{\partial \varepsilon}{\partial r} + \frac{1 + \omega}{(1 - \omega)^3} (\rho + P) \frac{\partial \omega}{\partial r} \right] = 0, \tag{16}$$

$$e^{2\beta} T^\lambda_{;\lambda} = \frac{V}{r} \left\{ \left(2\beta_{,1} + \frac{V_{,1}}{V} + \frac{1}{r} \right) \left[\varepsilon + \frac{1 + \omega^2}{2(1 - \omega)^2} (\rho + P) \right] + \frac{\omega(\rho + P)_{,1}}{(1 - \omega)^2} + \frac{\partial P}{\partial r} + \frac{1}{r} [\rho + \bar{P} - (P - \bar{P})] \right\} - \frac{1}{2} \left(2\beta_{,0} - \frac{V_{,0}}{V} \right) (\rho + P) + \frac{\partial P}{\partial u} + \frac{V}{r} \left[\frac{\partial \varepsilon}{\partial r} + \frac{1 + \omega}{(1 - \omega)^3} (\rho + P) \frac{\partial \omega}{\partial r} \right] = 0. \tag{17}$$

It is remarkable that only two Bianchi equations (15-17) are independent, then

$$e^{2\beta} T^\mu_{;\mu} - T^\mu_{0;\mu} = \left(\frac{V}{r} \right) T^\mu_{1;\mu} = 0. \tag{18}$$

If we use the Bondi mass aspect $V \equiv e^{2\beta} (r - 2m)$, after some elementary algebra, the equation system becomes equivalent to:

$$m_{,1} = 4\pi r^2 \rho \tag{19}$$

$$\beta_{,1} = 2\pi r \frac{(\rho + P)}{1 - \frac{2m}{r}} \tag{20}$$

$$m_{,0} = -4\pi r^2 e^{2\beta} \left(1 - \frac{2m}{r} \right) \left[\varepsilon + \frac{\omega(\rho + P)}{(1 - \omega)^2} \right] \tag{21}$$

$$8\pi \bar{P} = -2\beta_{,01} e^{-2\beta} + \left(1 - \frac{2m}{r} \right) \left(2\beta_{,11} + 4\beta_{,1}^2 - \frac{\beta_{,1}}{r} \right) + \frac{1}{r} [3\beta_{,1} (1 - 2m_{,1}) - m_{,11}]. \tag{22}$$

Also, for two independent Bianchi equations (15) and (16), we obtain:

$$-\frac{e^{-2\beta}}{2\pi r} \beta_{,10} + \frac{\partial P}{\partial r} + \left(4\pi r^2 P + \frac{m}{r} \right) \frac{(\rho + P)}{r \left(1 - \frac{2m}{r} \right)} + \frac{2}{r} (P - \bar{P}) = 0, \tag{23}$$

$$\frac{e^{2\beta}}{r} \left[1 + \left(1 - \frac{2m}{r} \right) + 4\pi r^2 (P - \rho) \right] \left[\varepsilon + \frac{\omega(\rho + P)}{(1 - \omega)^2} \right] + \frac{V}{r} \frac{\omega}{(1 - \omega)^2} \frac{\partial}{\partial r} (\rho + P) + \frac{V}{r} \left[\frac{\partial \varepsilon}{\partial r} + \frac{(1 + \omega)(\rho + P)}{(1 - \omega)^3} \frac{\partial \omega}{\partial r} \right] + \frac{\partial \rho}{\partial u} = 0. \tag{24}$$

The expression (23) is the generalization of the Tolman - Oppenheimer - Volkoff (TOV) equation of hydrostatic equilibrium (see, for example [31]). It can be shown that the conservation equation (24) can also be obtained from the field equations (19) and (21), remembering that the second mixed derivatives commute, that is, $m_{,01} = m_{,10}$. Now, combining (21) with (24) we obtain:

$$\frac{2m_{,0} e^{-2\beta}}{4\pi r^3 \left(1 - \frac{2m}{r} \right)} \left[1 - \frac{m}{r} + 2\pi r^2 (P - \rho) \right] = \frac{\omega}{(1 - \omega)^2} \left(1 - \frac{2m}{r} \right) (\rho + P)_{,1} + \frac{\partial \varepsilon}{\partial r} + \frac{(1 + \omega)(\rho + P)}{(1 - \omega)^3} \frac{\partial \omega}{\partial r} + \frac{e^{-2\beta}}{4\pi r^2} m_{,10}.$$

If we assume that radiation profiles ε and the variable ω , vary little, so we can write an expression very similar to the Euler equation

$$2m_{,0} \left[1 - \frac{m}{r} + 2\pi r^2 (P - \rho) \right] = \frac{\omega \cdot e^{2\beta}}{(1 - \omega)^2} \left[4\pi r^2 \left(1 - \frac{2m}{r} \right)^2 r (\rho + P)_{,1} \right] + r \left(1 - \frac{2m}{r} \right) m_{,10}. \tag{25}$$

Equation (25) is omitted in previous works on the evolution of radiating fluid sphere [6, 20, 21, 23, 28]. This omission prevents the closing of the system of equations, and motivates the spurious inclusion of a luminosity Gaussian pulse [21, 23–25, 28]. Equation (25) allows us relate the mass exchange with the time like and radial derivatives of the effective variables, and together with eq. (21), the radiation flux ε

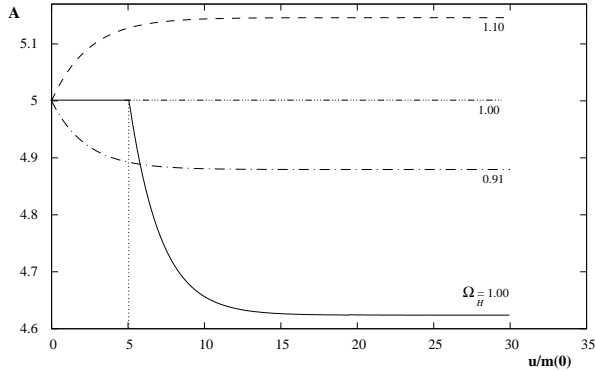


Fig. 1: The radius A as a function of the normalized time-like coordinate $\frac{u}{m(0)}$ for the initial values $A = 5.0$; $M = 1.0$ in the model Schwarzschild-like. Dashed line: $\Omega = 1$ static equilibrium, $\Omega = 1.1$ expansion; $\Omega = 0.91$ collapse. Solid line: solutions according to Herrera et al. [6].

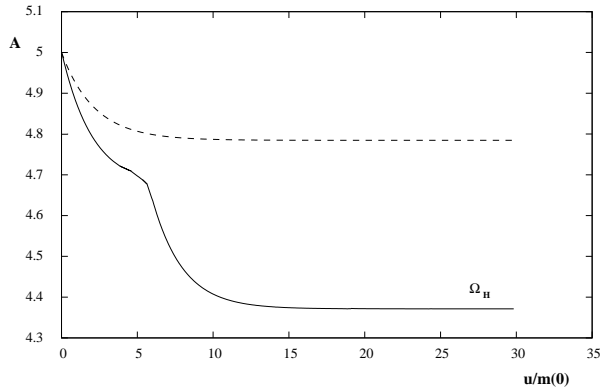


Fig. 2: The radius A as a function of the normalized time like coordinate $\frac{u}{m(0)}$ in the Schwarzschild-like model. Initial values for the surface variables $A = 5$; $M = 1.0$; $\Omega = 0.833$. Dashed line: calculations present. Solid line: solutions according to Herrera et al. [6].

is calculated. With the field equations (19) to (22) we can calculate the expressions of the physical variables ω , \bar{P} , $\bar{\rho}$, if we know the expressions $m(u, r)$ and $\beta(u, r)$ in each layer of the material under study. As a consequence, the state equations $P(u, r)$, $\rho(u, r)$ play an important role in determining the behavior of the physical variables present in the field equations and establishing their posterior evolution.

3 The models and surface equations

From the field equations (19) and (20) we can see

$$m = \int_0^r 4\pi r^2 \rho dr, \quad (26)$$

$$\beta = 2\pi \int_a^r \frac{\rho + P}{1 - \frac{2m}{r}} r \cdot dr. \quad (27)$$

These expressions for m and β are very similar to those obtained in the static case. This suggests a procedure to obtain dynamic solutions, following the same method of Herrera et al. [6], starting from a static solution:

1. Select a static solution of the gravitational field equations for a perfect fluid with spherical symmetry that explicitly shows its radial dependence

$$\rho_{static} = \rho(r) \quad P_{static} = P(r),$$

2. Suppose that the effective variables P and ρ (eq. 10) have the same radial dependence as in the static solution, but taking into account that now the edge condition $\bar{P}_a = 0$ is now expressed as

$$P_a = -\omega_a \rho_a. \quad (28)$$

Note that the subscript Δ_a indicates that the quantity Δ is evaluated at the edge of the distribution.

3. With this radial dependence for the effective variables, and together with (26) and (27), the values of m and β are calculable, except for three unknown functions (surface variables) that we are going to determine:

- (a) Equation (9) evaluated at $r = a$.
- (b) Equation (25) evaluated at $r = a$.
- (c) Equation (15) evaluated at $r = a$, or equation (22) evaluated at $r = a$.

4. Integrating numerically the ordinary differential equations obtained in (3), for a set of initial data, we completely determine the functions m and β .

5. With the field equations (19) to (22) we can calculate the expressions of the physical variables for the model considered.

As outlined in the previous methods (subsection 3), it is necessary to establish the surface variables and the equations that control its evolution.

- As mentioned in (subsection 3a), one of the surface equations is (9) evaluated at $r = a$, which takes the form

$$\dot{a} = \frac{da}{du} = \dot{A} = F(\Omega - 1), \quad (29)$$

where here it is very convenient to standardize the variables in terms of the initial mass $m(0) = m(u = 0, r = a)$ and define as surface variables:

$$A \equiv \frac{a}{m(0)} \quad M \equiv \frac{m_a}{m(0)} \quad \Omega \equiv \frac{1}{1 - \omega_a}, \quad (30)$$

as well as the variable

$$F = \left[e^{2\beta} \left(1 - \frac{2m}{r} \right) \right]_{r=a} = \left(\frac{V}{r} \right)_a, \quad (31)$$

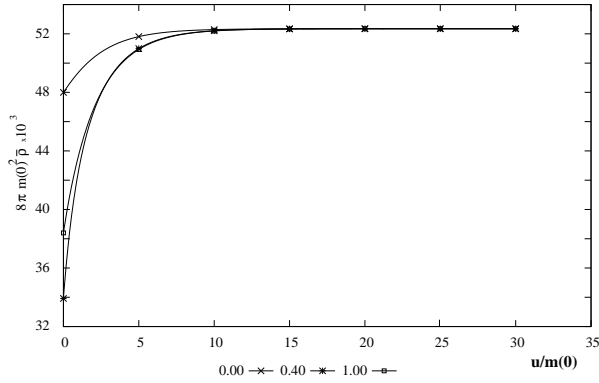


Fig. 3: Density $8\pi m(0)^2 \bar{\rho}$ in function of the temporal variable $\frac{u}{m(0)}$ for the model of Schwarzschild, for $\frac{t}{a} = 0.00, 0.40$ and 1.00 .

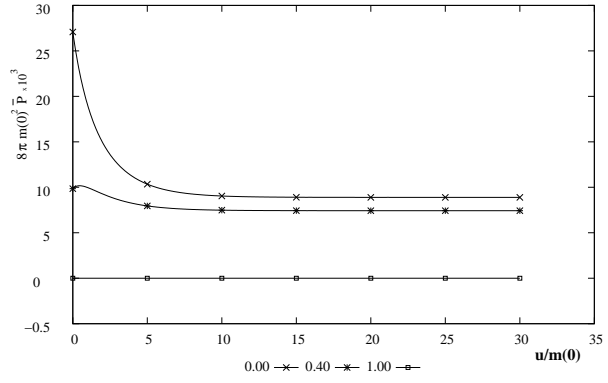


Fig. 4: Normalized pressure values $8\pi m(0)^2 \bar{P}$ in function of the time variable $\frac{u}{m(0)}$ for the model of Schwarzschild, for $\frac{t}{a} = 0.4$ and 1.00

Instead of using as surface variable F (31) – the gravitational potential at the surface –, as used in the references [6, 20, 21, 28]; we will use mass M , that is, the equation for radial evolution is

$$\dot{A} = \left(1 - \frac{2M}{A}\right)(\Omega - 1), \quad (32)$$

This equation is valid for all models.

- The second equation (25) is dependent on the model and it becomes necessary to calculate the first derivatives of the effective density and pressure, as can be seen.

$$2m_{,0}|_a \left\{ 1 - \frac{m}{r} + r\beta_{,1} \left(1 - \frac{2m}{r} \right) - m_{,1} \right\}_a + r \left(1 - \frac{2m}{r} \right) \frac{\partial}{\partial u} (4\pi r^2 \rho) \Big|_a = \Omega(\Omega - 1) \left[4\pi r^2 \left(1 - \frac{2m}{r} \right)^2 r \frac{\partial}{\partial r} (\rho + P) \right]_a \quad (33)$$

- The last equation (23) is the Tolman - Oppenheimer - Volkoff conservation equation evaluated at $r = a$, which we can write

$$\beta_{,10}|_a = 2\pi r \left(\frac{\partial P}{\partial r} \right) \Big|_a + \left[\frac{4\pi r^2 (\rho + P)}{2r^2 \left(1 - \frac{2m}{r} \right)} \right]_a \left(4\pi r^2 P + \frac{m}{r} \right)_a + 4\pi (P - P_t)|_a \equiv G. \quad (34)$$

Both equations (33) and (34) have a similar structure, in terms of the surface variables:

$$\Upsilon_M \dot{A} + \Xi_M \dot{M} + \Lambda_M \dot{\Omega} = \Delta_M \quad (35)$$

$$\Upsilon_\Omega \dot{A} + \Xi_\Omega \dot{M} + \Lambda_\Omega \dot{\Omega} = \Delta_\Omega, \quad (36)$$

where

$$\Upsilon_\xi \equiv \Upsilon_\xi(A, M, \Omega), \quad \Xi_\xi \equiv \Xi_\xi(A, M, \Omega), \quad \Lambda_\xi \equiv \Lambda_\xi(A, M, \Omega), \quad \Delta_\xi \equiv \Delta_\xi(A, M, \Omega), \quad \forall \xi \in \{M, \Omega\}$$

are functions of (A, M, Ω) . These three equations (32), (33) and (34) allow us to establish a system of three ordinary differential equations for the surface variables; which together with the initials data set, determine m and β , as set forth in subsection 4. Below are two examples for the interior distribution Schwarzschild-like and Tolman VI-like in section 4 and 5, respectively.

4 The Schwarzschild-like model

We will get as the first test example Schwarzschild's well-known internal and static constant density solution. For this, we are going to assume that the density depends only on the time-type variable, as explained in [6, 32] we can write the state equation for the Schwarzschild type model as

$$\rho = \frac{3m}{4\pi r^3} \quad (37)$$

$$P = \rho \left\{ \frac{1 - \frac{1}{g} \left[\frac{1 - \frac{2M}{A} \left(\frac{t}{a} \right)^2}{1 - \frac{2M}{A}} \right]^{\frac{1}{2}}}{\frac{1}{g} \left[\frac{1 - \frac{2M}{A} \left(\frac{t}{a} \right)^2}{1 - \frac{2M}{A}} \right]^{\frac{1}{2}} - 3} \right\}, \quad (38)$$

where the value of g is determinated from the boundary condition ($\bar{P}_a = 0$) then the effective pressure satisfies the relationship (28); and consequently $g = \frac{1}{3-2\Omega}$. Evaluating equation (9), for $r = a$, we get (32) and with (23) and (24) for

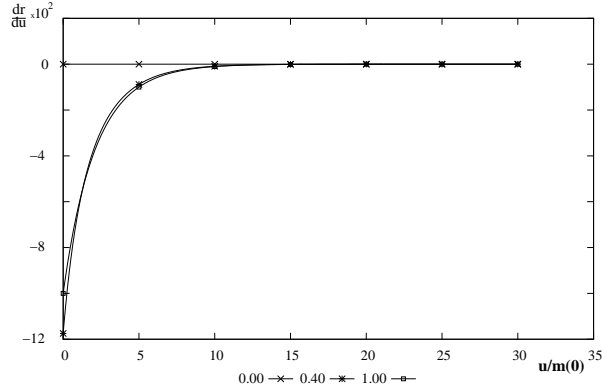


Fig. 5: Temporal velocity evolution in coordinates radiative $\frac{dr}{du}$, for the model of Schwarzschild, for $\frac{z}{a} = 0.00, 0.40$ and 1.00 .

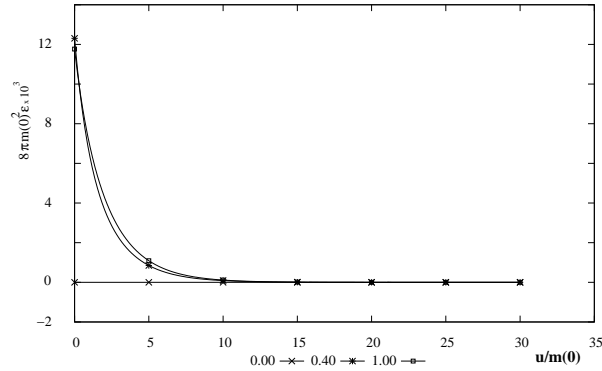


Fig. 6: Radiation profiles $8\pi m(0)^2 \varepsilon$. for the model of Schwarzschild. All layers emit radiation but decrease until reaching a state of equilibrium for $\Omega = 1$.

$r = a$ we obtain then

$$\begin{aligned} \dot{M} &= 3 \left(\frac{M}{A} \right)^2 \left(1 - \frac{2M}{A} \right) \frac{(\Omega - 1)(2\Omega - 3)}{\frac{3M}{A} - \Omega \left(1 + \frac{2M}{A} \right)} \\ \dot{\Omega} &= \frac{2\Omega(1 - \Omega)}{A} \left(1 - \frac{2M}{A} \right) - \frac{1}{A} \left(\frac{M}{A} \right) \left(\frac{3 - 2\Omega}{1 - \frac{2M}{A}} \right) \dot{A} + \\ &\quad - \frac{\Omega}{M} \frac{1}{\left(1 - \frac{2M}{A} \right)} \dot{M}, \end{aligned}$$

and from (20) and (19) we obtain, then after the immediate integration

$$\begin{aligned} m(r) &= m(0) \cdot M \left(\frac{r}{a} \right)^3 \\ \beta &= \frac{1}{2} \log \left[1 + \frac{3}{2\Omega} \left(\sqrt{\frac{1 - \frac{2M}{A}}{1 - \frac{2M}{A} \left(\frac{r}{a} \right)^2}} - 1 \right) \right]. \end{aligned}$$

Figures 1 and 2 show the evolution of the radius A . Notice that $\Omega = 1$ represents a condition of static equilibrium,

$\Omega > 1$ represents expansion, $\Omega < 1$ the collapse. In both cases the system returns to equilibrium very quickly. In order to make some comparison, we took the initial data very close to those chosen in the reference [6]. We did not use the value for $\Omega = 1$, since with this approximation the system does not have static behavior. The figures 3, 4, 5, 6 represent the profiles of physical variables versus the time like coordinates for different pieces of material and for initials data. We obtain monotonous variations in the physical quantities, as a consequence of the non-assumption of the Gaussian pulse. In particular it is shown in figure 6, how all the layers emit monotonously, unlike the figure 7 in Herrera et al. [6]

5 The Tolman VI-like model

Following [2] we can assume as static solution

$$\begin{aligned} 4\pi a^2 \rho &= 3h \left(\frac{a}{r} \right)^2 \\ 4\pi a^2 P &= h \left(\frac{a}{r} \right)^2 \left[\frac{1 - 9 \cdot z \left(\frac{z}{a} \right)}{1 - z \left(\frac{z}{a} \right)} \right], \end{aligned}$$

as before the value of z is determined from the boundary condition ($\bar{P}_a = 0$) then $P_a = -\omega_a \rho_a$; and consequently $z = \frac{4\Omega - 3}{3(4\Omega - 1)}$; and $h = \frac{m}{3r}$. Evaluating the equations (9), (23) and (24) at $r = a$ we obtain

$$\begin{aligned} \dot{M} &= - \frac{\left(1 - \frac{2M}{A} \right)^2 (16\Omega^2 + 3) \left(\frac{M}{A} \right) \dot{A}}{8 \left[\Omega \left(1 - \frac{2M}{A} \right) + \frac{M}{A} \right]} \\ \dot{\Omega} &= - \frac{1}{A} \left[\frac{M}{A} - \frac{(4\Omega - 3)(4\Omega - 1)}{8} \left(1 - \frac{2M}{A} \right) \right] \\ &\quad + (4\Omega - 1)(4\Omega - 3) \frac{\dot{A}}{8A} + \frac{\Omega}{\left(1 - \frac{2M}{A} \right)} \frac{\dot{M}}{M}, \end{aligned}$$

and the corresponding values of β and m are

$$\begin{aligned} \beta &= \frac{2M}{3A} \frac{1}{\left(1 - \frac{2M}{A} \right)} \left\{ \log \left(\frac{r}{a} \right) + 2 \log \left[\frac{3 - \left(\frac{4\Omega - 3}{4\Omega - 1} \right) \left(\frac{r}{a} \right)}{3 - \left(\frac{4\Omega - 3}{4\Omega - 1} \right)} \right] \right\} \\ m &= m(0) M \left(\frac{r}{a} \right). \end{aligned}$$

Figure 7 shows the temporal variation of the radius of a radiant sphere, for different values of Ω . There is a critical value Ω_0 for $A = 6.66$ and $M = 1$ and slight increase in Ω causes a permanent expansion or the contraction rises to the critical value. In the following figures 8,9,10 we show the variations of pressure density and radiation of some interior layers in case of surface expansion (explosion-like). We noted in the example in the figure 10 that all layers absorbed energy during the initial collapse, and then a radiative pulse is emitted, before returning to the equilibrium configuration.

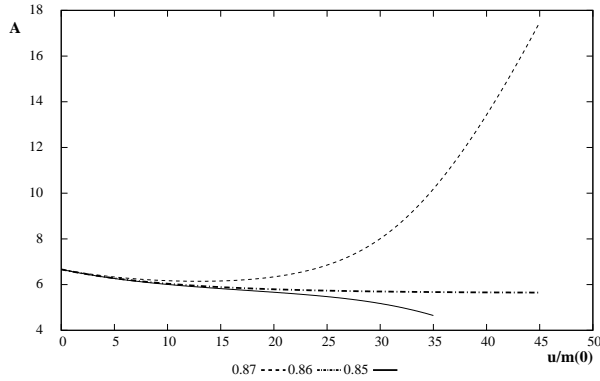


Fig. 7: Radio A of the distribution according to the variable temporary $\frac{u}{m(0)}$ in a TolmannVI-like model. With initials values, $A = 6.66667$; $M = 1$. $\Omega = 0.87$ (rebound) and $\Omega = 0.85$ (contraction) and the critical value $\Omega = 0.860723$

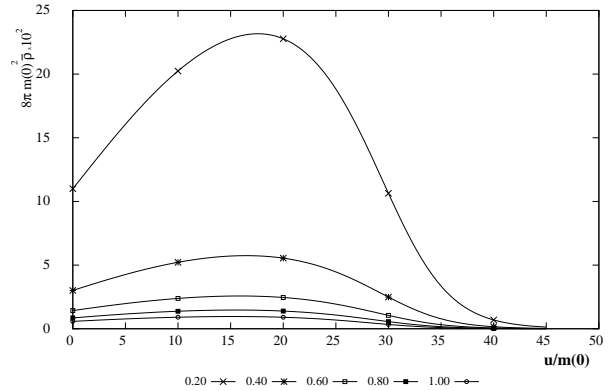


Fig. 9: Density $8\pi m(0)^2 \bar{\rho}$ as function of the time-like variable $\frac{u}{m(0)}$ in a TolmannVI-like model. For the layers in contraction ($\Omega = 0.87$) with $\frac{z}{a} = 0.2, 0.4, 0.6, 0.8$ and 1 .

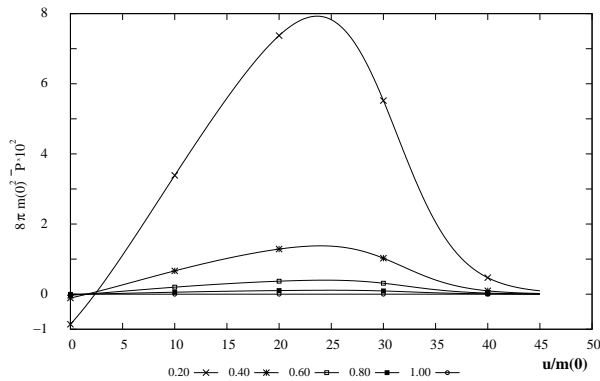


Fig. 8: Values of the normalized pressure $8\pi m(0)^2 \bar{P}$ as function of the time-like variable $\frac{u}{m(0)}$ in a TolmannVI-like model. For the layers in contraction ($\Omega = 0.87$) with $\frac{z}{a} = 0, 0.4, 0.6, 0.8$ and 1 .

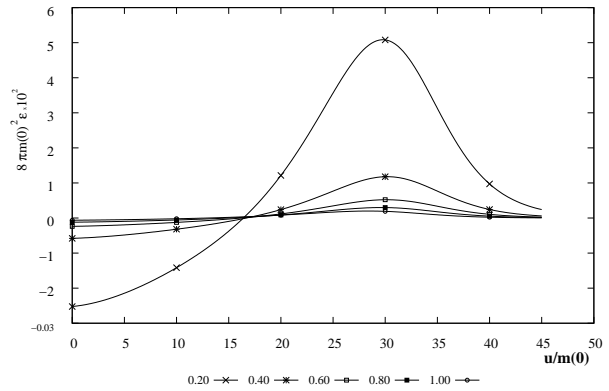


Fig. 10: Radiation profiles emitted $8\pi m(0)^2 \epsilon$ as function of the time-like variable $\frac{u}{m(0)}$ in a TolmannVI-like model. For the layers in contraction ($\Omega = 0.87$) with $\frac{z}{a} = 0.2, 0.4, 0.6, 0.8$ and 1 .

6 Conclusions

We have reviewed the relativistic description of the collapse of self-gravitating radiant spheres, following the usual procedure [6, 19–21, 23, 25, 28, 33] and find that it is an effective method for such a purpose, since the field equations together with the conservation laws (Bianchi’s Identity) form a complete set of integrable equations that do not require an additional hypothesis about the emission of radiated energy. That is, the emission hypothesis of a Gaussian pulse at an arbitrary instant to trigger the collapse; it is not only unnecessary, but also leads to qualitatively and quantitatively different solutions, as we have shown in figures 1-9. We emphasize the importance of using conservation equations properly, as was done in Section 2; We formally reobtain the generalized TOV equation of the hydrostatic equilibrium (equation 23) and a relativistic version of the Euler equation for the self-gravitating sphere (equation 25).

We have seen that the Schwarzschild-like description is an

ideal case that does not represent the phenomenology of the high energy events observed in the stellar collapse of massive stars such as supernovas and quasars. The measurable magnitudes of density, pressure and emission evolve smoothly, returning to the equilibrium condition very rapidly (Figures 3-6). On the other hand, the Tolman VI description involves two possible qualitatively different scenarios, such as the implosion or the explosion of the outer layers of the self-gravitating sphere, depending on the initial values of the mass, radius and velocity observables, as we have shown in figure 7.

We have shown that, in the case of contraction, the density and pressure variables similarly evolve (Figures 8 and 9) as might be expected if a polytrope state equation is used. In addition, Figures 8 and 9, show a dependence of the evolution of such magnitudes according to the radius of the considered layer, with much higher values of density and pressure in the innermost layers, in agreement with the description of the stellar collapse of massive stars.

Finally figure 10 shows that during the collapse of the

self-gravitating radiating spheres a pulse of radiation emission is generated before reaching equilibrium again; which arises *naturally* from the complete solution of the evolution equations, and maybe is important to explain the emission process in very high energy in Supernova bursts and Quasars.

Submitted on January 12, 2018

References

1. Oppenheimer J. R. and Snyder H. On Continued Gravitational Contraction. *Physical Review*, 1939, v. 56, 455–459.
2. Tolman R. C. Static Solutions of Einstein's Field Equations for Spheres of Fluid. *Physical Review*, 1939, v. 55, 364–373.
3. Vaidya P. C. Nonstatic Solutions of Einstein's Field Equations for Spheres of Fluids Radiating Energy. *Physical Review*, 1951, v. 83, 10–17.
4. Bondi H. The Contraction of Gravitating Spheres. *Proceedings of the Royal Society of London Series A*, 1964, v. 281, 39–48.
5. Bayin, S. Ş Radiating fluid spheres in general relativity. *Phys. Rev. D*, 1979, v. 19, 2838–2846.
6. Herrera L., Jiménez J., and Ruggeri G. J. Evolution of radiating fluid spheres in general relativity. *Phys. Rev. D*, 1980, v. 22, 2305–2316.
7. Patino A. and Rago H. The Effect of Electric Charge on the Evolution of Radiant Spheres in General Relativity. *Astrophysics and Space Science*, 1996, v. 241, 237–247.
8. Sah A. and Chandra P. Class of Charged Fluid Balls in General Relativity. *International Journal of Astronomy and Astrophysics*, 2016, v. 6, 494–511.
9. Pant N., Pradhan N. and Bansal R. K. Relativistic model of anisotropic charged fluid sphere in general relativity. *Astrophysics and Space Science*, 2016, v. 361, 41.
10. Harko T. and Mak M. K. Exact power series solutions of the structure equations of the general relativistic isotropic fluid stars with linear barotropic and polytropic equations of state. *Astrophysics and Space Science*, 2016, v. 361, 283.
11. Maurya S. K. and Maharaj S. D. Anisotropic fluid spheres of embedding class one using Karmarkar condition. *ArXiv e-prints*, 2017.
12. Singh K. N., Bhar P., and Pant N. A new solution of embedding class I representing anisotropic fluid sphere in general relativity. *International Journal of Modern Physics D*, 2016, v. 25, 1650099.
13. Herrera L. and Falcón N. Heat waves and thermohaline instability in a fluid. *Physics Letters A*, 1995, v. 201, 33–37.
14. Herrera L. and Santos N. O. Cylindrical collapse and gravitational waves. *Classical and Quantum Gravity*, 2015, v. 22, 2407–2413.
15. Van den Bergh N. and Slobodeanu R. Shear-free perfect fluids with a barotropic equation of state in general relativity: the present status. *Classical and Quantum Gravity*, 2016, v. 33(8), 085008.
16. Herrera L., Denmat G. L. and Santos N. O. Dynamical instability and the expansion-free condition. *General Relativity and Gravitation*, 2012, v. 44, 1143–1162.
17. Aguirre F., Hernandez H., and Nunez L. A. Radiation hydrodynamics and radiating spheres in general relativity. *Astrophysics and Space Science*, 1994, v. 219, 153–170.
18. Chan R., Herrera L., Pacheco J. A. F. and Santos N. O. Diffusion processes in the collapse of a radiating spherical body. *Astrophysical Journal*, 1991, v. 382, 255–260.
19. Herrera L. and Barreto W. Relativistic Gravitational Collapse in Co-moving Coordinates: the Post-Quasistatic Approximation. *International Journal of Modern Physics D*, 2011, v. 20, 1265–1288.
20. Cosenza M., Herrera L., Esculpi M. and Witten L. Evolution of radiating anisotropic spheres in general relativity. *Phys. Rev. D*, 1982, v. 25, 2527–2535.
21. Medina V., Nunez L., Rago H. and Patino A. Evolution of radiating charged spheres in general relativity. *Canadian Journal of Physics*, 1988, v. 66, 981–986.
22. Bonnor W. B., de Oliveira A. K. G., and Santos N. O. Radiating spherical collapse. *Phys. Rep.*, 1989, v. 181, 269–326.
23. di Prisco A., Falcón N., Herrera L., Esculpi M. and Santos N. O. Pre-relaxation Processes in a Radiating Relativistic Sphere. *General Relativity and Gravitation*, 1997, v. 29, 1391–1405.
24. Herrera L., Barreto W., di Prisco A., and Santos N. O. Relativistic gravitational collapse in noncomoving coordinates: The post-quasistatic approximation. *Phys. Rev. D*, 2002, v. 65(10), 104004.
25. Barreto W., Rodriguez B., and Martinez H. Radiating Fluid Spheres in the Effective Variables Approximation. *Astrophysics and Space Science*, 2002, v. 282, 581–593.
26. Pant N., Mehta R. N., and Tewari B. C. Relativistic model of radiating massive fluid sphere. *Astrophysics and Space Science*, 2010, v. 327, 279–283.
27. Tewari B. C. Relativistic collapsing radiating stars. *Astrophysics and Space Science*, 2012, v. 342, 73–77.
28. Patiño A. and Rago H. A Sphere Contraction in General Relativity. *Lett. Nuovo Cimento*, 1983, v. 38, 321–328.
29. Davies G. Second-Order Black Hole Perturbations: A Computer Algebra Approach, I – The Schwarzschild Spacetime. *ArXiv General Relativity and Quantum Cosmology e-prints*, 1998.
30. Neary N., Ishak M., and Lake K. Tolman type VII solution, trapped null orbits, and w-modes. *Phys. Rev. D*, 2001, v. 64(8), 084001.
31. Bekenstein J. D. Hydrostatic Equilibrium and Gravitational Collapse of Relativistic Charged Fluid Balls. *Phys. Rev. D*, 1971, v. 4, 2185–2190.
32. Aguirre F., Nunez L. A., and Soldovieri T. Variable Eddington Factor and Radiating Slowly Rotating Bodies in General Relativity. *ArXiv General Relativity and Quantum Cosmology e-prints*, 2005.
33. Barreto W., Rodríguez B., Rosales L., and Serrano O. Self-similar and charged radiating spheres: an anisotropic approach. *General Relativity and Gravitation*, 2007, v. 39, 537–538.

Progress in Physics is an American scientific journal on advanced studies in physics, registered with the Library of Congress (DC, USA): ISSN 1555-5534 (print version) and ISSN 1555-5615 (online version). The journal is peer reviewed and listed in the abstracting and indexing coverage of: Mathematical Reviews of the AMS (USA), DOAJ of Lund University (Sweden), Scientific Commons of the University of St.Gallen (Switzerland), Open-J-Gate (India), Referential Journal of VINITI (Russia), etc. Progress in Physics is an open-access journal published and distributed in accordance with the Budapest Open Initiative: this means that the electronic copies of both full-size version of the journal and the individual papers published therein will always be accessed for reading, download, and copying for any user free of charge. The journal is issued quarterly (four volumes per year).

Electronic version of this journal: <http://www.ptep-online.com>

Advisory Board of Founders:

Dmitri Rabounski, Editor-in-Chief
Florentin Smarandache, Assoc. Editor
Larissa Borissova, Assoc. Editor

Editorial Board:

Pierre Millette
Andreas Ries
Gunn Quznetsov
Felix Scholkmann
Ebenezer Chifu

Postal address:

Department of Mathematics and Science, University of New Mexico,
705 Gurley Avenue, Gallup, NM 87301, USA
